Ascorbic acid mediated reduction of $Fe(acac)_3$ for synthesis of Fe_3O_4 nanoparticles

アスコルビン酸を還元剤として用いた Fe_3O_4 ナノ粒子合成

Ph.D. Thesis

March 2017

Approved by

Professor Makoto Takahashi
Academic Supervisor

Ajinkya Girish Nene

Department of Applied Chemistry,
Chubu University, Japan

Abstract

Reproducible, size and shape controlled synthesis of magnetite (Fe_3O_4) nanoparticles was a challenge. To address this problem, we present a new, simple, and highly reproducible method for synthesizing size-controlled Fe_3O_4 nanoparticles by reduction of $Fe(acac)_3$ using ascorbic acid. Size controlled Fe_3O_4 nanoparticles were successfully synthesized by using this method. Particle size is controlled without using any surface capping agent. Particle size is controlled only by controlling reaction parameters such as ultrapure water concentration, addition temperature, ascorbic acid and precursor concentration, dropping/addition rate, reflux temperature and time, and stirring rate. Synthesized materials is characterized by various physico-chemical characterization techniques like scanning electron microscopy (SEM), transmission electron microscopy (TEM), energy dispersive X-ray analysis (EDAX), X-ray diffraction (XRD), X-ray photoelectron spectroscopy (XPS), Raman and Fourier Transform Infra-red spectroscopy in order to know the particle size and shape, particle size distribution, elemental composition, crystal structure, purity, phases (if any) etc.; and to correlate it to various synthesis parameters used.

A detailed comparative study of synthesis reaction conditions (ascorbic acid mediated reduction of $Fe(acac)_3$) in presence of ultrapure water and in absence of ultrapure water is presented in this thesis. It was observed that addition of ultrapure water during the chemical synthesis process yields Fe_3O_4 nanoparticles, whereas if the reaction is carried out in absence of water yields Fe nanoparticles - which get oxidized upon exposure to air atmosphere. Fe_3O_4 nanoparticles of smallest size of 15 ± 5 nm and Fe/iron oxide nanoparticles of smallest size of 7 ± 1 nm were successfully synthesized. Comparative study of the synthesis process parameters is presented in the thesis. Mechanism for formation of Fe_3O_4 nanoparticles is proposed herewith in which water acts as an oxygen supplier. Small (8 nm, 9 nm and 15 nm), medium (22 nm, 23 nm, 29 nm, 33 nm and 42 nm) and large (76 nm, 108 nm) sized Fe_3O_4 nanoparticles have been synthesized by varying and controlling the experimental conditions. Present proposed and demonstrated method is observed to yield reproducible results.

Further, the method is extended to synthesize a graphene-Fe_3O_4 nanocomposite in which graphene was first functionalized with carboxylic group and then added during the chemical synthesis of Fe_3O_4 nanoparticles by reduction of $Fe(acac)_3$ using ascorbic acid. In this study the monodisperse spherical nanoparticles of Fe_3O_4 with 10 nm particle diameter were observed to remain attached to graphene surface.

Contents

Chapter 1: Introduction

1 Motivation and Outline

Magnetic Fe_3O_4 nanoparticles are important because of their wide range of applications such as magnetic storage media, rotary shaft sealing, magnetic fluid hyperthermia, and drug delivery. Synthesis of magnetite nanoparticles with desired size in reproducible manner was a challenge. The established synthetic routes of Fe_3O_4 nanoparticles have difficulty in controlling the particle size, shape, and properties. Many of the reported methods have practical limitations and disadvantages. To solve these problems, it was necessary to establish a new synthesis method for Fe_3O_4 nanoparticles which can yield nanoparticles in reproducible manner with an excellent size control.

This thesis presents the work carried out on development of a new and novel synthesis route for Fe_3O_4 nanoparticles. Also hybrid nanocomposite based on Fe_3O_4 nanoparticles and graphene were synthesized by the new synthesis route. Their characterization and applications were also studied. The main objective of this research was to establish a synthesis route for synthesis of Fe_3O_4 nanoparticles without using any surface capping agent for controlling the particle size. This is due to the fact that surface capped nanoparticles are not suitable and difficult to process for further applications such as in cancer hyperthermia. Also, perfect control over the particle size is required along with reproducibility so as to have practical applications. In the present demonstrated method, Fe_3O_4 nanoparticles were synthesized by reduction of $Fe(acac)_3$ by ascorbic acid in presence of ultrapure water and dehydrated ethanol. A new mechanism for generation of magnetite (Fe_3O_4) nanoparticles was established. Reduction of $Fe(acac)_3$ by ascorbic acid was studied in detail with experimental synthesis parameters. Decomposition of Iron precursor $Fe(acac)_3$ was studied at different experimental parameters and decomposition efficiency was calculated. Reducing acid solution made up of dehydrated ethanol, ultrapure water and ascorbic acid was added into $Fe(acac)_3$ solution in diphenyl ether made of dissolving $Fe(acac)_3$ in diphenyl ether. This addition was carried out at preset temperature (60 ℃, 70 ℃, 80 ℃, etc.) conditions. Before calculating decomposition efficiency, the concentration of $Fe(acac)_3$ reduced by ascorbic acid at different time, temperature, ultrapure water concentration was calculated to understand the reaction and effect of these parameters on the decomposition efficiency. For synthesis of Fe_3O_4 nanoparticles, Reaction temperature after addition of reducing acid solution was raised to 190 ℃ (reflux temperature) for different time interval. Nanoparticles were separated by filtration and characterized by various physico-chemical characterization techniques. From this study a new mechanism for formation of Fe_3O_4 nanoparticles was proposed in which $Fe(acac)_3$ is reduced by ascorbic acid and ultrapure water acting as oxygen supplier to generate Fe_3O_4 nanoparticles. Experiments were done at

various parameters such as different concentration of ascorbic acid and ultrapure water, different temperatures at which reducing acid was added, reflux temperature, and time of reflux. Main objective was to control the size of Fe_3O_4 nanoparticles and to obtain the nanoparticles with size less than 20 nm. The reaction parameters were optimized to synthesize Fe_3O_4 nanoparticles with desired size (less than 20 nm). Fe_3O_4 nanoparticles with size 15±4 nm were obtained by this new synthetic route by reducing $Fe(acac)_3$ at 70 °C with ascorbic acid and refluxing at 190 °C for 1 hour.

Graphene-Fe_3O_4 nanocomposites were prepared in order to check the validity of our proposed reaction and to create a new composite material. Surface functionalization of graphene was carried out to obtain to provide anchoring site for Fe_3O_4 nanoparticles. Fe_3O_4 nanoparticles were synthesized on graphene which remains attached to graphene. Fe_3O_4 nanoparticles having average diameter 10 nm were deposited on graphene.

1.1. Nanotechnology and Nanobiotechnology

Nanotechnology and Biotechnology are major and important fields in science. Nanobiotechnology applying nanotechnology principles/materials to biotechnology area and hence is an interdisciplinary field. Nanobiotechnology is one of the 21st century's most promising technologies. A wide variety of applications can be explored by combining Nanotechnology and Biotechnology. Metal oxides such as titanium oxide, and zinc oxide (ZnO) are used in skincare products. Nanoparticles, are used in biotechnological applications like sensing (glucose sensing, gas sensing etc.), drug delivery. In food sector, some promising applications and technologies like nutrient delivery systems, biosensers, and edible films preparation for food are being developed [4]. Long term preservation of food and microbial contamination in food are main problems in food industry. Nanosensors can sense, if the food is correctly preserved or not at proper conditions such as temperature are under developments [1- 4].

Nanobiotechnology has great potential applications in biomedical area. Targeted drug delivery can be achieved by considering specific pathophysiological features of diseased tissue and use of drug loaded nanoparticles. Higher concentration of drugs can be accumulated by using nanoparticles as compared to normal drugs. Gold nanoparticles loaded with specific complementary DNA strands provide high sensitivity detection of pathogenic organisms. As sequence of interest can bind to complementary DNA strand present on gold nanoparticles it forms a dense visible web of gold nanoparticles, this kind of approach have shown promising results in detection of anthrax. Stable optical-electrical biosensors can be made by using semiconductor nanoparticles integrated with DNA, enzymes, antibodies [1, 5].

1.2 Nanomaterials

A nanometer is one billionth of one meter i.e. 10^{-9} m. Properties of nanomaterials are different from that of bulk form and atomic/molecular level from. Nanotechnology and applications of nanomaterials is now emerging field. Siegel classified nanomaterials as zero dimensional, one dimensional, two dimensional, three dimensional nanomaterials. Currently nanomaterials are used in various applications such as solar cells, fuel cells, making audio/video tapes, in computer hard drives, dental bonding agents, catalysis, water purifiers, skin care products etc. In biomedical science nanomaterials can be used for targeted drug delivery, disease diagnosis, sensing applications [1, 6, 7, 11].

Fullerenes, quantum dots are classified as zero-dimensional nanomaterials. Fullerenes of carbon (C60) are the spherical molecules made up of entirely carbon atoms. A fullerene C60 is made up of 60 carbon atoms arranged in hexagon formation to form a hollow spherical structure. Fullerenes show some unique electrical and physical properties. Quantum dots are nanocrystals having size ranging from 1- 10 nm. They are also known as artificial crystals. Cadmium telluride (CdTe), cadmium Selenide (CdSe), indium phosphide (InP), indium arsenide (InAs) are some well-known quantum dots. Nanotubes, nanowires, nano-rods are one-dimensional nanomaterials. Some examples of one-dimensional nanomaterials are carbon nanotubes, Si nanotubes, Boron nitride nanotubes.

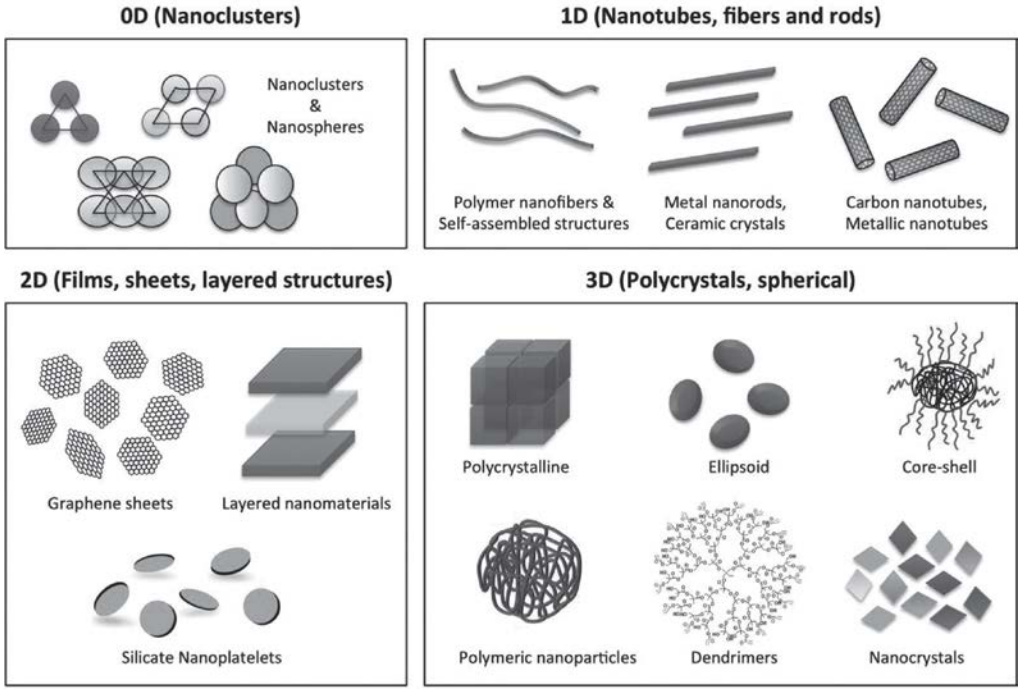

Figure 1.2.B Graphical representation on examples of 0-dimensional, 1-dimensional, 2-dimensional and 3-dimensional nanomaterials [8].

Thin films, nanosheets and nanoplates are two dimensional nanomaterial. Nanoballs (dendritic structures), nanocones, polymeric nanoparticles, nanopillers are classified as three-dimensional nanomaterials. Also they have high surface area and can provide enough absorption sites [6- 9].

1.3 Nanoparticles

In general, nanoparticle is defined as particles having size in the range of 1 - 100 nm. Nanoparticles have different chemical, physical properties such as higher specific surface areas, specific optical properties, mechanical strengths, and specific magnetizations than bulk materials. Nanoparticle research is currently a scientific interest due to their potential applications in biomedical, electronic and optical fields [10].

1.4 Applications of Nanoparticles

Nanoparticles have immense applications in almost all fields of science and human life. Use of nanoparticles in analytical systems also leads to improved sensitivity, selectivity, rapidity and portability. Ag and Pt nanoparticles have been used as catalysts in chemical reactions. In the electronic industry, metal nanoparticle paste is used for circuit pattern formation of a printed wired board. Au or Cu nanoparticles are used to make nanoparticle paste for circuit pattern formation. Metal nanoparticles such as Au and iron oxide can be used in paints. Magnetic nanoparticles have potential applications in high density magnetic recording materials. Quantum dots can be used to produce light emitting diodes (LED). In fast optical switches nanoparticles of CdS, CdSe, GaAs and Si dispersed in glasses are used. Nanoparticles such as metal nanoparticles, silica nanoparticles can be used for instrumental separation of analytes, detection and sample treatment in catalysis, gas sensing, and lubricants. Use of nanoparticles for treatment of industrial wastewater is one of the potential applications. TiO_2, Al_2O_3, ZrO_2, MnO and CeO_2, FeS, nanoparticles have potential applications in separation of environmental pollutants. Use of magnetic properties of nanoparticles (Magnetic nanoparticles) and attachment of targeted ligand can result in target specific delivery systems. This kind of delivery systems can be used in oral, nasal, intraocular etc. routes. Noble metal nanoparticles (gold, silver nanoparticles) [15] are extensively used in biosensing applications. Chitosan and Au nanoparticles have potential applications in medical diagnostics, detections and sensing applications. Extensive research has been carried out on gold and silver nanoparticles for development of molecular diagnostics, drug delivery, imaging and therapeutics. Nanoparticles like silver and copper have antimicrobial properties and can be used to kill harmful bacteria. Magnetic nanoparticles such as Fe_3O_4 nanoparticles have important potential applications in magnetic resonance imaging (MRI) and cancer hyperthermia treatment [10-16, 21, 22, 24].

1.5 Metal/ Metal Oxide nanoparticles

Metal oxides can be used in technological applications such as fabrication of microelectronic circuits, sensors, coatings for the passivation of surfaces against corrosion, piezoelectric devices, catalysts, and as fuel cells, cancer hyperthermia and other biomedical applications such as targated drug delivery. Metal oxide nanoparticles exhibit unique chemical and physical properties [17, 18]. Table 1.5 describes merits and demerits of different nanoparticle synthesis methods.

Table 1.5 Merits and demerits of different nanoparticle synthesis methods.

Type of Synthesis	Merits	Demerits	Reference
Co-Precipitation	Convenient way, simple and rapid preparative method, easy control of particle size and composition	extensive agglomeration, poor morphology and particle size distribution	[19, 20]
Thermal decomposition	producing highly monodispersed particles with a narrow size distribution	High cost, Long time synthesis reaction, high temperature	[21, 22]
Microemulsion	Monodispersed Nanoparticles with various morphology can be produced	not very efficient and difficult to scale up	[22]
Polyol	Uniform size particles can be prepared, easily to scale-up	Needs high temperature, long time	[23],[24]
Sol-Gel	low processing cost, energy efficiency, high production rate, and rapid productivity of fine	Limited efficiency, high cost	[26], [27]
Microwave	Fast heating and reaction kinetics, short reaction time, product yield can be increase	Health Hazards microwave radiations, costly microwave systems	[28]
Sonochemical	Simple, low cost, safe, environment friendly, absence of many reactants	Very small concentration of prepared NP's, particle agglomeration Very narrow	[28]
Spray pyrolysis	Finely dispersed particles of predictable size, shape and variable composition	Aggregated particles, expensive	[25]
biological synthesis	Selectivity and precision for nanoparticle	Little knowledge	[28]

	formation, Cost effective, Ecofriendly		
Laser pyrolysis	Small particle size, narrow particle size distribution, nearly absence of aggregation	Complicated, very expensive	[25]
Pulsed wire discharge method	Fast process, higher purity of NPs	Batch process, limited production, High Vacuum Systems, Costly process, contaminations in product	[28]
Chemical vapor condensation	suitable for preparing small quantities to demonstrate desired properties in the laboratory	Low production, difficult to control size and particle size distribution	[29]

1.5.1 Co-precipitation: Among the different synthesis methods co-precipitation method is a simplest method. This method also provides possibilities to modify nanoparticle's surface and particle homogeneity. In this method, co-precipitation of various salts like nitrates, sulphates, chlorides, perchlorates etc. is carried out. This co-precipitation is carried out under fine control of pH by using solutions of NaOH, NH_4OH to yield corresponding oxide nanoparticles [19, 20].

1.5.2 Thermal decomposition: Thermal decomposition method is an organic solution phase decomposition route. In this method, thermal decomposition of a metallic precursor in presence of organic surfactant is carried out. Synthesis is generally carried out at high temperature. Highly monodispersed particles with a narrow size distribution can be synthesized with this method [21, 22].

1.5.3 Microemulsion: In microemulsion method due to use of surfactant immiscible fluids like oil in water (O/W) or water in oil (W/O) become thermodynamically stable. Surfactant molecules can form a monolayer at the interphase between oil and water thus it can bridge the interfacial tension between oil and water. When microemulsion containing reactants are mixed together, due to the reaction microdroplets are formed. Due to the presence of surfactant, fine microdroplets of aqueous get trapped within surfactant molecule assembles. Microcavities stabilized by surfactant can provide locking up effect that limits particle nucleation, growth, agglomeration results in nanoparticle formation [22, 25, 28].

1.5.4 Polyol: Polyol approach uses polyols such as ethylene glycol, diethylene glycol to reduce metal salts to metal nanoparticles. A wide variety of inorganic non aggregated particles can be

prepared by using polyol method. Polyols act as reducing agent and high boiling solvent. Polyols also control particle growth and prevent aggregation of particles. In this method precursor is suspended into liquid polyol and system is heated up to boiling point of polyol. Precursor is reduced to nuclei and subsequently nanoparticles synthesized [23, 24].

1.5.5 Sol-gel: Mainly three steps such as preparation of sol, successive gelation and removal of solvent are included into sol-gel synthetic route. Sol-gel synthetic route is a versatile method. Various nanocomposites either crystalline or amorphous can be synthesized with controlled porosity in bulk amounts by using this method [30]. This method has advantages like high production rate, and rapid productivity of fine homogeneous particles and low processing cost. This method is an effective method and widely used in synthesis of metal oxides (example iron oxide, Fe_2O_3-SiO_2 nanocomposite) [24, 26, 27].

1.5.6 Microwave: Microwave radiations are used in reaction solution to synthesize nanoparticles. This is a simple rapid and easy method for nanoparticle synthesis. Microwaves with frequency ranging from 300 MHz to 300 GHz. Widely used frequency is 2.456 GHz. During the microwave synthesis method fast and homogenous conditions can be maintained. Example - copper nanoparticles, iron oxide nanoparticles [28].

1.5.7 Sonochemical: Sonochemical method was initially used to synthesize iron nanoparticles but now this method has been used for synthesis of various metal and metal oxide nanoparticles. In sonochemical method, ultrasound radiations in the range from 20 kHz to 10 MHz are applied on precursors.This enhances the reaction to synthesize nanoparticles. This is a simple method in which different metal precursors with different concentrations can be used for nanoparticle synthesis. Also size control of nanoparticle can be done by using this method [28]. Synthesis of metal oxide nanoparticles can be easily achieved by carrying out the reaction in air or oxygen atmosphere. Example- copper mamoparticles, Fe_2O_3 nanoparticles, Fe_3O_4 nanoparticles [28, 22].

1.5.8 Spray pyrolysis: In this method, solution is sprayed into different reactors then aerosol droplets undergo evaporation of solvent followed by solute condensation and drying, thermolysis of the precipitated particles at high temperature. Experimental conditions can be controlled to generate homogenous well-defined nanoparticles. This method has high production rate. This method has advantages over commonly used synthetic routes such as rapidity and continuity. Example – Fe_2O_3 nanoparticles, zinc oxide nanoparticles [25, 24].

1.5.9 Biological synthesis: Solvent medium, reducing agent and nontoxic material for nanoparticle stabilization are main parameters in biological synthesis method. There are many

reports on synthesis of nanoparticles by using bacteria [36, 37], fungi [38, 39], plants [40, 41], actinomycetes [42, 43]. Biosynthetic route is simple, easy and almost nontoxic. Synthesized nanoparticles by this method canbe used for various applications depending on their morphology. However size control of nanoparticles is sometime difficult in this synthetic route. Still this synthetic route is little known and lot of research is to be done in this method such as mechanism of nanoparticle formation, size control, tuning of reactions. Example – Fe_3O_4 nanoparticles, Silver nanoparticles, gold nanoparticles [36, 38, 40, 28].

1.5.10 Laser pyrolysis: A flowing mixture of gases is heated with a high energy and power density laser beam – either in a continuous mode or pulsed mode - to initiate and sustain a chemical reaction. Above specific laser power and pressure, a critical nuclei concentration reaches to reaction zone. This leads to homogenous nucleation of particles which is followed by transportation of particles to a filter by an inert gas. Small size, less aggregation, narrow size distribution is the main advantages of this synthetic route. Example – iron oxide nanoparticles, copper nanoparticles [25, 28].

1.5.11 Pulsed wire discharge: Pulsed wire discharge method is a physical nanoparticle synthetic route. This method is completely different as compared to other methods. In pulse wire discharge method metal wire usually copper is evaporated by using pulse current. This produces vapor and by using ambient gas this vapor is cool down to generate nanoparticles. By using pulsed discharge method synthesis of metal oxide, nitrides, and metal nanoparticles is reported. This method is simple. But this method has high production rate. This method is useful for metals available in thin wire form and with high electrical conductivity. Example – copper nanoparticles, silver nanoparticles [28].

1.5.12 Chemical Vapor Condensation: In chemical vapor condensation synthetic route rapid condensation of metallic vapor is carried out. This results in synthesis of fine grained structures. This is a very attractive, simple synthetic route mainly used for synthesis of material in small quantity in a laboratory scale. Examples – iron nanoparticles, tungsten disulphide nanoparticles [29].

1.6 Magnetite/Fe_3O_4nanoparticles properties

Magnetite (Fe_3O_4) is one of the oxides of iron. Iron oxide is present in different types such as magnetite (Fe_3O_4), maghemite (γ-Fe_2O_3), hematite (α-Fe_2O_3), goethite (α-FeOOH), ferrous oxide (FeO). Out of these magnetite (Fe_3O_4) possess both ferrous (reduced) and ferric (oxidized) phases. Magnetite is also known as iron ^{II,III} oxide. Figure 1.6.A represents oversimplified reaction of magnetite and chemical formula of each phase.

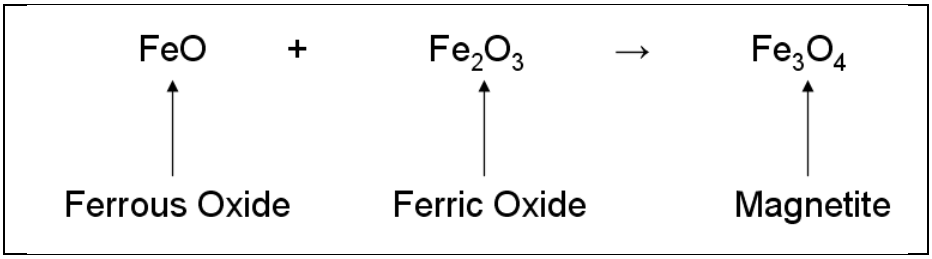

Figure 1.6. A Simplified magnetite synthesis reaction [31].

Fe_3O_4 nanoparticles have interesting properties and various potential applications. Fe_3O_4 nanoparticles have crystal structure which is an inverse spinel pattern. Alternating tetrahedral and tetrahedral-octahedral layers are present. Figure 1.6.B represents the structure of unit cell of magnetite (Fe_3O_4). Half of the octahedral lattice sites are occupied by ferrous species. The reason behind this is the higher ferrous crystal field stabilization energy (CFSE). Other octahedral lattice sites and all the tetrahedral lattice sites are occupied by ferric species. Magnetite unit cell possess face centered cubic pattern and crystal lattice parameter, $a = 0.8396$ nm. Effective surface area of magnetite nanoparticles depends upon the method used for synthesis and synthesis reaction parameters as these things affects on size of nanoparticles. Magnetite possess melting point 1590°C. Ferrous and ferric species are present in octahedral sites of magnetite. Magnetite (Fe_3O_4) crystal is an inverse spinel structure with alternating octahedral and tetrahedral layers. Due to transfer of electrons in octahedral sites between Fe^{2+} and Fe^{3+} ions, it shows magnetic and electrical properties.

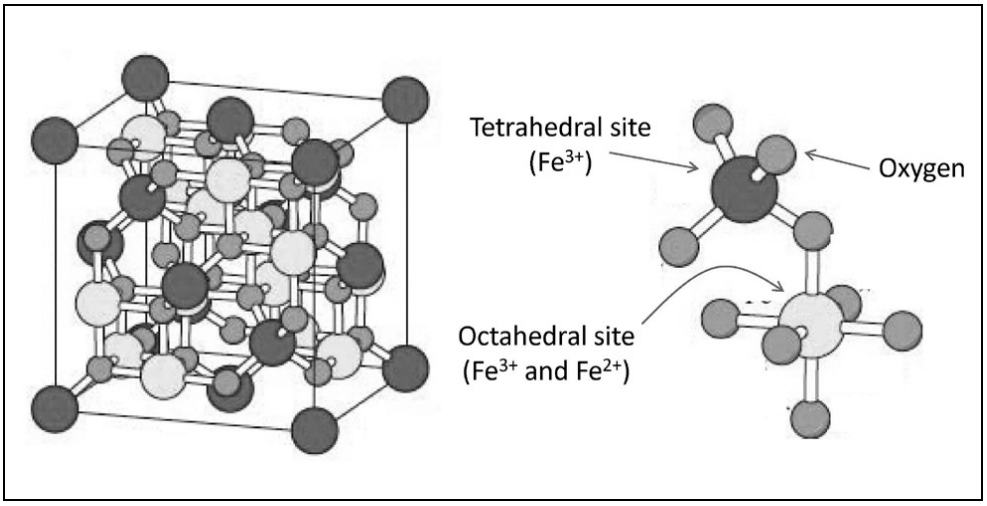

Figure 1.6.B Structure of Unit cell of magnetite (Fe_3O_4) [35].

Curie temperature in magnetite is observed to be 850 K. Magnetic moments of ontetrahedral sites (occupied by ferric species) gets aligned ferromagnetically but magnetic moments present on octahedral sites (occupied by ferrous species) gets antiferromagnetically aligned. Both the magnetic moments cancel each other and this behavior is called as ferrimagnetic behavior.

Coercivity and remanence (retentivity) is exerted by ferrimagnetism. As nanoparticle size decreases then this property tends towards paramagnetic or superparamagnetic magnetization.Therefore decrease in nanoparticle size will enhance supermagnetic behavior and decrease ferromagnetic behavior. As size of nanoparticles decreases the relative oxygen concentration decreases, therefore a slight reduction in iron valance state occurred. Because of this ferrous ion content increase, therefore increase in magnetization should be observed. Table 1.6 shows different properties of magnetite nanoparticles [31, 32].

Table 1.6 Different properties of Fe_3O_4 nanoparticles, their value and details [31].

Property	**Value**	**Details**
Band gap	0.1 eV	almost semi-conductor
color	black	suspended solutions exhibit jet black color
conductivity	102-103 /Ω/cm	almost metallic
crystal structure	inverse spinel	alternating octahedra and tetrahedra-octahedral layers
Curie temperature (nano-scale)	738 K	higher proportion of surface spins in nano-scale particles enhances the dipolar anisotropy
electrical properties	between metal and semiconductor	almost metallic good conductivity due to closeness of Fe^{2+} and Fe^{3+} ions on octahedral sites
Magnetic properties (nano-scale)	superparamagnetic	-
morphology	Octahedral crystals	bounded by {111} planes and rhombo-dodecahedra
saturation magnetization (nano-scale)	6.4 nm: 1.1 μB/fu 10.8 nm: 2.6 μB/fu 37.8 nm : 2.3 μB/fu	relative oxygen concentrations decline causing valence states of iron cations to be slightly reduced, generating greater ferrous ion content; since the ultimate magnetic moment depends upon ferrous species, subsequent increase in magnetization; below 10 nm surface effects cause saturation magnetization to decrease

1.7 Applications of Fe_3O_4 nanoparticles

Different applications of nanoparticles are explained in section 1. 4, however it is necessary to mention some important applications of Fe_3O_4 nanoparticles. Applications of Fe_3O_4 nanoparticles are biosensing, targeted drug delivery, photocatalysis etc. However because of magnetic properties of these nanoparticles provides an opportunity for applications in magnetic separation and cancer hyperthermia treatment. Figure 1.7 shows a typical example of magnetic separation process in which magnetically tagged cells (•) can be separated from the mixture of unwanted biomaterial (◦) present in a fluid.

Besides this if Fe_3O_4 nanoparticles are subjected to external alternating magnetic field, they generate heat because of losses during the magnetic reversal process during magnetization. This property can be useful in some applications such as hardening of adhesives and in cancer treatment. Hyperthermia is a type of cancer treatment in which heat is generated within a cancerous tissue. High temperature can break down/burn/kill cancer cells. However, such heat can also injure to normal tissue which is one of the major problem in hyperthermia treatments. There are different types of hyperthermia such as local, regional and whole body hyperthermia.

Heat is generated when external magnetic field is applied on Fe_3O_4 nanoparticles and magnetic losses occur due to hysteresis, Neel or Brown relaxation and frictional losses. Under the influence of thermal energy, Fe_3O_4 nanoparticles show spontaneous change in magnetization. Hence, magnetization oscillates or rotates between two equilibrium positions. Typical time between two states can be given by Neel relaxation time. If magnetic field is applied to Fe_3O_4 nanoparticles then nanoparticles align with magnetic field and rotate. Rotation of the particle is called as Brownian motion and rotation of moment within particle is called as Neel relaxation. This is because of interaction of magnetic field with the magnetization which generates the torque. The time taken by Fe_3O_4 nanoparticles to align with external magnetic field is given by Brown relaxation time. Hysteresis is generated due to delay between magnetic field rotation and magnetization rotation. Hysteresis loop generates thermal energy/heat which can be used in cancer hyperthermia treatment [32-34].

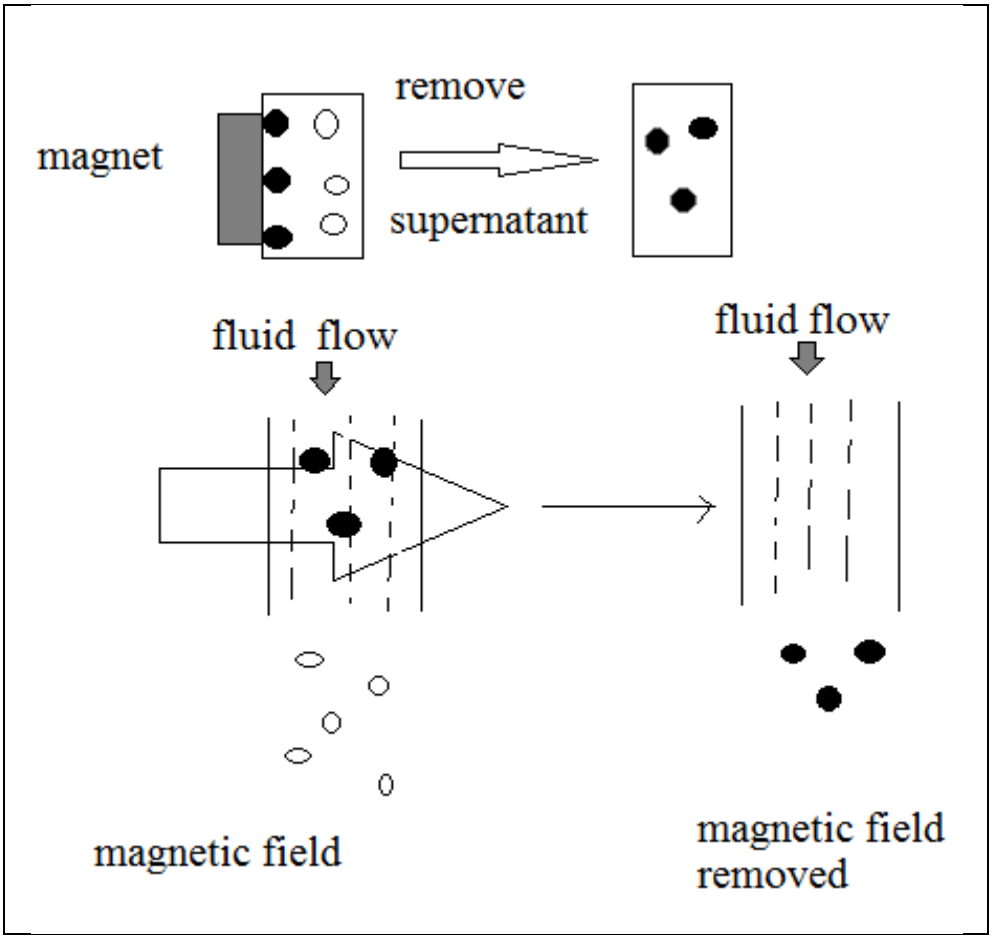

Figure 1.7 Typical example of magnetic separation process [32]

1.8 Synthesis of Fe_3O_4 nanoparticles: different methods

In recent years, extensive research work has been carried out on Fe_3O_4 nanoparticles because of their interesting magnetic and electrical properties. The performance of Fe_3O_4 nanoparticles is most importantly depends upon the method chosen for their synthesis. Physical and chemical properties of Fe_3O_4 nanoparticles and their surface also have effects on performance of these nanoparticles. A synthesis method for Fe_3O_4 nanoparticles can allow control over size, tuning of surface chemistry for getting desired properties in Fe_3O_4 nanoparticles. Some new methods for synthesis of Fe_3O_4 nanoparticles using thermal degradation of iron precursor at high temperature have been developed but such method needs very high temperature and are complicated. In thermal decomposition method, main factors are: presence of suitable organometallic precursor that decomposes below the surfactant degradation temperature, two surfactants which can differentially adsorbed on nano crystal faces and one surfactant must promote the monomer exchange between particles to achieve size distribution [44 - 46]. Fe_3O_4 nanoparticles are extensively studied for their biomedical applications such as in drug delivery, in magnetic resonance imaging (MRI), and in hyperthermia treatment of cancer [47 - 50].

Stringent requirements are there for application of Fe_3O_4 nanoparticles in bio-medical science.

Some of them are: (a) Size of the Fe_3O_4 nanoparticles should be smaller than 20 nm [51] – for their easy penetration and motion inside the human body; (b) Surface should not be capped by a capping agent typically used in chemical synthesis process of nanoparticles; thereby allowing the possibility of binding a drug molecule to the nanoparticle for further use; (c) In general, as the size of the magnetic nanoparticles decreases, critical transition temperature (T_c) decreases. This puts an additional restriction that magnetic nanoparticles should be used below T_c, in order to utilize their magnetic property. Thus, one has to choose a correct size of the nanoparticles having required critical transition temperature (T_c), suitable for its desired application; and (d) synthesis process should be highly reproducible, scalable, and low cost. Recently there are also so many advancements in synthesis of Fe_3O_4 nanoparticles by using colloidal chemical approaches. Also magnetic nanoparticles in the range of 2-20 nm can be used in applications such as magnetic storage devices, in ferrofluids, in magnetic refrigeration systems, in magnetic resonance imaging for contrast enhancement. Nanoparticles can be dispersed in organic solvents and their powder form can be retaining by removing solvents. There are some important issues or problems in nanoparticle synthesis such as monodisperse nanoparticle synthesis or particle size distribution should be uniform, synthesis of nanoparticles with high crystallinity and required crystal structure, shape control such as non-spherical or anisotropic nanoparticle synthesis, Control over particle size with high reproducibility. The size of nanoparticles can be controlled by fine tuning of reaction parameters such as reaction time, temperature, concentration of reactants and concentration of stabilizing surfactants [52].

Chemical methods (using either aqueous or organic solution), polyol method (method of reducing metallic oxide or metallic complex compound by polyol in organic solvent) are generally employed for synthesis of Fe_3O_4 nanoparticles. T. Daou et.al. have synthesized Fe_3O_4 nanoparticles of size 39±5 nm by hydrothermal reaction of 1 M ferric chloride hexa-hydrate ($FeCl_3.6H_2O$) and 2 M Ferric chloride tetra hydrate ($FeCl_2.4H_2O$) dissolved in 2 M HCl followed by slow addition of aqueous solution of tetramethyl ammonium hydroxide [$N(CH_3)_4OH$]. In this method at 70 °C co-precipitation from Fe^{2+} and Fe^{3+} ions by [$N(CH_3)_4OH$] was carried out and at 250 °C hydrothermal treatment was carried out. Very slow process and need for high temperature are the major drawback of this process [53]. In another effort by M. Mascolo et. al., Fe_3O_4 nanoparticles (63 nm±25 nm) were synthesized by co-precipitation method in alkaline condition using $FeCl_3$ and $FeCl_2$ salts. In this method initially ferrous and ferric hydroxides are prepared and these reactions are very fast. Then ferric hydroxide decomposes to FeOOH. Finally FeOOH and $Fe(OH)_2$ undergo solid state reaction to form magnetite. However, particle size is large and not really suitable for medical applications [54]. J. Lope et.al. have synthesized Fe_3O_4 nanoparticles by chemical co-precipitation method and coated with oleic acid as surfactant agent [55]. It is difficult to synthesize magnetite particles (Fe_3O_4), which have a particular stoichiometric composition by

co-precipitation method also the pH adjustment or pH control is very important and a tedious task. There are some other disadvantages of co-precipitation method such as broad nanoparticle size distribution, poor crystallization and irregular crystal shape [56]. Polyol method have its own disadvantages like it needs long synthesis time (minimum 7 - 8 hours) and high temperature (>200 °C) [56]. The exact mechanism leading to formation of Fe_3O_4 and origin of oxygen element in Fe_3O_4 is still unclear in polyol method. Several other methods have been reported for synthesis of Fe_3O_4 nanoparticles such as chemical method using plant extracts and bacteria as reducing agents [46, 57], thermal decomposition/pyrolysis of organo-metallic precursors [58-60], ultrasound irradiation [61], gamma radiolysis [62], sol-gel method [63-65] etc. Each of these methods has itsown advantages and limitations. Most of these methods yields polydisperse nanoparticles, surface capped nanoparticles, nanoparticles with impurities, in addition to poor reproducibility. It is important to select correct size of nanoparticles. At the same time, synthesis method should be highly reproducible, scalable, and economical. Different polymers and surfactants such a polyvinylalcohol (PVA) [66], poly (vinylpyrrolidone) (PVP) [67], polyethylene glycol (PEG) [68], oleic acid [69], polyacrylic acid (PAA) [70] are used for coating of Fe_3O_4 nanoparticles or as capping agent (for controlling the size of the nanoparticles during synthesis and suppressing the aggregation). This result in improved morphology, prevention of agglomeration and aggregation of nanoparticles, but such may affect the properties of nanoparticles. Also, polymers and surfactants are expensive and difficult to (naturally) decompose. Thus, their use restricts the applications of Fe_3O_4 nanoparticles in biomedical science and also can cause environmental problems.

1.9 Different mechanisms of Fe_3O_4 nanoparticle synthesis

In this section some different mechanisms are explained used to synthesize Fe_3O_4 nanoparticles.

Abedini et. al. synthesized colloidal Fe_3O_4 nanoparticles by using gamma radiolysis method. An aqueous solution containing $FeCl_3.6H_2O$ and PVA (Poly Vinyl Alcohol) and isopropanol was prepared. pH of this solution was increased to 11 by adding NaOH solution at 70 °C. Final solution was irradiated by gamma rays.

$$\mathbf{H_2O\text{---irradiation} \longrightarrow e^-, H_2, OH, H_2O_2 \text{ etc. form}}$$

$$\mathbf{Fe^{3+} + e^- \longrightarrow Fe^{2+}}$$

$$\mathbf{Fe^{2+} + 2Fe^{3+} + 8OH^- \longrightarrow Fe_3O_4 + 4H_2O}$$

Above equations show the formation mechanism for Fe_3O_4 nanoparticles. In this mechanism PVA acts as stabilizer, isopropanol and NaOH act as hydroxyl ion scavengers and stabilizers to control growth [71].

Mascolo et.al. synthesized Fe_3O_4 nanoparticles by co-precipitation reaction at room temperature and in presence of bases, such as NaOH, KOH or $(C_2H_5)_4NOH$.

$$\mathbf{2FeCl_3 + FeCl_2 + 8\ BOH \longrightarrow Fe_3O_4 + 4H_2O + BCl}$$

In above equation B = Na^+, K^+ or $(C_2H_5)_4N^+$. Following equations are proposed in this report for Fe_3O_4 formation.

$$\mathbf{Fe^{3+} + 3\ OH \longrightarrow Fe(OH)_3}$$

$$\mathbf{Fe(OH)_3 \longrightarrow FeOOH + H_2O}$$

$$\mathbf{Fe^{2+} + 2OH^- \longrightarrow Fe(OH)_2}$$

$$\mathbf{2FeOOH + Fe(OH)_2 \longrightarrow Fe_3O_4 + 2H_2O}$$

Overall reaction equation can be given as:

$$\mathbf{2Fe^{3+} + Fe^{2+} + 8OH^- \longrightarrow 2Fe(OH)_3Fe(OH)_2 \longrightarrow Fe_3O_4 + 4H_2O}$$

In this method $FeCl_2.4H_2O$ and $FeCl_3.6H_2O$ were dissolved in degassed water followed by addition of NaOH at room temperature [54].

Roonasi et. al. studied the mechanism of Fe_3O_4 formation using isotope fractionation study.In this report Fe II and Fe III alkali solutions were used. Synthesis of magnetite nanoparticles was done by coprecipitation of iron (II) and (III) and oxidation of ferrous hydroxide [72].
Overall reaction is as follows

$$\mathbf{Fe^{2+} + 2\ Fe^{3+} + 8OH^- \longrightarrow Fe_3O_4 + 4H_2O}$$

Initially precipitation of $Fe(OH)_2$ occurs after addition of iron (II) chloride solution to Sodium hydroxide solution as follows:

$$\mathbf{FeCl_2 + 2NaOH \longrightarrow Fe(OH)_2 + 2NaCl}$$

Magnetite formation starts then with oxidation of $Fe(OH)^+$ in aqueous solution.

$$\mathbf{Fe\ (OH)_{2(solid)} \longleftrightarrow\ [Fe\ (OH)]^{+}_{(aq)} + OH^{-}}$$

Then oxidation takes place as follows:

$$\mathbf{2[Fe(OH)]^{+}_{(aqueous)} + \tfrac{1}{2}\ O_2 + H_2O \longrightarrow\ [Fe_2(OH)_3]^{3+}_{(aqueous)} + OH}$$

$[Fe_2\ (OH)_3]^{3+}$ then combines with $[Fe\ (OH)]^+$. Which lead to formation of $Fe_3O(OH)_4^{2+}$ having same Fe II/Fe III ratio as magnetite. Then following equation shows how intermediate transfer to crystalline magnetite.

$$\mathbf{Fe_3O\ (OH)_4^{2+}{}_{(aq)} + 2OH^{-} \longrightarrow\ Fe_3O_{4(solid)} + 3\ H_2O}$$

Xi et.al. synthesized rod shaped Fe_3O_4 nanocrystals by poly (vinyl pyrrolidone) (PVP)-mediated hydrothermal synthesis method. Synthesis was carried out at 90 °C. In this mechanism NaOH act as pH regulator and provides OH ions, KNO_3 acts as oxidizing agent. Initially $Fe(OH)_2$ is formed and part of $Fe(OH)_2$ is oxidized to $Fe(OH)_3$ [73].
The formation of Fe_3O_4 can be explained as follows:

$$\mathbf{Fe(OH)_2 + 2\ Fe(OH)_3 \longrightarrow\ Fe_3O_4 + 4\ H_2O}$$

$$\mathbf{3\ Fe(OH)_2 + NO_3^{-} \longrightarrow\ Fe_3O_4 + NO_2^{-} + 3\ H_2O}$$

Qiaojuan et.al. have synthesized biocompatible Fe_3O_4 nanocrystals. In this method in presence of α, ω-dicarboxyl-terminated polyethylene glycol (HOOC-PEG-COOH) and oleylamine, the pyrolysis of $Fe(acac)_3$ in diphenyl oxide was carried out to synthesize Fe_3O_4 nanocrystals. Polyethylene glycol (HOOC-PEG-COOH) can form a primary amine salt with oleylamine by donating its proton, leading to the formation of OOC-PEG-COO, which then coordinates with $Fe(acac)_3$ by partly replacing the acetylacetonate ligand of $Fe(acac)_3$. The carboxylated PEG first reacts with oleylamine forming the primary amine salt, which subsequently coordinates with Fe atom in $Fe(acac)_3$ by partly replacing the acetylacetonate ligand, consequently leading to the formation of a large molecular network.This molecular network then partly breaks down and forms Fe_3O_4 nuclei. As reaction goes on Fe_3O_4 nanocrystals synthesized. Mechanism is as follows [74]:

$$\mathbf{HOOC\text{-}PEG\text{-}COOH + 2R\text{-}NH_2 \longrightarrow\ RNH_3^{+}\text{-}OOC\text{-}PEG\text{-}COO^{-+}H_3NR}$$

(Polyethylene glycol) (Oleamine) (Amine salt)

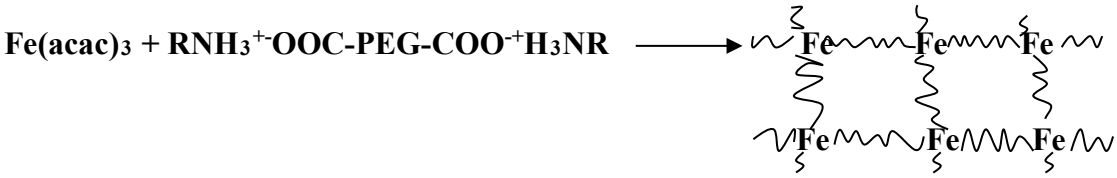

(Molecular network)

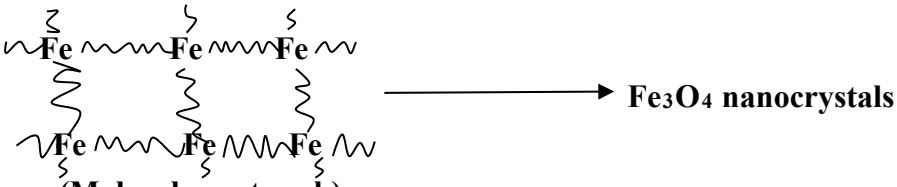

(Molecular network)

1.10 Reduction of $Fe(acac)_3$ by ascorbic acid to generate Fe_3O_4 nanoparticles

Our method is similar to the sol-gel method. $Fe(acac)_3$ (Fe(III) acetylacetonate compound) in diphenylether was reduced by ascorbic acid and hydrolyzed with using water.

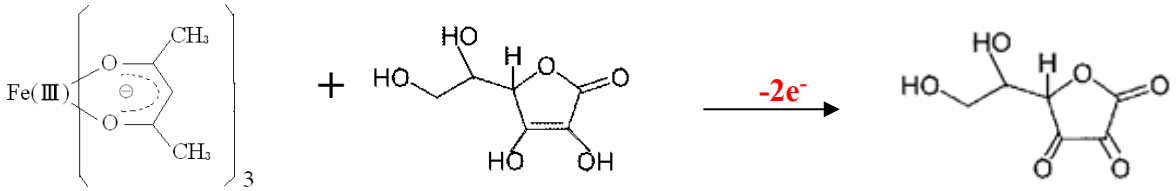

$Fe(acac)_3$ Ascorbic acid dehydroascorbic acid

$$6Fe(III)(acac)_3 + \text{ascorbic acid (act as reducer)} + 8H_2O \longrightarrow 2Fe_3O_4 + \text{dehydroascorbic acid} + 18\ acac$$

In this method, water acts as the supplier of oxygen. $Fe(acac)_3$ is reduced by ascorbic acid, then reaction mixture is heated to 190 °C for 1 hour.

1.11 Purpose of the dissertation

Fe_3O_4 nanoparticles are important because of their wide range of applications in various different fields such as magnetic storage media, rotary shaft sealing, magnetic fluid hyperthermia, drug delivery. Magnetite（Fe_3O_4）nanoparticles have been made mainly using co-precipitation method or polyol method. In the coprecipitation method, magnetite nanoparticles are synthesized by the hydrolysis of Fe^{2+} ion and Fe^{3+} ion in mole ratio of 1:2, by a base usually NaOH or NH_4OH. In such case, over all composition of the precipitate is same as that of the reaction system. But, as the hydrolysis rate of Fe^{3+} ion is greatly different from that of Fe^{2+} ion, the composition of the nanoparticle may not be same. Also pH control is important and difficult. If pH > 11, then re-dissolutions of $Fe(OH)_3$ and $Fe(OH)_2$ will begin.

$$Fe(OH)_3 \text{ ----- > } Fe(OH)_4^- \quad Fe(OH)_2 \text{ ------ > } Fe(OH)_3^-$$

Therefore, synthesis of magnetite particles (Fe_3O_4), with a stoichiometric composition, by the coprecipitation method is difficult.

In the polyol method, metal nanoparticle, such as Au nanoparticles, can be synthesized by this method. In this case, the formation mechanism of metallic nano particles is clear.

$$\text{R-C(-R')H-OH (alcohol form) ---- > R-C(-R')=O (ketone form)} + e^- + H^+$$

This electron (e^-) reduces metallic ion to metal. But the mechanism leading to Fe_3O_4 in the polyol method has not been clear yet. Especially, origin of oxygen element in Fe_3O_4 is not clear.

Synthesis of magnetite (Fe_3O_4) nanoparticles with desired size in reproducible manner is still a problem. To solve such problems this research work is focused on ascorbic acid mediated reduction of $Fe(acac)_3$ to synthesize Fe_3O_4 nanoparticles and to study or understand the mechanism of Fe_3O_4 formation. For this purpose we have examined the relationship among various reaction parameters (such as temperature, concentration, dropping rate, reflux time and temperature etc.). In order to study the effect of reaction parameters on rate of reaction and reduction of $Fe(acac)_3$ by ascorbic acid, we have examined decomposition efficiency of $Fe(acac)_3$ at different water concentrations, addition temperatures. We have also examined the effect of these reaction parameters on nanoparticle diameter and crystallinity. In a study we have optimized the synthetic conditions so as to synthesize Fe_3O_4 nanoparticles having diameter less than 30 nm for their possible applications in cancer hyperthermia or drug delivery. Further this method was extended to synthesize graphene-Fe_3O_4 nanocomposite.

References:

1. R. Amin, S. Hwang, S. Park, "Nanobiotechnology: An interface between Nanotechnology and Biotechnology", NANO: Brief Reports and Reviews 6(2), 101–111, 2011.
2. M. Roco, "Nanotechnology: convergence with modern biology and medicine", Current Opinion in Biotechnology 14, 337–346, 2003.
3. The Royal Society & The Royal Academy of Engineering, "Nanoscience and nanotechnologies: opportunities and uncertainties", chapter 4, 25-33, 2004.
4. N. Duran, P. Marcato, "Nanobiotechnology perspectives. Role of nanotechnology in the food industry: a review", International Journal of Food Science and Technology 48, 1127–1134, 2013.
5. M. Fakruddin, Z. Hossain, H. Afroz, "Prospects and applications of nanobiotechnology: a medical perspective", Journal of Nanobiotechnology 10(31), 2-8, 2012.
6. A. Alagarasi, "Introduction to nanomaterials", Chapter: 1, pp.76.
   Available from: http://www.nccr.iitm.ac.in/2011.pdf
7. V. Pokropivny, R. Lohmus, I. Hussainova, A. Pokropivny, S. Vlassov, "Introduction in nanomaterials and nanotechnology", Tartu University Press, 225p, 2007.
8. James K. Carrow, Akhilesh K. Gaharwar "Bioinspired Polymeric Nanocomposites for Regenerative Medicine", Macromol. Chem. Phys. 216, 248−264, 2015.
9. Jitendra N. Tiwari, Rajanish N. Tiwari, Kwang S. Kim "Zero-dimensional, one-dimensional, two-dimensional and three-dimensional nanostructured materials for advanced", Progress in Materials Science. 57, 724–803, 2012.
10. S. Horikoshi, N. Serpone, "Introduction to nanoparticles in microwaves in nanoparticle synthesis: Fundamentals and applications, Chapter 1, 1-24, ISBN: 9783527648122, 2013. Available at: http://dx.doi.org/10.1002/9783527648122.ch1
11. F. Einar Kruis, Heinz Fissan, Aaron Peled, "Synthesis of nanoparticles in the gas phase for electronic, optical and magnetic applications: A review", J. Aerosol Sci. 29, No. 5/6, 511-535, 1998.
12. A. Nikam, M. Ratnaparkhiand, S. Chaudhari, "Nanoparticles- an overview", Int. J. Res. Dev. Pharm. L. Sci. 3(5), 1121-1127, 2014.
13. V. Mohanraj, Y. Chen, "Nanoparticles – a review", Trop. J. Pharm. Res. 5 (1), 561-573, 2006.
14. M.Abhilash, "Potential applications of nanoparticles", International Journal of Pharma and Bio Sciences 1(1), 1-12, 2010.
15. G. Doria, J. Conde , B. Veigas , L. Giestas, C. Almeida, M. Assuncao, J. Rosa, P. Baptista, "Noble metal nanoparticles for Biosensing Applications", Sensors12, 1657-1687, 2012.
16. A. Kaur, U. Gupta, "A review on applications of nanoparticles for the preconcentration of environmental pollutants", J. Mater. Chem.19, 8279–8289, 2009.
17. Review of literatures on noble metal nanoparticles: Properties and applications, available from http://shodhganga.inflibnet.ac.in/bitstream/10603/39151/7/07_chapter%202.pdf

18. M. Fernandez-Garcia, J. Rodriguez, Metal oxide nanoparticles. In nanomaterials: inorganic and bioinorganic perspectives; Lukehart, C. M., Scott, R. A., Eds.; Wiley-Blackwell: West Sussex, U.K., 2008.
19. H. Kumar, Manisha, P. Sangwan, "Synthesis and characterization of MnO_2 nanoparticles using co-precipitation technique", International Journal of Chemistry and Chemical Engineering 3,155-160, 2013.
20. B. Wang, Q. Wei, S. Qu, "Synthesis and characterization of uniform and crystalline magnetite nanoparticles via oxidation-precipitation and modified co-precipitation methods", Int. J. Electrochem. Sci. 8, 3786 – 3793, 2013.
21. R. Betancourt-Galindo, P. Y. Reyes-Rodriguez, B. A. Puente-Urbina, et al., "Synthesis of copper nanoparticles by Thermal decomposition and their antimicrobial properties," Journal of Nanomaterials, vol. 2014, Article ID 980545, 5 pages, 2014. http://dx.doi.org/10.1155/2014/980545
22. W. Wu, Q. He, C. Jiang, "Magnetic iron oxide nanoparticles: synthesis and surface functionalization strategies", Nanoscale Res. Lett.3, 397–415, 2008.
23. W.Cai, J. Wan, "Facile synthesis of superparamagnetic magnetite nanoparticles in liquid polyols", Journal of Colloid and Interface Science 305, 366–370, 2007.
24. S. Laurent, D. Forge, M. Port, A. Roch, C. Robic, L. V. Elst, R. Muller, "Magnetic iron oxide nanoparticles: synthesis, stabilization, vectorization, physicochemical characterizations, and biological applications", Chem. Rev.108, 2064–2110, 2008.
25. P. Tartaj, M. Morales, S. Verdaguer, T. Carreno, C. Serna, "The preparation of magnetic nanoparticles for applications in biomedicine", J. Phys. D: Appl. Phys. 36**,** 182–197, 2003.
26. S. Ramesh, "Sol-Gel synthesis and characterization of $Ag_{3(2+x)}Al_xTi_{4-x}O_{11+\delta(0.0 \le x \le 1.0)}$ nanoparticles", Journal of Nanoscience, vol. 2013, Article ID 929321, 8 pages, 2013. http://dx.doi.org/10.1155/2013/929321
27. Sols, gels, and organic chemistry, Chapter-ceramic materials, 400-411, Springer New York, 2007. http://link.springer.com/chapter/10.1007%2F978-0-387-46271-4_22
28. A. Umer, S. Naveed, N. Ramzan, "Selection of a suitable method for the synthesis of copper nanoparticles", NANO: Brief Reports and Reviews.7, 1230005 (18 pages), 2012.
29. X. Dong, C. Choi, B. Kim, "Structural and magnetic characterization of Fe nanoparticles synthesized by chemical vapor condensation process", Journal of Applied Physics 92, 5380, 2002.
30. Francesco Branda (2011), The sol-gel route to nanocomposites, Advances in nanocomposites - synthesis, characterization and industrial applications, Dr. Boreddy Reddy (Ed.), ISBN: 978-953-307-165-7, InTech, Available from: http://www.intechopen.com/books/advances-in-nanocomposites-synthesis-characterizationan_d-industrial-applications/the-sol-gel-route-to-nanocomposites

31. L. Blaney, "Magnetite (Fe_3O_4): properties, synthesis, and applications" (2007). Volume 15 - 2007. Paper 5. http://preserve.lehigh.edu/cas-lehighreview-vol-15/5
32. Q. Pankhurst, J. Connolly, S. Jones, J. Dobson, "Applications of magnetic nanoparticles in biomedicine", J. Phys. D: Appl. Phys. 36, R167–R181, 2003.
33. S. Bucak, B. Yavuzturk, A. Sezer (2012). Magnetic nanoparticles: synthesis, surface modifications and application in drug delivery, Recent advances in novel drug carrier systems, PhD. Ali Demir Sezer (Ed.), ISBN: 978-953-51-0810-8, InTech, DOI: 10.5772/52115. Available from: http://www.intechopen.com/books/recent-advances-in-novel-drug-carrier-systems/magnetic-nanoparticles-synthesis-surface-modifications-and-application-in-drug-delivery
34. R. Hergt, S. Dutz, R. Muller, M. Zeisberger, "Magnetic particle hyperthermia: nanoparticle magnetism and materials development for cancer therapy", J. Phys.: Condens. Matter 18, 2919–2934, 2006.
35. A. Teixeira, J. Tristao, M. Araujo, L. Oliveira, F. Moura, J. Ardisson, C. Amorimd, R. Lago, "Iron: a versatile element to produce materials for environmental applications", J. Braz. Chem. Soc. 23 (9), 1579-1593, 2012.
36. C. Elcey, A. Kuruvilla, D. Thomas, "Synthesis of magnetite nanoparticles from optimized iron reducing bacteria isolated from iron ore mining sites", Int. J. Curr.Microbiol. App. Sci 3(8) 408-417, 2014.
37. P. Roychoudhury, P. Gopal, S. Paul, R. Pal, "Cyanobacteria assisted biosynthesis of silver Nanoparticles - a potential antileukemic agent", J Appl Phycol (2016), doi: 10.1007/s10811-016-0852-1.
38. K. Vahabi, G. Ali Mansoori, S. Karimi, "Biosynthesis of silver nanoparticles by fungus *Trichoderma Reesei*", Insciences J. 1(1), 65-79, 2011.
39. P. Mukherjee, A. Ahmad, D. Mandal, S. Senapati, S. Sainkar, M. Khan, R. Parishcha, P. V. Ajaykumar, M. Alam, R. Kumar, M.Sastry, "Fungus-mediated synthesis of silver nanoparticles and their immobilization in the mycelial matrix: A novel biological approach to nanoparticle synthesis", Nano Lett., 1, 515-519, 2001.
40. V. Kumar, S. Yadav, "Plant-mediated synthesis of silver and gold nanoparticles and their applications", J Chem Technol Biotechnol. 84, 151–157, 2009.
41. S. Iravani, "Green synthesis of metal nanoparticles using plants", Green Chem. 13, 2638–2650, 2011.
42. R. Balagurunathan, M. Radhakrishnan, R. Babu, D. Velmurugan, " Biosynthesis of gold nanoparticles by *Streptomyces viridogens* strain HM10", Indian J Biochem Biophys.48, 331-335, 2011.
43. K. Saminathan, "Biosynthesis of silver nanoparticles using soil Actinomycetes Streptomyces sp", Int.J.Curr. Microbiol.App.Sci. 4(3), 1073-1083, 2015.

44. Y. Wei, B. Han, X. Hu, Y. Lin, X. Wang, X. Deng, Synthesis of Fe_3O_4 nanoparticles and their magnetic properties, Procedia Engineering. 27, 632-637, 2012.
45. A. G. Roca, M. P. Morales, K. O'Grady, C. J. Serna, Structural and magnetic properties of uniform magnetite nanoparticles prepared by high temperature decomposition of organic precursors, Nanotechnology. 17, 2783–2788, 2006.
46. M. Senthil, C. Ramesh, Biogenic synthesis of Fe_3O_4 nanoparticles using *Tridax Procumbens* leaf extract and its antibacterial activity on *Pseudomonas Aeruginos*a, Digest Journal of Nanomaterials and Biostructures.7, 1655-1660, 2012.
47. K. Gupta, M. Gupta, Synthesis and surface engineering of iron oxide nanoparticles for biomedical applications, Biomaterials. 26, 3995–4021, 2005.
48. J. B. Mamani, L. F. Gamarra, G. E. Souza Brito, Synthesis and characterization of Fe_3O_4 nanoparticles with perspectives in biomedical applications, Materials Research.17(3) , 542-549, 2014.
49. P. Tartaj, M. P. Morales, S. V. Verdaguer, T. G. Carreno and C. J. Serna, The preparation of magneticnanoparticles for applications inbiomedicine, Journal of Physics D: Applied Physics.36, 182–197, 2003.
50. J. Motoyama, T. Hakata, R. Kato, N. Yamashita,T. Morino, T. Kobayashi , H. Honda, Size dependent heat generation of magnetite nanoparticles under AC magnetic field for cancer therapy, Bio Magnetic Research and Technology,6 (4), 1-9, 2008.
51. S. Sun, H. Zeng, Size-controlled synthesis of magnetite nanoparticles, J. Am. Chem. Soc. 124 , 8204 - 8205, 2002.
52. T. Hyeon, Chemical synthesis of magnetic nanoparticles, Chem.Commun.8, 927-934, 2003.
53. T. J. Daou, G. Pourroy,S. B. Colin, J. M. Greneche, C. U. Bouillet, P. Legare, P. Bernhardt, C. Leuvrey, and G. Rogez, Hydrothermal synthesis of monodisperse magnetite nanoparticles, Chem. Mater.18, 4399-4404, 2006.
54. M. C. Mascolo, Y. Pei, T. A. Ring, Room temperature co-precipitation synthesis of magnetite nanoparticles in a large pH window with different bases, Materials.6, 5549-5567, 2013.
55. J. Lopez, F. Gonzalez, F. Bonilla, G. Zambrano, M. Gomez, Synthesis and characterization of Fe_3O_4 magnetic nanofluid, Rev. Latin Am. Metal. Mat. 30 (1), 60-66, 2010.
56. M. Das, P. Dhak, S. Gupta, D. Mishra, T. Maiti, A. Basak, P. Pramanik, Highly biocompatible and water dispersible amine functionalized magnetite nanoparticles, prepared by a low temperature, air assisted polyol process: A new platform for bio-separation and diagnostics, Nanotechnology. 21, 12, 2010.
57. P. A. Sundaram, R. Augustine, M. Kannan, Extracellular biosynthesis of iron oxide nanoparticles by *Bacillus subtilis* strains isolated from Rhizosphere soil, Biotechnology and Bioprocess Engineering. 17, 835-840, 2012.
58. A. Angermann, J. Topfer, Synthesis of magnetite nanoparticles by thermal decomposition

of ferrous oxalate dehydrate, J. Mater. Sci. 43, 5123–5130, 2008.
59. F. Zhao, B. Zhang, L. Feng, Preparation and magnetic properties of magnetite nanoparticles, Materials Letters. 68, 112–114, 2012.
60. S. Rongrong, G. Guanhua, Y. Ran, Z. Kechao, Q. Guanzhou, L. Xiaohe, Controlled synthesis and characterization of monodisperse Fe_3O_4 nanoparticles, Chinese Journal of Chemistry. 27, 739-744, 2009.
61. L. Wang, J. S. Jiang, Preparation of Fe_3O_4 spherical nanoporous particles facilitated by polyethylene glycol 4000, Nanoscale Res Lett.4, 1439–1446, 2009.
62. G. Qiu, Q. Wang, M. Nie, Polypyrrole-Fe_3O_4 magnetic nanocomposite prepared by ultrasonic irradiation, Macromol. Mater. Eng. 291, 68–74, 2006.
63. A. Abedini, A. R. Daud, M. A. A. Hamid, N. K. Othman, Radiolytic formation of Fe_3O_4 nanoparticles: Influence of radiation dose on structure and magnetic properties, PLOS ONE.9 (3), 1-8, 2014.
64. J. Xu, H. Yang, W. Fu, K. Du, Y. Sui, J. Chen, Y. Zeng, M. Li, G. Zou, Preparation and magnetic properties of magnetite nanoparticles by sol–gel method, Journal of Magnetism and Magnetic Materials. 309, 307–311, 2007.
65. Lemine, K. Omri, B. Zhang, L. El Mirb, M. Sajieddine, A. Alyamani, M. Bououdina, Sol–gel synthesis of 8 nm magnetite (Fe_3O_4) nanoparticles and their magnetic properties, Superlattices and Microstructures. 52, 793–799, 2012.
66. R. Kurchania, S. Sawant, R. Ball, Synthesis and characterization of magnetite/polyvinyl alcohol core–shell composite nanoparticles, J. Am. Ceram. Soc. 97, 3208–3215, 2014.
67. X. Lu, M. Niu, R. Qiao, M. Gao, Superdispersible PVP-coated Fe_3O_4 nanocrystals prepared by a “One-Pot” reaction, J. Phys. Chem.112, 14390–14394, 2008.
68. A. Mukhopadhyay, N. Joshi, K. Chattopadhyay, G. De, A Facile Synthesis of PEG-Coated Magnetite (Fe_3O_4) Nanoparticles and their prevention of the reduction of Cytochrome C, ACS Appl. Mater. Interfaces 4, 142−149, 2012.
69. L. Zhang, R. He, H. Gu, Oleic acid coating on the monodisperse magnetite nanoparticles, Applied Surface Science.253, 2611-2617, 2006
70. C. Zhou, W. Zhang, M. Xia, W. Zhou, Q. Wan, K. Peng, B. Zou, Synthesis of Poly(acrylic acid) Coated-Fe_3O_4 superparamagnetic nano-Composites and their fast removal of dye from aqueous solution, Journal of Nanoscience and Nanotechnology 13, 4627–4633, 2013.
71. A. Abedini, A. Daud, M. Hamid, N. Othman, “Radiolytic formation of Fe_3O_4 nanoparticles: Influence of radiation dose on structure and magnetic properties”, Plos One. 9, e90055, 2014.
72. P. Roonasi, A. Holmgreen, “A study of the mechanism of magnetite formation based on iron isotope fractionation”, EPD Congress, 829-836, 2009.
73. Z. Xi, S. Yanfeng, Z. Lubin, “Hydrothermal synthesis, growth mechanism and magnetic property of Fe_3O_4 nanorod”, 2012.

available from: http://www.paper.edu.cn
74. Q. Jia, J. Zeng, R. Qiao, L. Jing, L. Peng, F. Gu, M. Gao, "Gelification: An effective measure for achieving differently sized biocompatible Fe_3O_4 nanocrystals through a single preparation recipe", J. Am. Chem. Soc. 133, 19512–19523, 2011.

Chapter 2: Synthesis and Characterization of Fe_3O_4 nanoparticles

2.1 Synthesis of Fe_3O_4 nanoparticles

In this thesis, we have indigenously developed a simple, efficient, and effective method for

synthesis of Fe_3O_4 nanoparticles in which $Fe(acac)_3$ in diphenyl ether is reduced by ascorbic acid and hydrolyzed by using ultrapure water. Decomposition efficiency of precursor $Fe(acac)_3$ was studied and effect of different parameters on rate of reaction was studied. In order to control the Fe_3O_4 nanoparticle size synthesis was carried out at different parameters and parameters were optimized for size controlled synthesis of Fe_3O_4 nanoparticles having different parameters. A new mechanism for synthesis of Fe_3O_4 nanoparticles by reduction of $Fe(acac)_3$ using ascorbic acid is proposed.

Chemicals used in this work were: $Fe(acac)_3$ (purity 99 %, Strem chemicals, Japan), ascorbic acid (purity 99.6 %, Wako Pure Chemicals Industries, Ltd., Japan), dehydrated ethanol (prepared and used when required in our laboratory), diphenyl-ether (purity 99 %, Wako Pure Chemicals Industries, Ltd., Japan), and Ultrapure deionized (DI) water. All the chemicals were of analytical grade.

Figure 2.1.A and Figure 2.1.B represents temperature program and synthesis scheme respectively. At the time of synthesis experiment precursor solution (by dissolving $Fe(acac)_3$ in diphenyl ether) was taken in flask and kept under constant stirring. Thermocouple and polyrecorder were used to read the temperature. Ascorbic acid solution was added in $Fe(acac)_3$ solution (dissolved in diphenyl ether) at different temperatures such as 60 °C, 70 °C, 80 °C. Then temperature was increased to 190 °C.

[Estimation of Decomposition efficiency of precursor $Fe(acac)_3$]: A study on decomposition efficiency of precursor $Fe(acac)_3$ at different parameters was carried out. Fe_3O_4 nanoparticle synthesis experiment was performed. After addition of reducing acid solution containing dehydrated ethanol, ultrapure water, and ascorbic acid, 1 mL sample was taken out by using a syringe at different time interval. Sample was diluted to 50 mL using diphenyl-ether. Ultraviolet-visible (UV-VIS) spectra of all samples were measured to estimate the concentration of precursor present at that time.

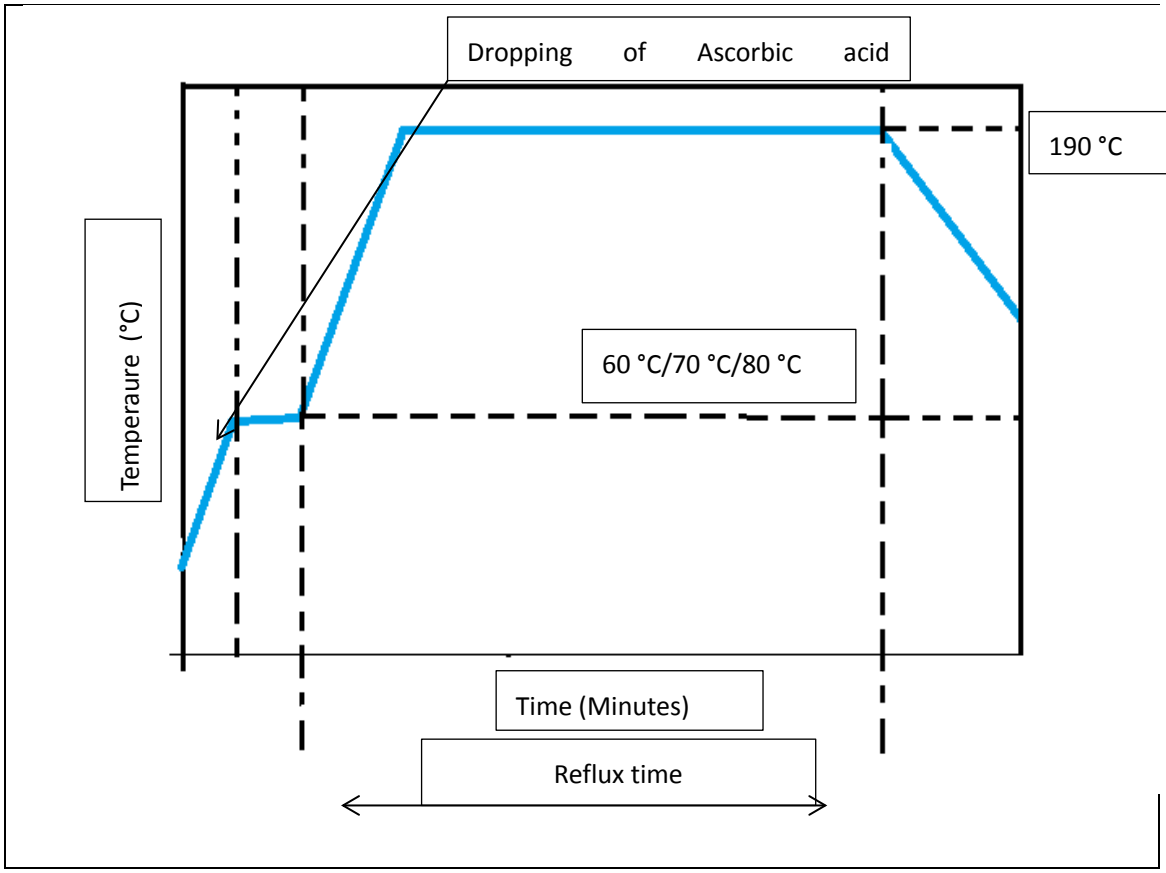

Figure 2.1.A Temperature program

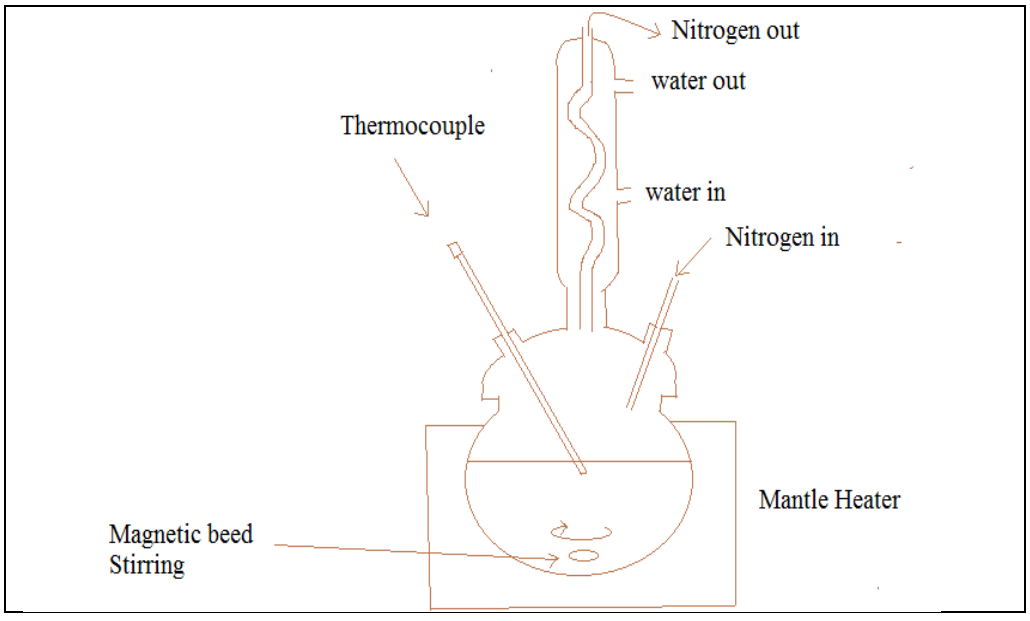

Figure 2.1.B Synthesis scheme

Experimental parameters for estimating the influence of addition temperature and ultrapure water concentration on the decomposition efficiency of $Fe(acac)_3$ precursor:

To estimate the influence of addition temperature on decomposition efficiency of $Fe(acac)_3$, addition temperature was varied from 60 °C to 80 °C. To estimate the influence of ultrapure

water concentration on decomposition efficiency of $Fe(acac)_3$ concentration of ultrapure water was varied such as 1.2 M or 2.4 M or 12 M. In reducing acid solution ascorbic acid concentration was constant (0.025 M). A dropping rate of 2 mL/min was used. 30 mM $Fe(acac)_3$ stock solution was prepared by dissolving $Fe(acac)_3$ in diphenyl ether. 50 mL of 30 mM $Fe(acac)_3$ solution was used in experiment. Before each experiment initial concentration of $Fe(acac)_3$ was estimated.

Experimental procedure for synthesis of Fe_3O_4 nanoparticles at different conditions:
50 mL of 30 mM $Fe(acac)_3$ diphenyl-ether solution was made (by dissolving $Fe(acac)_3$ in diphenyl-ether) and the solution was kept under stirring in N_2 gas atmosphere. Subsequently, temperature was increased up to preset temperature. A reducing acid solution made up of ascorbic acid, ultrapure water and dehydrated ethanol was then added at a preset dropping rate after the solution temperature reached to preset temperature. After the addition of reducing acid solution, the solution was heated to 190 °C again and refluxed for 1 hour. Finally, it was cooled down to room temperature naturally. Product was separated by filtration and washed 4 - 5 times by chloroform to remove any impurities, followed by dried in vacuum. Dry powder obtained is subsequently used for physico-chemical characterization.

Influence of addition temperature on Fe_3O_4 nanoparticle diameter and crystallinity: Addition temperature was varied as room temperature (23 °C) and from 60 °C to 80 °C. Ascorbic acid concentration was 0.025 M. Ultrapure water concentration was varied as 1.2 M and 12 M. Dropping rate of 2 mL/min was used. In case of addition temperature of room temperature (23 °C) first the addition of reducing acid solution was carried out at room temperature then temperature was increased to 60 °C then heated to 190 °C for 1 hour.

Influence of ultrapure water concentration on Fe_3O_4 nanoparticle diameter and crystallinity: Addition temperature was varied from 60 °C to 80 °C. Ascorbic acid concentration was 0.025 M. Ultrapure water concentration was varied as 1.2 M and 12 M and 0 M (in absence of ultrapure water). Dropping rate of 2 mL/min was used. In case of 0 M water concentration, reducing acid solution was made without using water and synthesis was carried out.

Influence of precursor $Fe(acac)_3$ concentration on Fe_3O_4 nanoparticle diameter and crystallinity: Precursor $Fe(acac)_3$ concentration was varied as 15 mM, 30 mM and 50 mM. Addition of reducing acid solution containing 0.025 M ascorbic acid, 12 M ultrapure water and dehydrated ethanol was carried out at 70 °C and at dropping rate of 2 mL/min.

Influence of ascorbic acid concentration on Fe_3O_4 nanoparticle diameter and

crystallinity: Ascorbic acid concentration was varied as 0.025 M, 0.005 M and 0.05 M in reducing acid solution with 12 M ultrapure water and dehydrated ethanol. Addition of reducing acid solution was carried out at 70 °C with dropping rate of 2 mL/min.

Influence of dropping rate on Fe_3O_4 nanoparticle diameter and crystallinity: Dropping rate was varied as 1 mL/min, 2 mL/min, 3 mL/min. Addition of reducing acid solution containing 0.025 M ascorbic acid, 12 M ultrapure water and dehydrated ethanol was carried out at 70 °C

Estimation of final decomposition efficiency of $Fe(acac)_3$: After the completion of Fe_3O_4 nanoparticle synthesis reaction final decomposition efficiency was estimated to investigate the amount of $Fe(acac)_3$ precursor utilized in the reaction. After heating at 190 °C for 1 hour reaction mixture was cooled down to room temperature, 1 mL sample was taken out by using syringe and diluted to 50 mL using diphenyl ether. It was observed that colour intensity of solution was so much reduced after the completion of reaction this may be due to maximum utilization of $Fe(acac)_3$. Black coloured particles of the product were suspended in this sample. UV- visible spectra of this sample was measured and absorbance at maximum wavelength was recorded. From the calibration curve amount of $Fe(acac)_3$ in this sample was estimated. Final decomposition efficiency of $Fe(acac)_3$ was calculated using the formula.

2.2 Characterization techniques used

In this section, an introduction to characterization techniques used for analysis is presented. This work was mainly focused on establishment of a new reproducible synthetic route for Fe_3O_4 nanoparticles by ascorbic acid mediated reduction of $Fe(acac)_3$ in which size control is possible by controlling various reaction conditions. Synthesized nanoparticles or nanocomposites were analyzed for their size, crystallinity, crystal structure, elemental analysis and to understand their chemical composition and structure.

Most of the techniques such as spectroscopic and microscopic ones are based on the interaction of radiation with matter. Light (electromagnetic waves) or beam of particles (electron, proton, neutron) can be used for material analysis [1]. Electromagnetic waves are made up of electromagnetic field. This electromagnetic field is characterized by its frequency (ν) and wavelength (λ). The energy of electromagnetic waves can be calculated by $E = h\nu$, where h is the Planck's constant. Classification of electromagnetic waves based on their energy/frequency/wavelength is shown in Fig. 2.2.A [2]. Interaction between matter and waves is dependent upon the wavelength. For example characteristic atomic bonds can be identified

when infrared light interacts with the molecular vibrations while the characteristic atomic structure/composition can be recognized when X-rays are scattered in the solid material and/or excite electrons [3]. The particle beams are characterized by particles moving with a characteristic velocity (υ) and wavelength (λ). The de Broglie equation correlates these parameters with the particle mass m, based on the wave-particle duality: $\lambda = h / m \upsilon$. Examples are neutron, electron and ion beams.

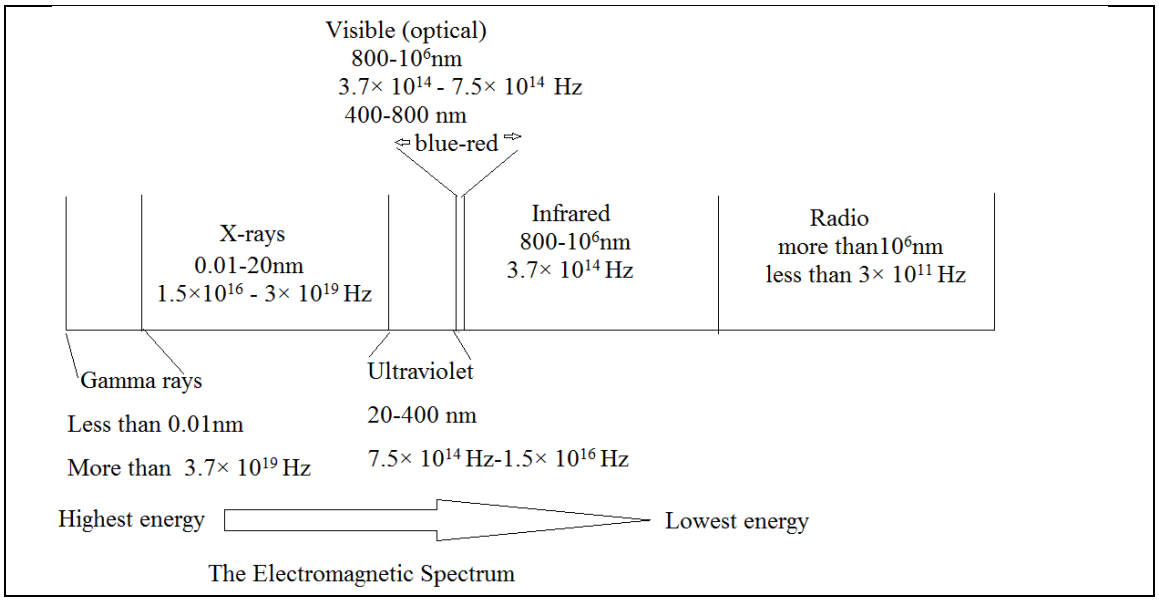

Figure 2.2.A Classification of different electromagnetic waves [2].

In this work powder samples of Fe_3O_4 nanoparticles were characterized by X-ray powder diffraction (XRD) using a Rigaku RINT-2100 X-ray diffractometer (Japan) with CuK_α radiation (λ =1.5406 nm). Transmission electron microscopy (TEM) images were obtained from JEOL JEM-2100F (USA) microscope. X-ray photoelectron spectroscopy (XPS) was done using UlVac Phi Versa Probe CU (Japan). Raman Spectroscopy was also performed using Renishaw InVia Raman Microscope (Japan). FTIR analysis was performed by using Perkin Elmer SpectrumOne (Japan).

(a) X-Ray Diffraction (XRD)

A periodic arrangement of atoms or molecules that form a crystal lattice is present in a crystal/crystalline material. A crystal structure with regularly spaced atoms can diffract X-rays. The sample is usually excited with monochromatic radiation of a known wavelength. This can determine the lattice planes with particular Miller indices (hkl) of the analyzed compound. X-rays hit a parallel lattice planes at an angle of θ. Then every atom within the planes acts as a scattering center and emits a secondary wave. Coherent scattering of X-ray by crystalline

substance is called as diffraction. Diffracted waves from different atoms can interfere with each other. By this interaction, the resultant intensity distribution is strongly modulated. If in a crystal, atoms are arranged in a periodical manner then the diffracted waves will have sharp interference peaks with similar symmetry as that of distribution in atoms.

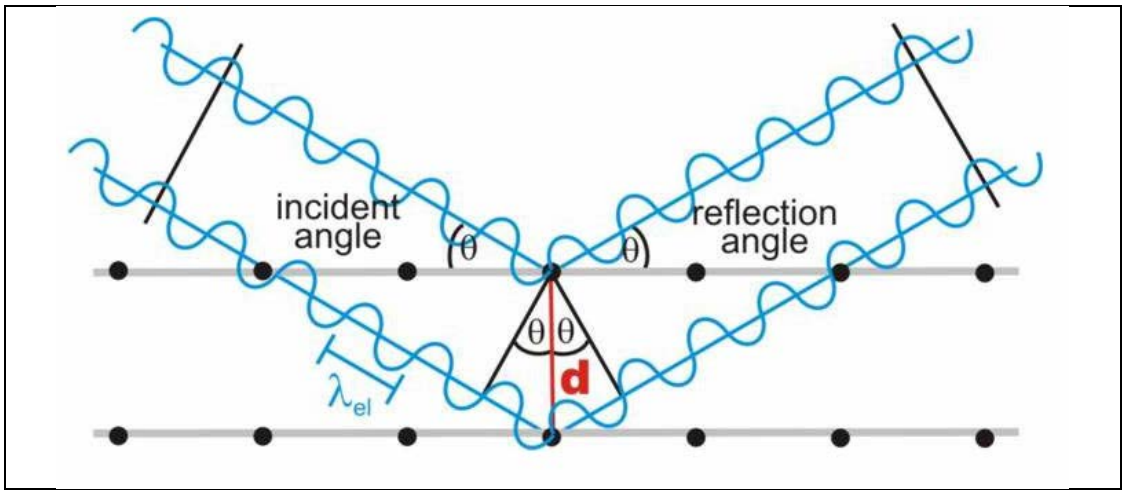

Figure 2.2.B X-ray diffraction in a crystal [4].

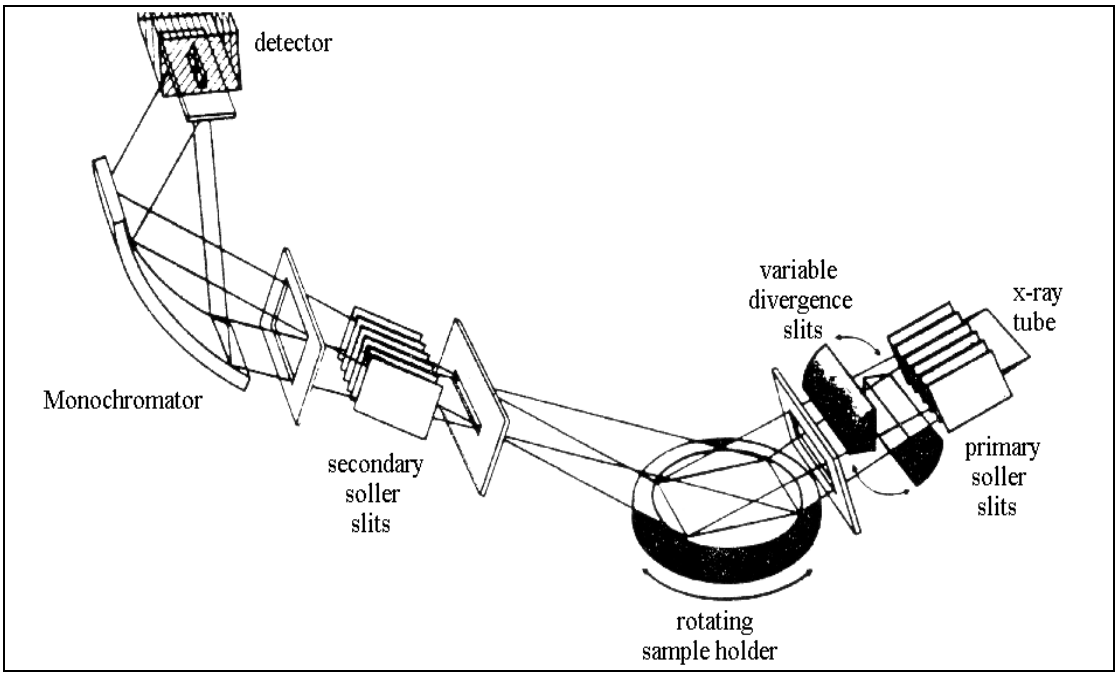

Figure 2.2.C Schematic of the powder diffractometer instrument adapted from [5]

Figure 2.2.B shows radiations that are reflected with an angle equal to θ which then reach the detector. For a given set of lattice plane, if the inter-planer distance is d then the condition for a diffraction peak to occur can be given as $n\lambda = 2d\sin\theta$. This is known as Bragg's law. In the equation, θ is the scattering angle, λ is the wavelength of X-ray, and n is an integer that represents the order of the diffraction. The Bragg's law is used for interpretation of X-ray diffraction data. Figure 2.2.C shows schematic of the powder diffractometer. X-ray

diffractometer works in step scan mode and operated with θ/2θ. The result is a diffraction pattern I (2θ) with peaks corresponding to *hkl* reflections. The position of these peaks provides Braggs reflection/diffraction angles or corresponding interplanar spacing and the intensity of reflections. These are like finger prints of structural phases and allow the identification of the sample. By using three strongest diffraction peaks most of the crystalline species can be identified. The identification can be done by comparing obtained diffraction patterns with references stored in database. XRD is one of the most applied analysis method in characterization because it identifies the crystalline structure, quantitative analysis can be done. Also it is a nondestructive, fast, simple and very small amount of sample is needed for analysis. Crystallite size from the diffraction pattern can be calculated by using scherrer equation. Scherrer equation is as follows:

$$t = K\lambda / B \cos\theta$$

Where, t is mean size of crystalline domains which may be smaller or equal to grain size, K is dimensionless shape factor and the shape factor has typical value of 0.9 but varies with the actual shape of crystallite, λ is X-ray wavelength, B is FWHM or the line broadening at half the maximum intensity, after subtracting the instrumental line broadening, in radians. θ is the Braggs angle [1].

(b) Electron Microscopy (EM)

Ordinary optical microscope uses visible light (400 nm to 800 nm). The resolution of the microscope depends on the wavelength of light used. The maximum resolution of the optical microscope is about 1 micron. For achieving better resolution electron microscopes were developed. Associated wavelength (λ) of electrons can be calculated by the De Broglie equation. De Broglie equation can be given as $\lambda = h / m_e \nu$ where ν is the particle velocity, h is Planck constant ($h = 6.63\times10^{-34}$ Js) and m_e is mass of electron ($m_e = 9.11\times10^{-31}$ Kg). Velocity of electron should be ca. 100km / s for obtaining resolution of 1 nm. To achieve this speed of electron 100 kV voltage is required. Electron beam is focused in electron microscopes using electro-magnetic lense. There are two major types of electron microscopies viz. Scanning Electron microscopy (SEM) and Transmission electron microscopy (TEM). SEM analyses surface of the sample while in TEM electron beam passes through sample. In TEM, when the beam is passed through sample image is formed due to interaction of electrons transmitted through the specimen. Image is magnified and focused onto fluorescent screen (imaging device) or detected by CCD camera (sensor). High resolution imaging is possible in TEM (Transmission Electron Microscopy) due to the small de Broglie wavelength of electrons. TEM is one of the major analysis techniques in variety of scientific fields in both biological and physical sciences.

A schematic of TEM instrument is shown in Figure 2.2.D. In TEM instrument electrons are generated by electron gun. An emission source is usually a tungsten filament or a lanthanum hexaboride (LaB_6) source. Tungsten filament will be either hair pin style filament or a small spike shaped filament. LaB_6 source will be small single crystals.

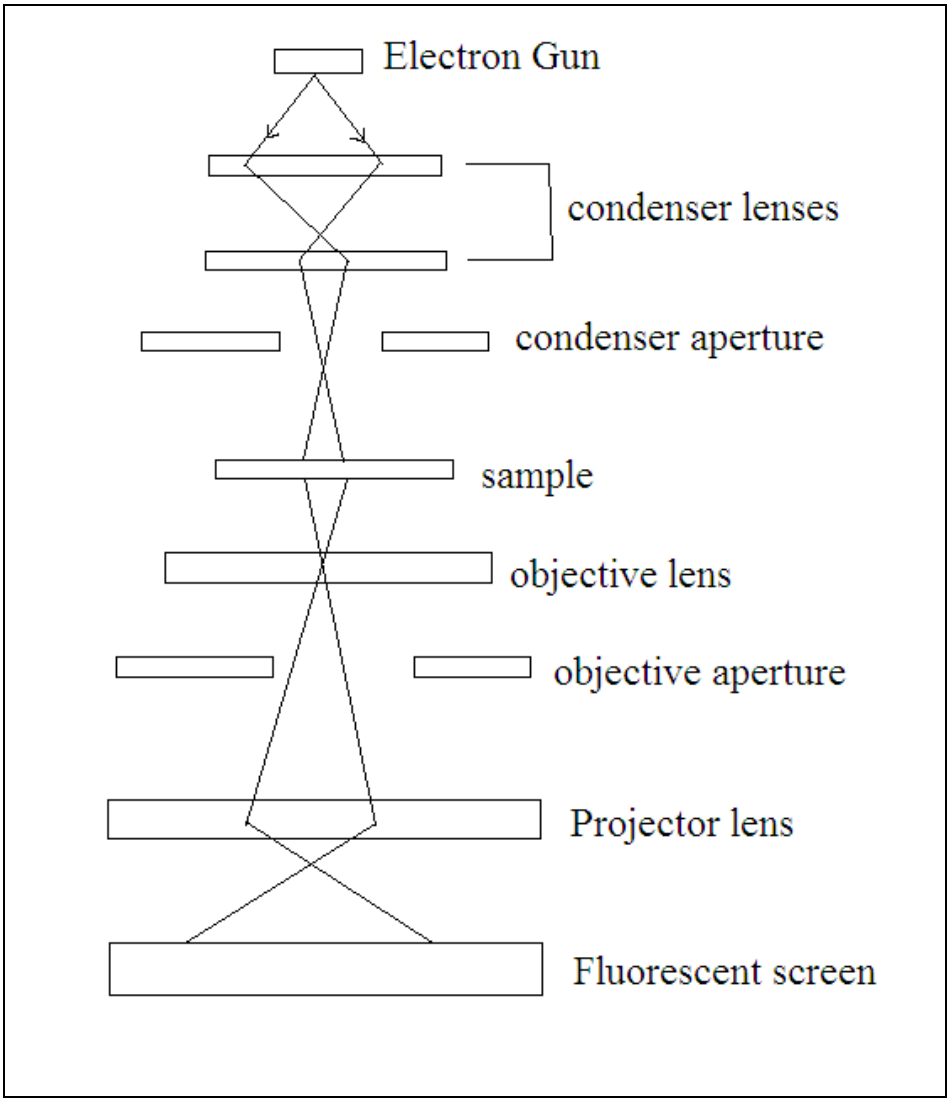

Figure 2.2.D A Schematic representation of TEM.

The electron gun is connected to high voltage source (about 100-300 kV. At sufficient current, gun will emit electrons either by thermionic emission or field electron emission. Electron beam is manipulated in two ways. Firstly electromagnets can manipulate electron beam. Secondly magnetic fields allow formation of a magnetic lens with variable focusing power. Also electrons are deflected at a constant angle due to electrostatic field. There is formation of shift in beam path due to coupling of two deflections in opposing direction with small intermediate gap.

A TEM instrument is consists of three different types of lenses such as condenser lenses, objective lenses and projector lenses. Condenser lenses are responsible for primary beam formation. Objective lenses focus the beam down onto the sample. The projector lenses expand the beam onto phosphor screen or imaging device. For direct observation the imaging system in TEM is consist of phosphor screen made up of fine zinc sulphide particles. Image recording system also have CCD camera. In TEM, voltage varies between the different models from 100 kV to 400 kV. The resolution in TEM achieved is 0.5 nm, which is much higher than the SEM. The energy of electrons determines the relative degree of their penetration in a specific sample. By this useful information can be obtained. In TEM electrons are accelerated in the same manner as in SEM but electrons get passed through sample. For avoiding the blocking of electron beam, sample must be flat and thin (5-100 nm). Transmitted electrons strike to the phosphor screen which is positioned below the sample and light is generated, showing the image. Darker areas in image represent those regions of sample through which fewer electrons were transmitted, (e.g. they are denser or thicker). In TEM, high spatial resolution can be obtained. TEM can be employed for determination of the detailed crystallography of the material. TEM is a complimentary tool to other crystallographic techniques like XRD [7 - 9].

Figure 2.2.E shows schematic of SEM instrument. In SEM maximum 10 nm resolution can be obtained and the used voltage can be varied between 10-14 kV. An area of the specimen is rapidly scanned by electron beam which is forced by the scanning coils. Electrons get reflected from the surface. The current of these reflected electrons is collected, amplified and plotted as 2D micrograph image of the intensity of signal. In the secondary and backscattered electron mode samples can be observed. Chemical analysis can be done by using Energy dispersive spectroscopy. Secondary electron mode is the most common imaging mode. It monitors low energy (≤50 eV) secondary electrons (SE). These electrons originate within few nanometers from the surface and have low energy. The brightness of signal is directly proportional to the number of electrons that reaches to detector. Depending on the tilt angle of sample surface the secondary electrons are reflected differently. Because these emissions are higher and also shadow contrast is generated. Therefore steep surface and edges tend to be brighter as compared to flat surfaces. This results in well-defined topographical with 3D-appearance. In backscattered mode backscattered electrons are high energy electrons (greater then 50 eV). These electrons undergo multiple elastic scattering events within the specimen. It can be used to detect the contrast between areas with different chemical composition [7, 8].

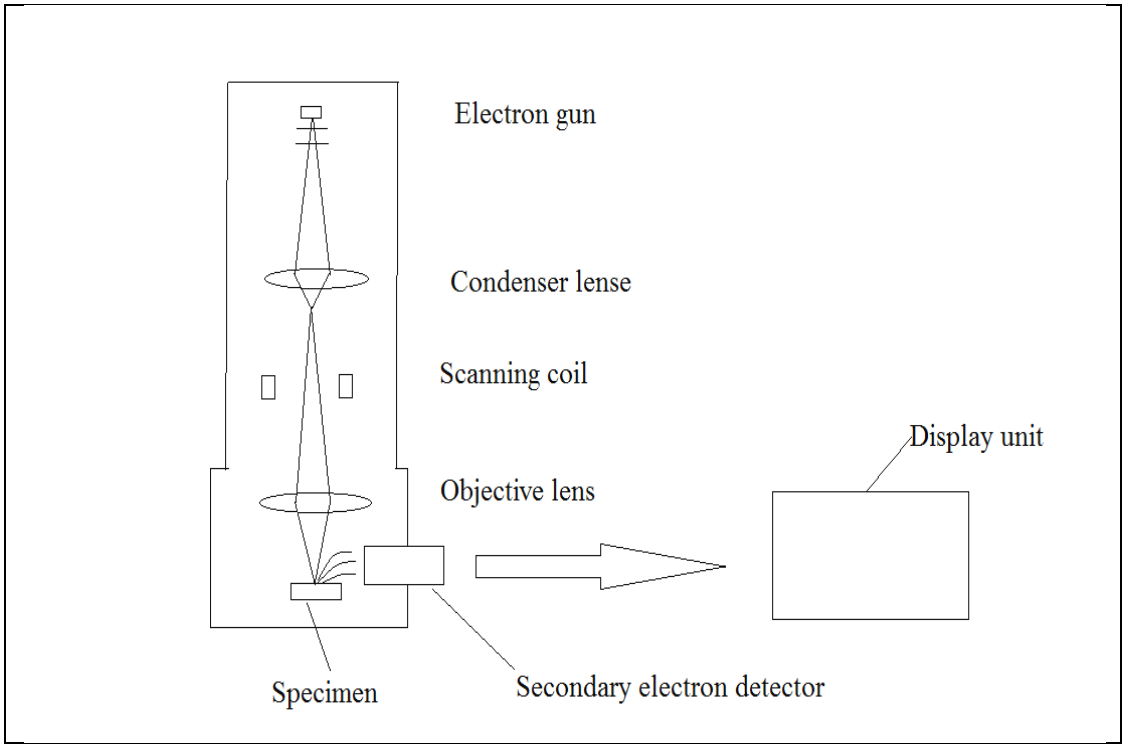

Figure 2.2.E Schematic of Scanning Electron Microscopy [6].

(c) Energy Dispersive X-ray Spectroscopy (EDS)

When a high energy beam of charged particles such as electrons or protons is focused into sample then there is characteristic X-rays emission from the sample. Atoms within the sample contain unexcited electrons in discrete electron shells bound to the nucleus. In presence of incident beam electron in inner shell get excited thus ejecting from the shell creating hole. An electron from the outer shell fills the hole. Due to the difference between higher energy shell and lower energy shell X-rays are released and measured. Energies of the X- rays are characteristic of the atomic structure of the element and difference between two shells the elemental composition of sample can be measured in EDS (energy dispersive X-ray spectroscopy) [10].

(d) UV-visible Spectroscopy

A UV-spectrophotometer measures the intensity of the light passing through sample (I_0), in comparison to its incident intensity (I_0) as shown in Figure 2.2.F. The ratio I/I_o is called the transmittance and is usually expressed in terms of (% T).

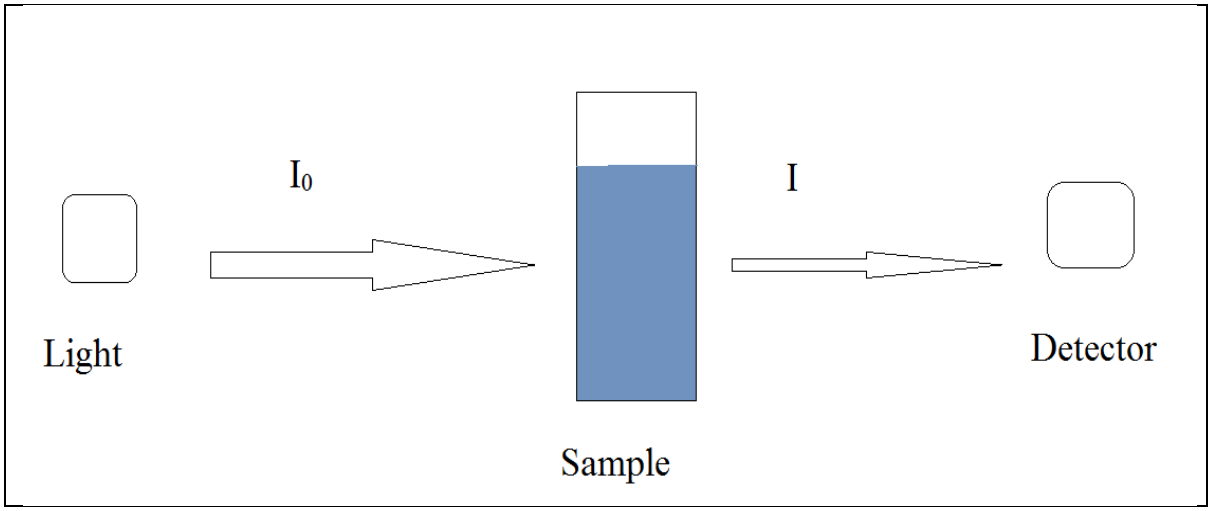

Figure 2.2.F Schematic of transmission measurement by UV spectroscopy.

Basic parts of spectrophotometer are: spectrometer for generating light (often an incandescent bulb for the visible wavelengths and a deuterium arc lamp in the ultraviolet), a holder for the sample, a monochromator to separate the different wavelengths and a detector. The detector is typical photodiode. A spectrophotometer can be either single beam or double beam. In single beam instrument the whole light passes through the sample cell. I_0 must be measured by removing the sample. In double beam instrument light splits into two beams before it reaches to sample. One beam is reference while other beam passes through sample. Samples are usually placed in cuvettes which are transparent cells.

Beer- Lamberts law can be used to measure the absorbance of particular sample and to deduce the concentration of the sample from the measurement. Beer-Lambert law can be given as:

$$\mathbf{A = \varepsilon \times l \times c}$$

Where, A is absorbance, ε is the molar extinction coefficient, l is the path length and c is the concentration [11, 12]. In present thesis, decomposition efficiency is calculated by using UV-spectrophotometry. Molar extinction coefficient of $Fe(acac)_3$ complex at maximum wavelength is 4000 ± 100.

(e) Fourier Transform Infrared Spectroscopy (FTIR)

Infrared spectroscopy method is based on the vibrations of atoms in a molecule. By passing infrared radiations through samples an infrared spectrum in obtained. By determining fraction of incident radiations absorbed at a particular energy spectrum is obtained. The energy at which peaks of spectrum occurs corresponds to frequency of a part of sample molecule.
A molecule should possess electric dipole moment which changes during the vibration to show

infrared absorptions. Interaction of infrared radiations with matter can be studied in terms of changes in molecular dipoles associated with vibrations and rotations. Atoms in molecule can move relative to one another. These kinds of movements are called as stretching or bending movements and can be termed as vibrations. Figure 2.2.G shows the components in FTIR [13].

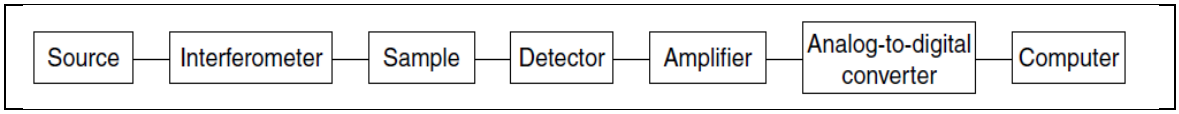

Figure 2.2.G Different components in FTIR [13].

(f) X-ray Photoelectron Spectroscopy (XPS)

When an X-ray is bombards a sample some electrons become excited enough to escape the atom, this is called as photoemission principle. When a sample is irradiated by X- rays with sufficient energy, electrons in specific bound state are excited. In XPS, sufficient energy is input to break away the photoelectron from the nuclear attraction force of an element. When electrons are ejected from surface of sample, they are energy filtered by hemispherical analyzer (HAS). Energy takes place before a detector records the intensity for a defined energy. The resulting energy spectra exhibit resonance peaks characteristic of the electronic structure for atoms at the surface because the core level of electrons in solid state atoms are quantized. The escape depth of electrons is limited though X-rays may penetrate deep into the sample. In terms of the binding energy of electronic states of the atom, the energies of photoelectron lines are well defined. Also at the surface, chemical environment of atoms results in well-defined energy shifts to the peak energy. In conducting samples detected electron energies can be referred to the Fermi energy. Also absolute energy scale can be established for identification of species. But in non-conducting samples energy calibration is a significant problem. XPS is a quantitative technique in which the number of electrons recorded for a given transition is proportional to the number of atoms present at the surface [14].

(g) Raman Spectroscopy

Raman spectroscopy is type a spectroscopic technique which is based on inelastic scattering of monochromatic light, usually from a laser source. Frequency of photons in monochromatic light changes upon interaction with a sample and this phenomenon is known as inelastic scattering of monochromatic light. For molecules it is called as Rayleigh scattering. The light interacts in Raman spectroscopy and distorts (polarizes) the cloud of electrons round the nuclei to form short lived state. This state is called as virtual state. In the scattering process energy will be transferred either from the molecule to the scattered photon or from the incident photon to the molecule. In such cases process is inelastic and the energy of the scattered photon is

different from that of the incident photon by one vibrational unit. This phenomenon is known as Raman scattering. A Raman system typically consists of four major components such as: Excitation source (Laser), Sample illumination system and light collection optics, wavelength selector (Filter or Spectrophotometer), detector (Photodiode array, CCD or PMT). A sample is normally illuminated with a laser beam in the ultraviolet (UV), visible (Vis) or near infrared (NIR) range. Scattered light is collected with a lens and is sent through interference filter or spectrophotometer to obtain Raman spectrum of a sample [15].

References

1. J. P. Eberhart, "Structural and chemical analysis of materials, John Wiley & Sons, 1991.
2. Electromagnetic radiation", by Nick Strobel at www.astronomynotes.com
3. I. Perez-Juste, O. N. Faza, "Interaction of radiation with matter, in structure elucidation in organic chemistry: The search for the right tools", (eds M.-M. Cid and J. Bravo), Wiley-VCH Verlag GmbH & Co. KGaA, Weinheim, Germany. Doi: 10.1002/9783527664610.ch1, 2015.
4. http://www.microscopy.ethz.ch/images/bragg_welle.jpg., 2008.
5. H. Krischner, B. Koppelhuberbitschnau, Rontgenstrukturanalyse , Rietveldmethode, 5th. ed. vieweg & sohn, 1994.
6. http://www.jeol.co.jp/en/science/sem.html
7. R. Erington, "Physical principles of electron microscopy", Springer publications, ISBN-10: 0-387-25800-0, 2005.
8. S. Amelinckx, D. van Dyck, J. van Landuyt, G.van Tengeloo, "Handbook of Microscopy: Application in materials science", solid-state physics and chemistry, VCH Verlagsgesellschaft mbH, 1997.
9. Williams, D.; Carter, C. B., "Transmission electron microscopy"; Springer: New York, 3 − 22, ISBN: 978-0-387-76501-3, 2009.
10. D. Peacor, "Analytical electron microscopy: X-ray analysis", chapter 4,available from: http://www.phy.pmf.unizg.hr/~andelka/Odabrana%20poglavlja%20OF/analitical_em_X_ray_analysis.pdf
11. J. Hardesty, "Spectrophotometry and the Beer-Lambert law: An Important Analytical Technique in Chemistry", available from: http://www.collin.edu/chemistry/Handouts%202009/Beer's%20Law.pdf
12. M. Fox, "Optical properties of solids", Oxford University Press, USA, 2002.
13. B. Stuart, "Infrared Spectroscopy: Fundamentals and applications", Willy, 2004, ISBN: 978-0-470-85428-0.
14. Casa XPS Manual 2.3.15 Rev 1.2, Introduction to XPS and AES, available from: http://www.casaxps.com/

15. W. Smith, G. Dent, “Modern Raman spectroscopy – A Practical Approach”, John Wiley & Sons, Ltd ISBNs: 0-471-49668-5, 2005.

Chapter 3: Synthesis and growth mechanism of Fe_3O_4 nanoparticles

3.1 The influence of synthesis parameters on the decomposition efficiency of $Fe(acac)_3$

3.1.1 Determination of $Fe(acac)_3$ concentration

The concentration of precursor $Fe(acac)_3$ present in each sample was calculated from absorbance at maximum wavelength. $Fe(acac)_3$ has the maximum absorption at about 440 nm because of existence of Fe ion in the structure of acetylacetone and pure acetylacetone does not have any of this kind of absorption peak [1-3]. According to Beer- Lamberts law:

$$\mathbf{A = \varepsilon \times l \times c}$$

Where, ε is the molar absorptivity, A is the absorbance, l is the path length and c is the concentration. When sample is placed in matched cuvettes, l is constant and ε × l is a constant. Therefore according to Beer-Lamberts law absorbance is directly proportional to concentration. By using this relation, a calibration curve was plotted. For making calibration curve different concentrations of $Fe(acac)_3$ solution in diphenyl ether were prepared such as 0.1 mM, 0.125 mM, 0.25 mM, 0.5 mM, 1 mM and absorbance at maximum wavelength was recorded for each concentration. A plot of the concentration (horizontal axis) and the absorbance (vertical axis) was prepared from the recorded data as shown in Figure 3.1.1. While calculating the $Fe(acac)_3$ concentration in sample this calibration plot was used. In the decomposition efficiency experiments absorbance of samples at maximum wavelength was recorded. From the calibration plot $Fe(acac)_3$ concentration for corresponding absorbance was calculated.

This precursor $Fe(acac)_3$ concentration estimated in sample is not reacted precursor or amount of precursor present in solution at that time. A stock solution of 30 mM of 250 mL $Fe(acac)_3$ in diphenyl ether was prepared, 50 mL (from the stock solution of 30 mM, 250 mL $Fe(acac)_3$ solution in diphenyl ether) solution was used in experiment and before each experiment initial concentration of $Fe(acac)_3$ solution was estimated. The decomposition efficiency was calculated by the following equation:

$$\text{Decomposition efficiency} = \frac{\text{Initial concentration} - \text{not reacted}}{\text{Initial concentration}} \times 100$$

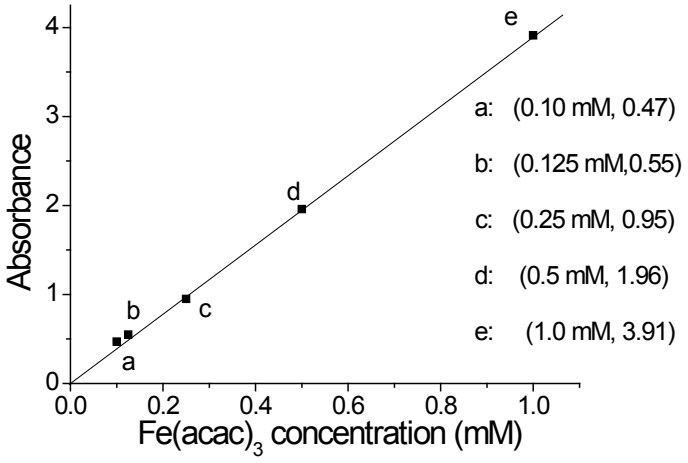

Figure 3.1.1 Calibration curve for determinatrion of $Fe(acac)_3$ concentration.

3.1.2 Influence of addition temperature

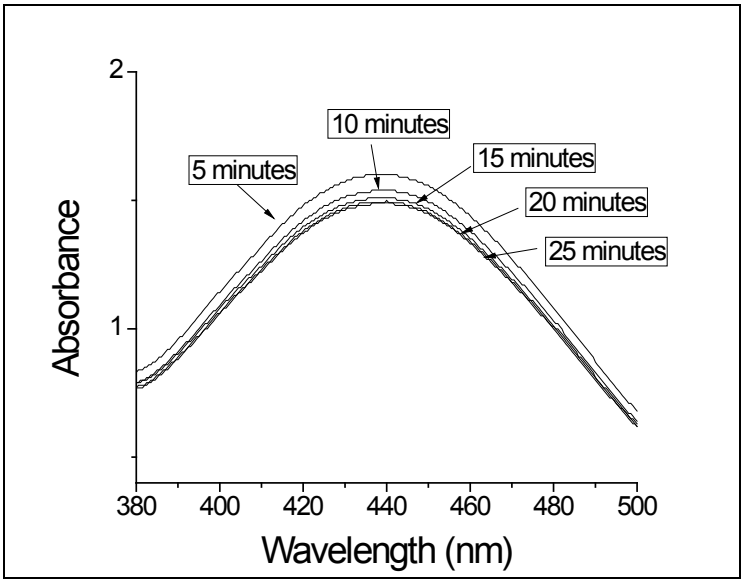

Figure 3.1.2.A UV-visible spectra of samples taken at different time interval and when addition carried out at 60°C. $[Fe(acac)_3]$ = 30 mmol/L (V = 50 mL), Reducing acid solution containing [ascorbic acid] = 25 mmol/L, [water] = 1.2 mol/L, Dropping rate: 2 mL/min, Volume of the reducing solution: 10 mL.

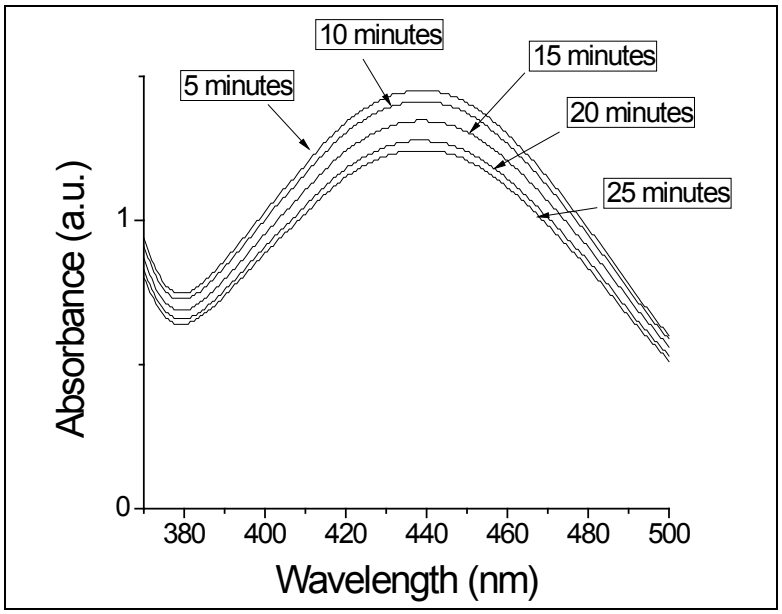

Figure 3.1.2.B UV-visible spectra of samples taken at different time interval and when addition carried out at 70 °C. [$Fe(acac)_3$] = 30 mmol/L (V = 50 mL), Reducing acid solution containing [ascorbic acid] = 25 mmol/L, [water] = 1.2 mol/L, Dropping rate: 2 mL/min, Volume of the reducing solution: 10 mL.

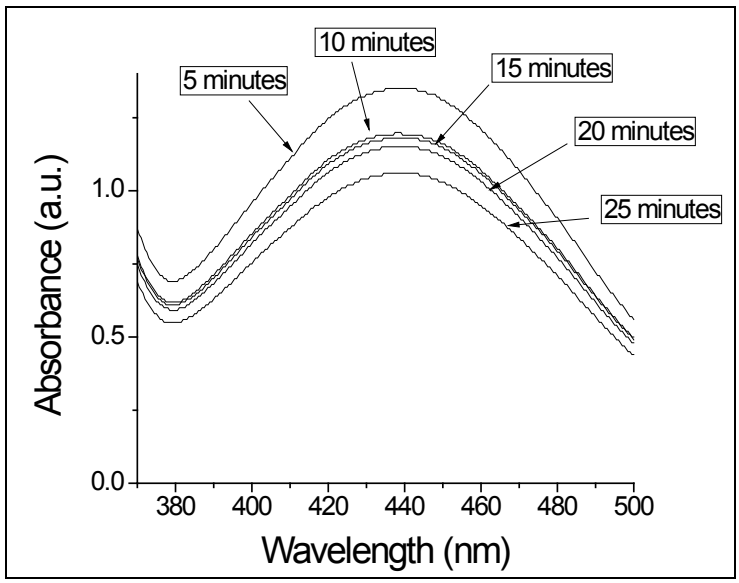

Figure 3.1.2.C UV-visible spectra of samples taken at different time interval and when addition carried out at 80 °C. [$Fe(acac)_3$] = 30mmol/L (V = 50 mL), Reducing acid solution containing [ascorbic acid] = 25 mmol/L, [water] = 1.2 mol/L, Dropping rate: 2 mL/min, Volume of the reducing solution: 10 mL.

Figures 3.1.2 (A, B, C) are the UV-visible spectra at 1.2 M ultrapure water concentration and reducing acid (ascorbic acid) solution addition temperature of 60 °C, 70 °C and 80 °C

respectively. In these results UV-visible spectra were measured at different time interval after addition of reducing acid solution containing ascorbic acid. It is observable that absorbance (at λ_{max}) decreases as the synthesis reaction proceeds which means that the precursor $Fe(acac)_3$ gets decomposed and consumed in the reaction. It is observed that $Fe(acac)_3$ solution shows maximum absorption at 440 nm (λ_{max}).

Table 3.1.2.D Absorbance, $Fe(acac)_3$ Initial – $Fe(acac)_3$ not reacted concentration at different time interval and addition temperatures and at 1.2M ultrapure water concentration.

Sample from addition started	At 60 °C 1.2M H_2O (stock=28 mM)	Decomposed $Fe(acac)_3$ (mM)	At 70 °C 1.2M H_2O (stock=28 mM)	Decomposed $Fe(acac)_3$ (mM)	At 80 °C 1.2M H_2O (stock=28 mM)	Decomposed $Fe(acac)_3$ (mM)
5 minutes	1.60	7.7	1.45	9.9	1.35	11
10 minutes	1.54	8	1.41	10.4	1.19	13
15 minutes	1.51	8.5	1.35	11	1.18	13.5
20 minutes	1.50	9	1.28	12	1.15	13.75
25 minutes	1.49	9.4	1.24	12.5	1.06	14.5

Table 3.1.2.E Decomposition efficiency of $Fe(acac)_3$ at different time interval, addition carried out at 60 °C, 70 °C and 80 °C and at 1.2M ultrapure water concentration.

Sample	Decomposition Efficiency (%) 60 °C	Decomposition Efficiency (%) 70 °C	Decomposition Efficiency (%) 80 °C
1 (5 minutes from addition started)	28	35.35	39.28
2(after 10 minutes)	28.57	37.14	46.42
3(after 15 minutes)	30.35	39.28	48.21
4(after 20 minutes)	32.14	42.85	49.10
5(after 25 minutes)	33.57	44.64	51.78

In Table 3.1.2.D the absorbance, initial $Fe(acac)_3$ concentration and $Fe(acac)_3$(Initial-not reacted) concentration is shown. Decomposition efficiency in percentage was calculated by using $Fe(acac)_3$ (Initial - not reacted) concentration and initial concentration. Table 3.1.2.E represents the decomposition efficiency (%) at reducing acid solution addition temperature 60 °C, 70 °C and 80 °C.

Figure 3.1.2.F represents comparison of decomposition efficiency (%) at different addition

temperature. At 60 °C decomposition efficiency was 33.57% this indicates 1/3 reduction of $Fe(acac)_3$. Decomposition efficiency increased with respect to time shows that precursor gets reduced by ascorbic acid. It can be observed that there is increase in decomposition efficiency with respect to increase in addition temperature. This shows that rate of reaction increases with increase in addition temperature.

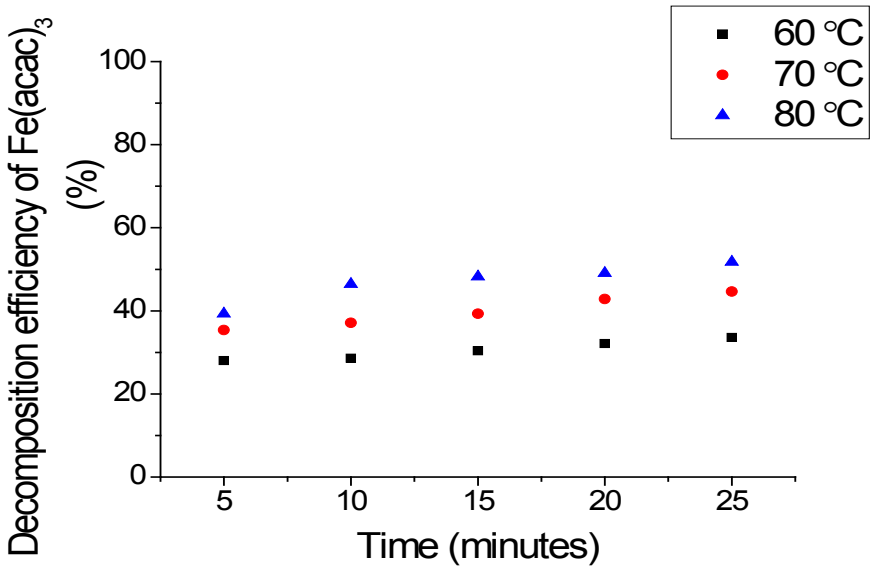

Figure 3.1.2.F Comparison of decomposition efficiency of $Fe(acac)_3$. [$Fe(acac)_3$] = 30 mmol/L (V = 50 mL), Reducing acid solution containing [ascorbic acid] = 25 mmol/L, [water] = 1.2 mol/L, Dropping rate: 2 mL/min, Volume of the reducing solution: 10 mL.

Table 3.1.2.G Final decomposition efficiency of $Fe(acac)_3$ when addition carried out at 60 °C, 70 °C and 80 °C and at 1.2 M ultrapure water concentration.

Addition temperature 1.2 M H_2O (stock=28 mM)	Absorbance (at λ_{max})	Decomposed $Fe(acac)_3$ (mM)	Final decomposition efficiency (%)
60 °C	0.15	26.05	93.03
70 °C	0.18	25.8	92.14
80 °C	0.19	25.65	91.60

Final decomposition efficiency estimated after the completion of reaction was estimated. Figure 3.1.2.F (a, b, c) represents UV-visible spectra measured after the completion of reaction. Table 3.1.2.G represents absorbance (at λ_{max}) and final decomposition efficiency estimated after the reaction completion. Results indicate that final decomposition efficiency was in the range of 90-100 %.

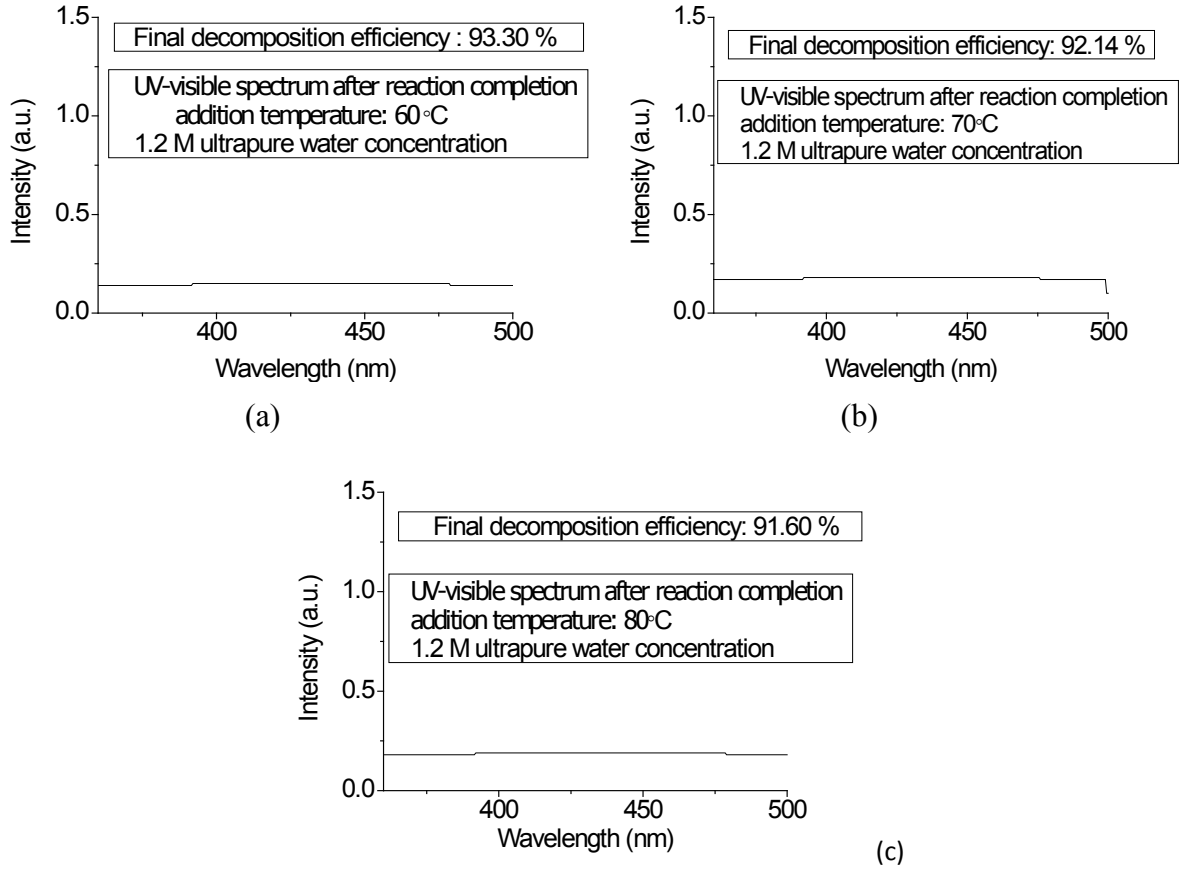

Figure 3.1.2.G Final decomposition efficiency of $Fe(acac)_3$ after reaction completion at different addition temperature at 60 °C (a), at 70 °C (b), at 80 °C (c). [$Fe(acac)_3$] = 30mmol/L (V = 50 mL), Reducing acid solution containing [ascorbic acid] = 25 mmol/L, [water] = 1.2 mol/L, Dropping rate: 2 mL/min, Volume of the reducing solution: 10 mL.

3.1.3 Influence of water concentration

Figure 3.1.3 (A, B, C) represents the UV-visible spectra at 2.4 M ultrapure water concentration and reducing acid (ascorbic acid) solution addition temperature of 60 °C, 70 °C and 80 °C respectively. It is observable that absorbance (at λ_{max}) decreases as the synthesis reaction proceeds which means that the precursor ($Fe(acac)_3$) gets decomposed and consumed in the reaction. It is observed that $Fe(acac)_3$ solution shows maximum absorption at 440 nm (λ_{max}). Change in ultrapure water concentration is not affecting on decomposition efficiency. There is negligible change in decomposition efficiency because the amount of $Fe(acac)_3$ reacted is almost same though ultrapure water concentration was changed.

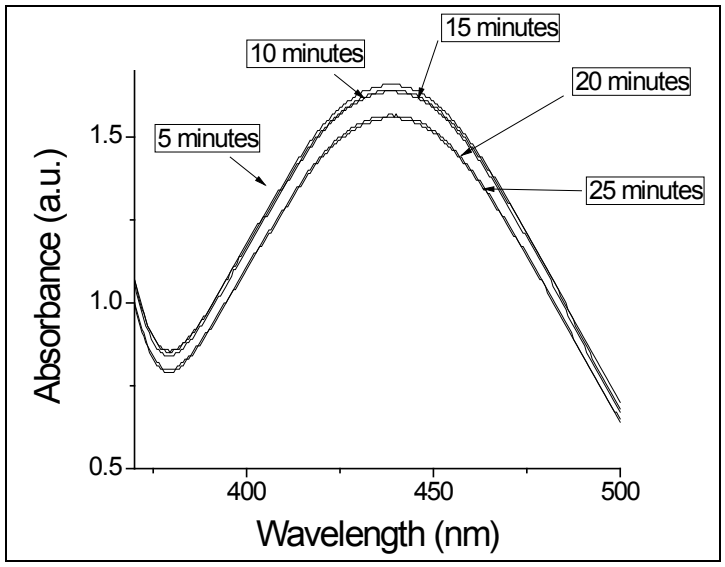

Figure 3.1.3.A UV-visible spectra of samples taken at different time interval and when addition carried out at 60 °C. [$Fe(acac)_3$] = 30mmol/L (V = 50 mL), Reducing acid solution containing [ascorbic acid] = 25 mmol/L, [water] = 2.4 mol/L, Dropping rate: 2 mL/min, Volume of the reducing solution: 10 mL.

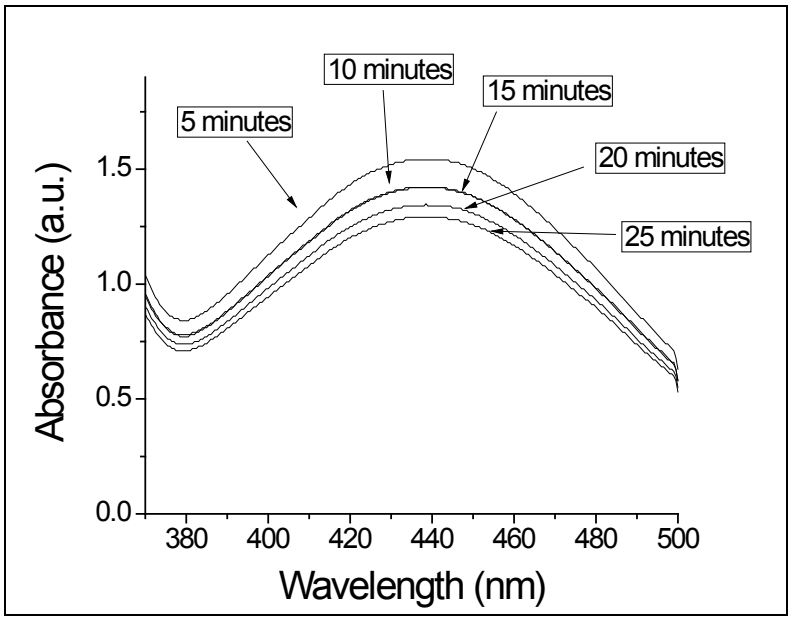

Figure 3.1.3.B UV-visible spectra of samples taken at different time interval and when addition carried out at 70 °C. [$Fe(acac)_3$] = 30mmol/L (V = 50 mL), Reducing acid solution containing [ascorbic acid] = 25 mmol/L, [water] = 2.4 mol/L, Dropping rate: 2 mL/min, Volume of the reducing solution: 10 mL.

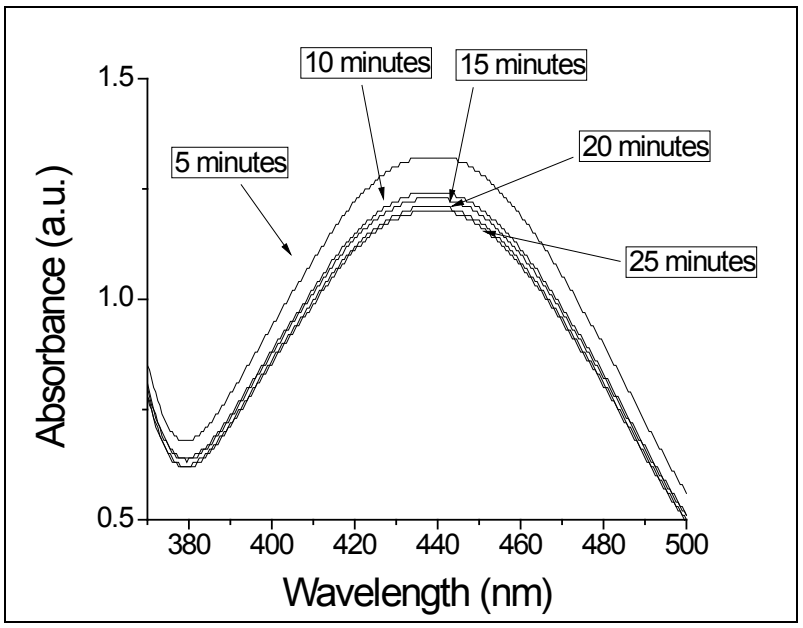

Figure 3.1.3.C UV-visible spectra of samples taken at different time interval and when addition carried out at 80 °C. [$Fe(acac)_3$] = 30mmol/L (V = 50 mL), Reducing acid solution containing [ascorbic acid] = 25 mmol/L, [water] = 2.4 mol/L, Dropping rate: 2 mL/min, Volume of the reducing solution: 10 mL.

Table 3.1.3.D Absorbance, $Fe(acac)_3$ Initial – $Fe(acac)_3$ not reacted concentration at different time and addition temperatures, at 2.4 M ultrapure water concentration.

Sample After addition	At 60 °C 2.4 M H_2O (stock= 29.5 mM)	Decomposed $Fe(acac)_3$ (mM)	At 70 °C 2.4 M H_2O (stock= 29 mM)	Decomposed $Fe(acac)_3$ (mM)	At 80 °C 2.4 M H_2O (stock= 30 mM)	Decomposed $Fe(acac)_3$ (mM)
5 minutes	1.66	8.5	1.54	9	1.32	13
10 minutes	1.64	8.8	1.42	11.2	1.24	14.5
15 minutes	1.64	8.8	1.42	11.2	1.23	14.62
20 minutes	1.56	10	1.34	12	1.21	14.88
25 minutes	1.56	10	1.30	13	1.20	15

In Table 3.1.3.D, the absorbance, initial $Fe(acac)_3$ concentration and $Fe(acac)_3$(Initial-not reacted) is shown. Decomposition efficiency in percentage was calculated by using $Fe(acac)_3$(Initial-not reacted) concentration and initial concentration. Table 3.1.3.E represents

the decomposition efficiency (%) when ultrapure water concentration was increased to 2.4 M and at reducing acid solution addition temperature 60 °C, 70 °C and 80 °C.

Table 3.1.3.E Decomposition efficiency of $Fe(acac)_3$ at different time interval and when addition carried out at 60 °C,70 °C and 80 °C, at 2.4 M ultrapure water concentration.

Sample	Decomposition Efficiency (%) 60 °C	Decomposition Efficiency (%) 70 °C	Decomposition Efficiency (%) 80 °C
1 (5 minutes from addition started)	28.81	31.03	43.33
2(after 10minutes)	29.83	38.62	48.33
3(after 15minutes)	30.51	38.62	48.73
4(after 20minutes)	33.9	41.37	49.6
5(after 25minutes)	33.9	44.82	50

Table 3.1.3.F Final decomposition efficiency of $Fe(acac)_3$ when addition carried out at 60°C, 70°C and 80°C and at 2.4 M ultrapure water concentration.

Addition temperature 2.4 M H_2O	Absorbance	Decomposed $Fe(acac)_3$ (mM)	Final decomposition efficiency (%)
60 °C (stock=29.5 mM)	0.20	27	91.52
70 °C (stock=29 mM)	0.22	26.47	91.27
80 °C (stock=30 mM)	0.21	27.46	91.53

It was observed that when ultrapure water concentration was changed to 2.4 M, there is no significant change in decomposition efficiency. This shows that change in ultrapure water concentration to 2.4 M does not have effect on rate of reaction or does not affect on rate of reaction.

Final decomposition efficiency estimated after the completion of reaction was estimated. Figure 3.1.3.G (a, b, c), represents UV-visible spectra measured after the completion of reaction. Table 3.1.3.F represents absorbance (at λ_{max}) and final decomposition efficiency estimated after the reaction completion. It was observed that final decomposition efficiency was in the range of 90-100 %.

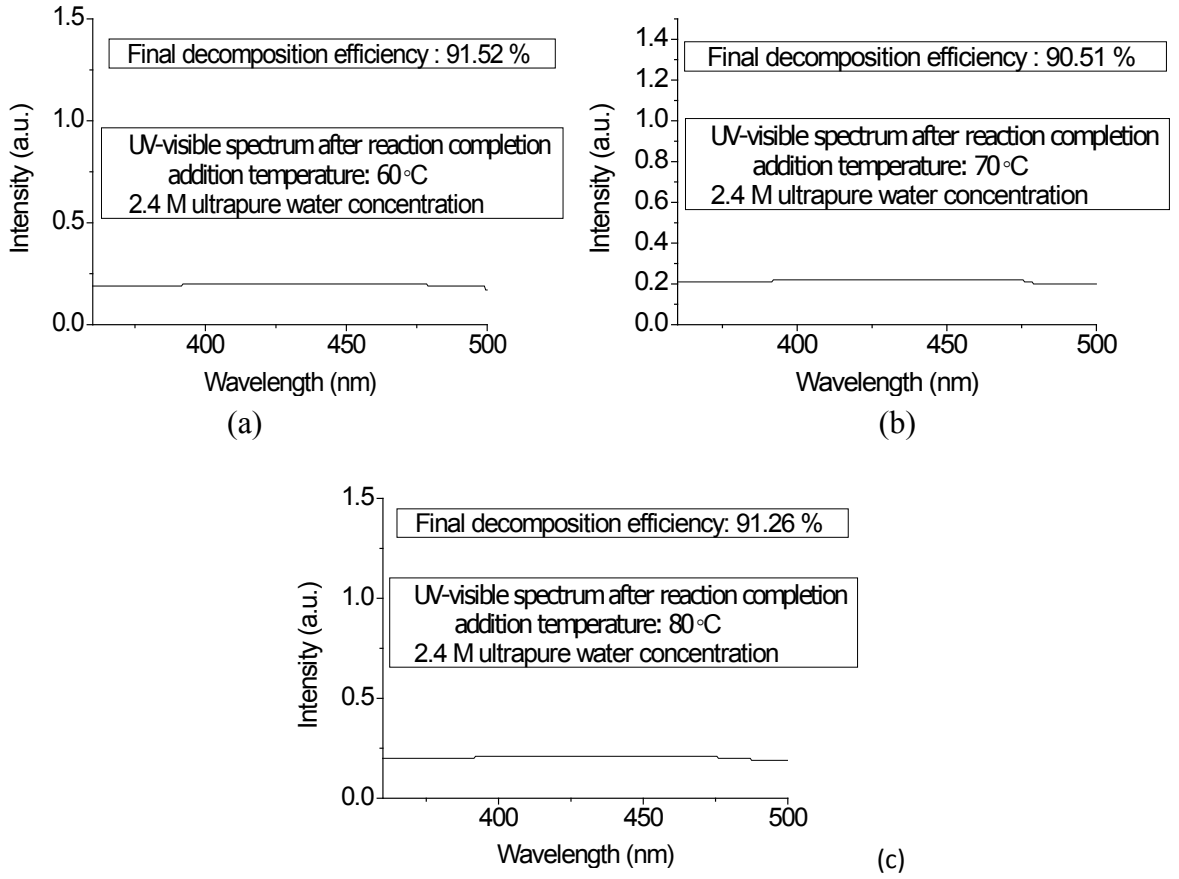

Figure 3.1.3.G Final decomposition efficiency of $Fe(acac)_3$ after reaction completion at different addition temperature at 60 °C (a), at 70 °C (b), at 80 °C (c). [$Fe(acac)_3$] = 30 mmol/L (V = 50 mL), Reducing acid solution containing [ascorbic acid] = 25 mmol/L, [water] = 2.4 mol/L, Dropping rate: 2 mL/min, Volume of the reducing solution: 10 mL.

Figures 3.1.3 (H, I, J) are the UV-visible spectra at 12 M ultrapure water concentration reducing acid (ascorbic acid) solution addition temperature of 60 °C, 70 °C and 80 °C. It is observable that absorbance (at λ_{max}) decreases as the synthesis reaction proceeds which means that the precursor ($Fe(acac)_3$) gets decomposed and consumed in the reaction. It is observed that $Fe(acac)_3$ solution shows maximum absorption at 440 nm (λ_{max}). Change in ultrapure water concentration is not affecting on decomposition efficiency. There is negligible change in decomposition efficiency because the amount of $Fe(acac)_3$ reacted is almost same though ultrapure water concentration was changed.

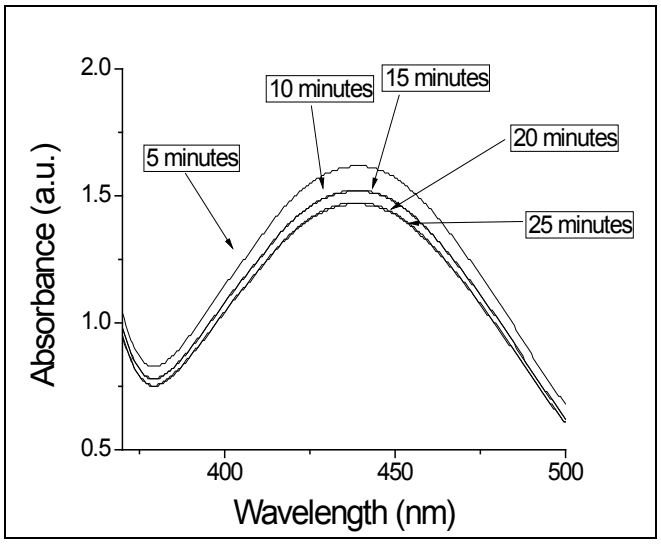

Figure 3.1.3.H UV-visible spectra of samples taken at different time interval and when addition carried out at 60 °C. [$Fe(acac)_3$] = 30mmol/L (V = 50 mL), Reducing acid solution containing [ascorbic acid] = 25 mmol/L, [water] = 12 mol/L, Dropping rate: 2 mL/min, Volume of the reducing solution: 10 mL.

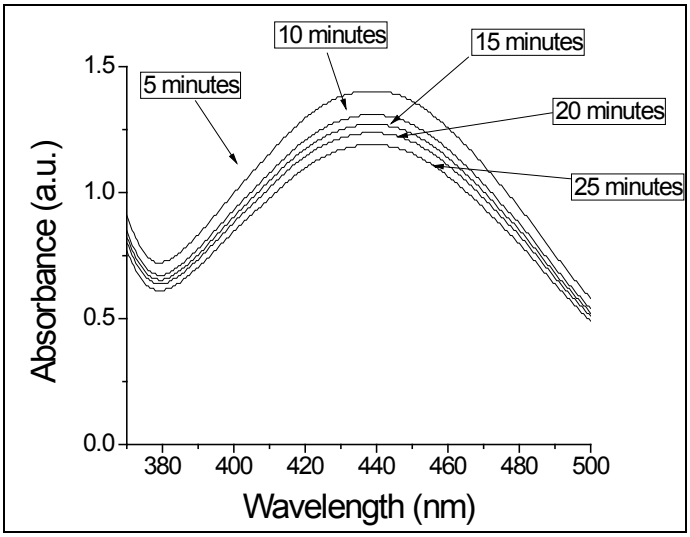

Figure 3.1.3.I UV-visible spectra of samples taken at different time interval and when addition carried out at 70 °C. [$Fe(acac)_3$] = 30 mmol/L (V = 50 mL), Reducing acid solution containing [ascorbic acid] = 25 mmol/L, [water] = 12 mol/L, Dropping rate: 2 mL/min, Volume of the reducing solution: 10 mL.

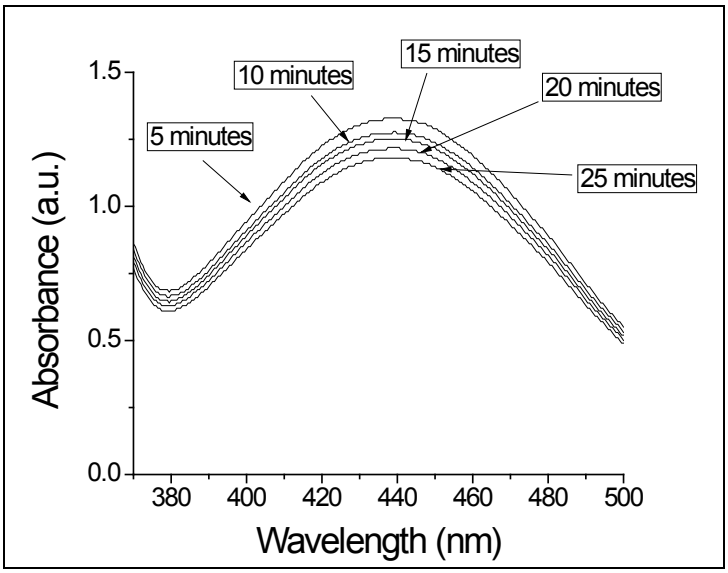

Figure 3.1.3.J UV-visible spectra of samples taken at different time interval and when addition carried out at 80 °C. [$Fe(acac)_3$] = 30mmol/L (V = 50 mL), Reducing acid solution containing [ascorbic acid] = 25 mmol/L, [water] = 12 mol/L, Dropping rate: 2 mL/min, Volume of the reducing solution: 10 mL.

Table 3.1.3.K Absorbance, $Fe(acac)_3$ Initial – $Fe(acac)_3$ not reacted concentration at different time interval and addition temperatures and at 12M ultrapure water concentration.

Sample After addition	At 60 °C 12M H_2O (stock=28 mM)	Decomposed $Fe(acac)_3$ (mM)	At 70 °C 12M H_2O (stock=26 mM)	Decomposed $Fe(acac)_3$ (mM)	At 80 °C 12M H_2O (stock=30 mM)	Decomposed $Fe(acac)_3$ (mM)
5 minutes	1.62	7.5	1.40	8.5	1.33	13.25
10 minutes	1.52	8.8	1.31	9.62	1.27	14
15 minutes	1.52	8.8	1.27	10.12	1.25	14.5
20 minutes	1.47	9.4	1.24	10.5	1.22	14.75
25 minutes	1.47	9.4	1.20	11	1.21	14.9

In Table 3.1.3.K the absorbance, initial $Fe(acac)_3$ concentrations and $Fe(acac)_3$(Initial-not reacted) is shown. Decomposition efficiency in percentage was calculated by using $Fe(acac)_3$(Initial-not reacted) concentration and initial concentration. Table 3.1.3.L represents the decomposition efficiency (%) when ultrapure water concentration was increased to 12 M and at reducing acid solution addition temperature 60 °C, 70 °C and 80 °C.

Table 3.1.3.L Decomposition efficiency of $Fe(acac)_3$ at different time interval and when addition carried out at 60 °C,70 °C and 80 °C and at 12 M ultrapure water concentration.

Sample	Decomposition Efficiency (%) 60 °C	Decomposition Efficiency (%) 70 °C	Decomposition Efficiency (%) 80 °C
1 (5 minutes from addition started)	26.78	32.69	44.16
2(after 10 minutes)	31.42	37	46.66
3(after 15 minutes)	31.42	38.92	48.33
4(after 20 minutes)	33.57	40.38	49.16
5(after 25 minutes)	33.57	42.30	49.66

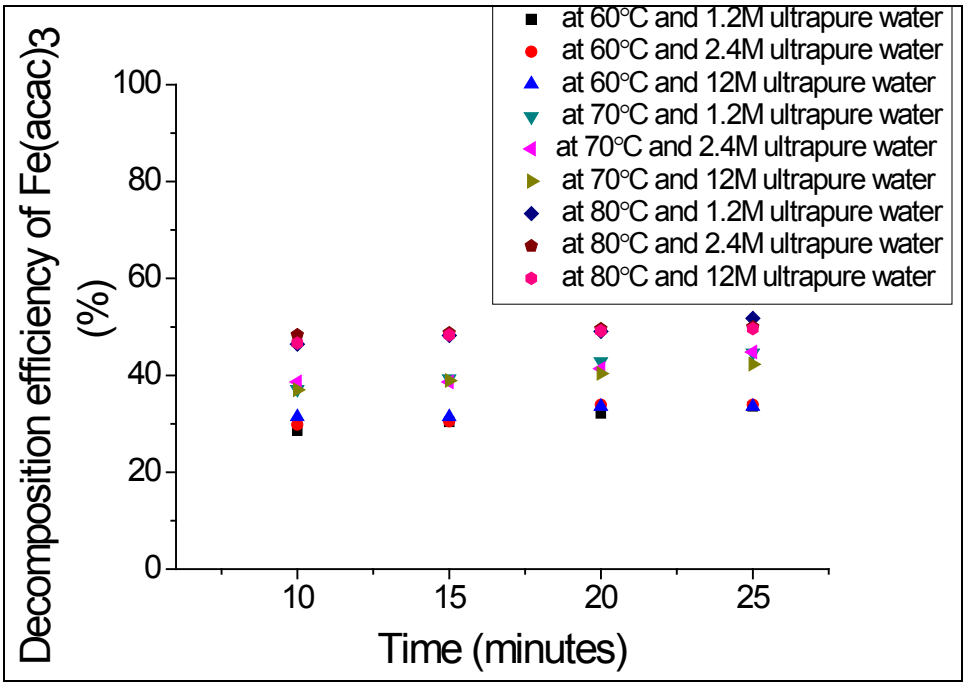

Figure 3.1.3.M Comparison between decomposition efficiency of $Fe(acac)_3$ (%) at different addition temperature and at different ultrapure water concentration.

It was observed that there is no significant effect on decomposition efficiency at 12M ultrapure water concentration. Figure 3.1.3.M represents comparison between decomposition efficiency (%) at different addition temperature 60 °C, 70 °C and 80 °C and at different ultrapure water concentration. Results shows that ultrapure water has no significant effect on decomposition efficiency, hence ultrapure water have no significant effect on rate of reaction.

Final decomposition efficiency estimated after the completion of reaction was estimated. Figure 3.1.3.N represents UV-visible spectra measured after the completion of reaction. Table 3.1.3.O represents absorbance (at λ_{max}) and final decomposition efficiency estimated after the reaction completion. Results indicate that final decomposition efficiency was in the range of

90-100 %.

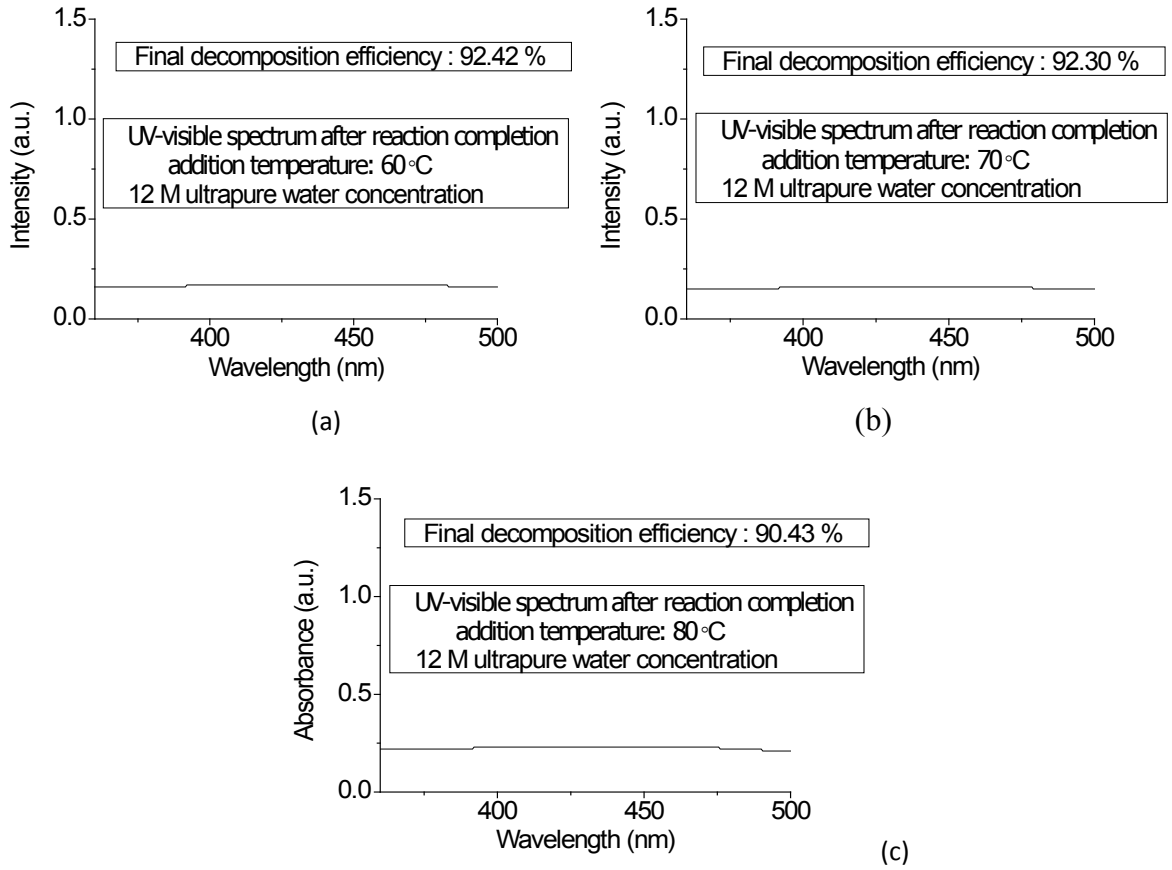

Figure 3.1.3.N Final decomposition efficiency of $Fe(acac)_3$ after reaction completion at different addition temperature at 60 °C (a), at 70 °C (b), at 80 °C (c). [$Fe(aca)_3$] = 30mmol/L (V = 50 mL), Reducing acid solution containing [ascorbic acid] = 25 mmol/L, [water] = 12 mol/L, Dropping rate: 2 mL/min, Volume of the reducing solution: 10 mL.

Table 3.1.3.O Final decomposition efficiency of $Fe(acac)_3$ when addition carried out at 60 °C, 70 °C and 80 °C and at 12M ultrapure water concentration.

Addition temperature 2.4 M H_2O	Absorbance	Decomposed $Fe(acac)_3$ (mM)	Final decomposition efficiency (%)
60 °C (stock=28 mM)	0.17	25.85	92.32
70 °C (stock=26 mM)	0.16	24	92.30
80 °C (stock=30 mM)	0.23	27.2	90.66

3.2 The influence of synthesis parameters on the composition and particle size of Fe_3O_4 nanoparticles

3.2.1 Influence of addition temperature

Figure 3.2.1.A represents the XRD patterns of sample prepared when addition was done at room temperature (Sample a), addition done at 60 °C (Sample b). In sample a, two peaks were observed at 2θ = 31.6, 45.3. These peaks are due to (220), (331) crystal planes of Fe_3O_4. XRD pattern of sample b shows two weak and broad peaks at 2θ= 35.44, 62.23. These peaks are due to (311) and (440) crystals planes of Fe_3O_4.

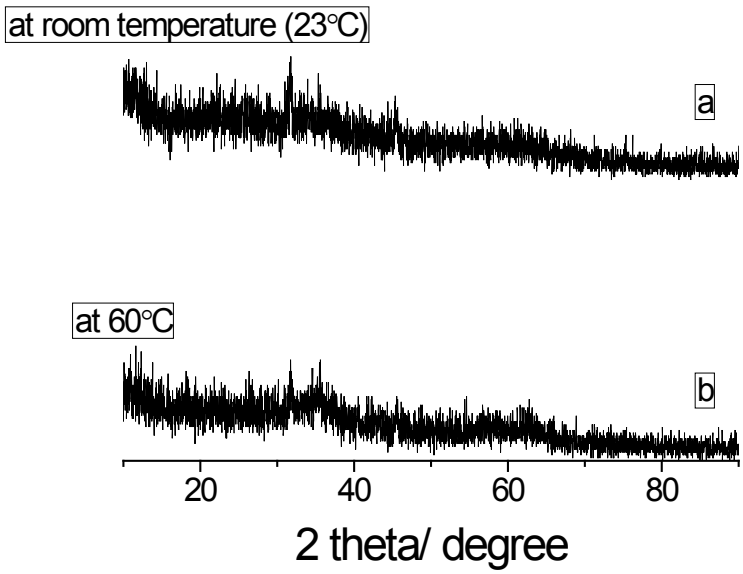

Figure 3.2.1.A XRD pattern of sample prepared when addition done at room temperature (Sample A), addition done at 60°C (Sample B). [$Fe(acac)_3$] = 30 mmol/L (V = 50 mL), Reducing acid solution containing [ascorbic acid] = 25 mmol/L, [water] = 1.2 mol/L, Dropping rate: 2 mL/min, Volume of the reducing solution: 10 mL.

Figure 3.2.1.B and Figure 3.2.1.C are the EDAX spectra of samples (sample A and sample B) prepared when addition was carried out at room temperature and at 60 °C at 1.2 M ultrapure water concentration. EDAX spectra (Figure 3.4.B and Figure 3.4.C) confirms the presence of Fe and O. Amount of carbon was detected because samples were mounted on carbon tape.

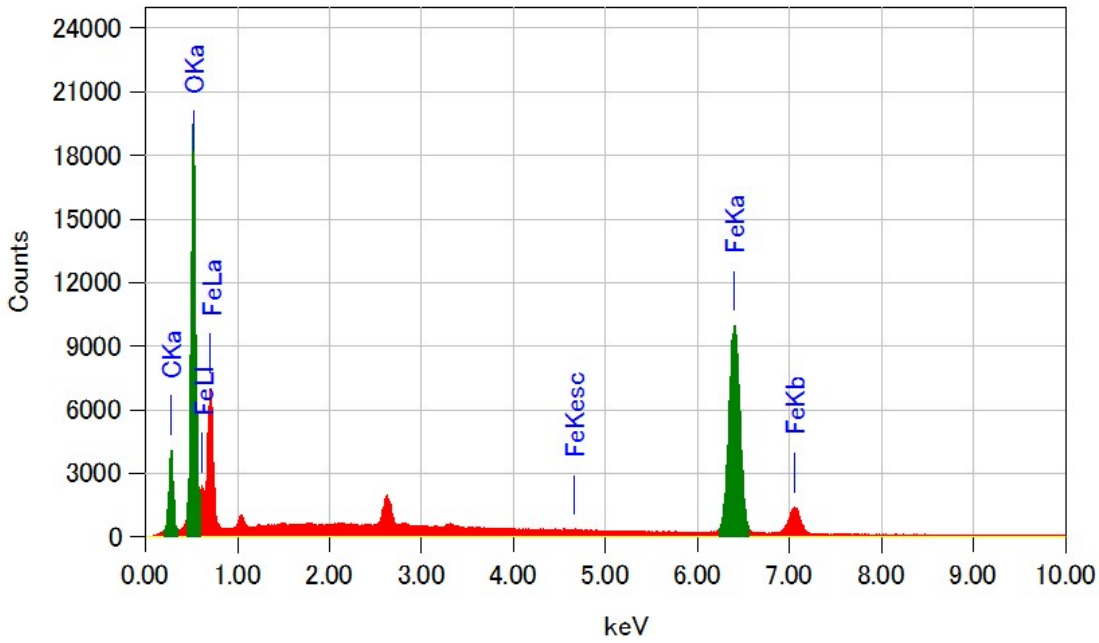

Figure 3.2.1.B EDAX pattern of sample prepared when addition done at room temperature (23°C), (Sample A). [$Fe(acac)_3$] = 30mmol/L (V = 50 mL), Reducing acid solution containing [ascorbic acid] = 25 mmol/L, [water] = 1.2 mol/L, Dropping rate: 2 mL/min, Volume of the reducing solution: 10 mL.

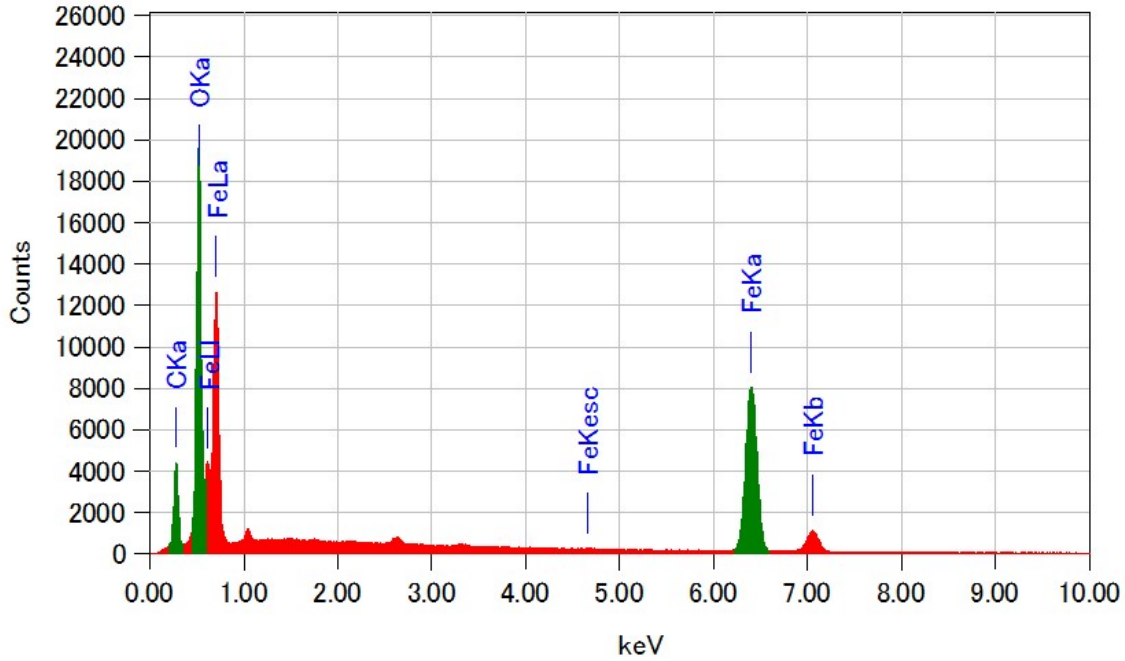

Figure 3.2.1.C EDAX pattern of sample prepared when addition done at 60°C (sample B). [$Fe(acac)_3$] = 30mmol/L (V = 50 mL), Reducing acid solution containing [ascorbic acid] = 25 mmol/L, [water] = 1.2 mol/L, Dropping rate: 2 mL/min, Volume of the reducing solution: 10 mL.

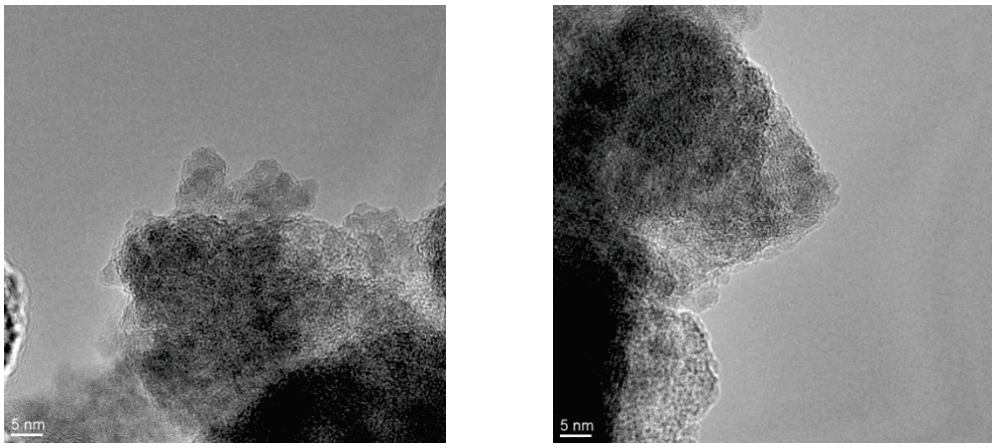

(a) (b)

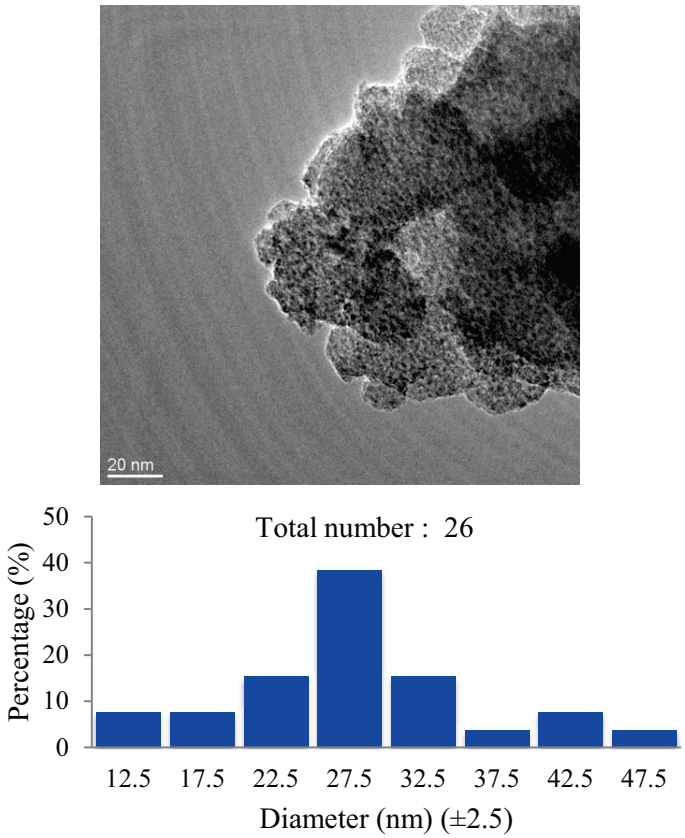

(c)

Figure 3.2.1.D HRTEM images of samples synthesized at 1.2M ultrapure water, addition at room temperature (a, b), at addition temperature of 60 °C with particle diameter distribution histogram (c). [$Fe(acac)_3$] = 30 mmol/L (V = 50 mL), Reducing acid solution containing [ascorbic acid] = 25 mmol/L, [water] = 1.2 mol/L, Dropping rate: 2 mL/min, Volume of the reducing solution: 10 mL.

Figure 3.2.1.D represents HRTEM (High Resolution Transmission Electron Microscopy)

images of Fe_3O_4 nanoparticles prepared at conditions same as in Figure 3.2.1.A. In Figure 3.2.1.D.a and b, the HRTEM images of sample prepared at 1.2 M ultrapure water concentration and when addition was carried out at room temperature are presented. Images were taken at different places on sample grid. Results show that this sample is largely aggregated. Figure 3.2.1.D.c shows HRTEM image and particle diameter distribution histogram of Fe_3O_4 nanoparticles prepared when addition was carried out at 60 °C and at 1.2 M ultrapure water. It was observed that the mean particle diameter of Fe_3O_4 nanoparticles was 29 ±9 nm at addition temperature of 60 °C.

Figure 3.2.1.E (a and b) are XRD patterns of particles synthesized with 1.2 M water at 70 °C and 80 °C respectively. In Fig. 3.2.1.E. (a), three week and broad diffraction peaks were observed at 2θ = 31.5, 35.4, 45.6 corresponded to (220), (311) and (331) crystal plane of Fe_3O_4 and the mean particle diameter was estimated at 33±3 nm. In 3.2.1.E (b), six weak and broad diffraction peaks were observed at 2θ = 31.5, 35.3, 42.9, 45.4, 56.9 and 62.3 corresponded to (220), (311), (400), (331), (511), (440) crystal planes of Fe_3O_4 and the mean particle diameter was 42±5 nm. These results imply that Fe_3O_4 nanoparticles can be synthesized by ascorbic acid mediated reduction of $Fe(acac)_3$.

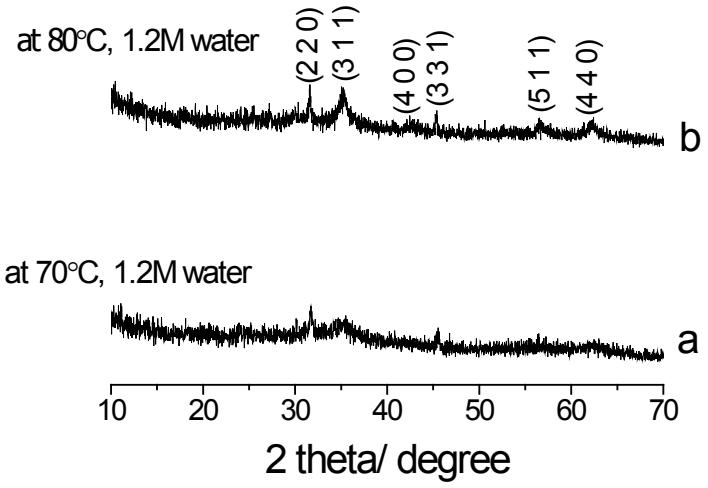

Figure 3.2.1.E XRD pattern of sample prepared when addition done at 70 °C (Sample a), addition done at 80 °C (Sample b). [$Fe(acac)_3$] = 30mmol/L (V = 50 mL), Reducing acid solution containing [ascorbic acid] = 25 mmol/L, [water] = 1.2 mol/L, Dropping rate: 2 mL/min, Volume of the reducing solution: 10 mL.

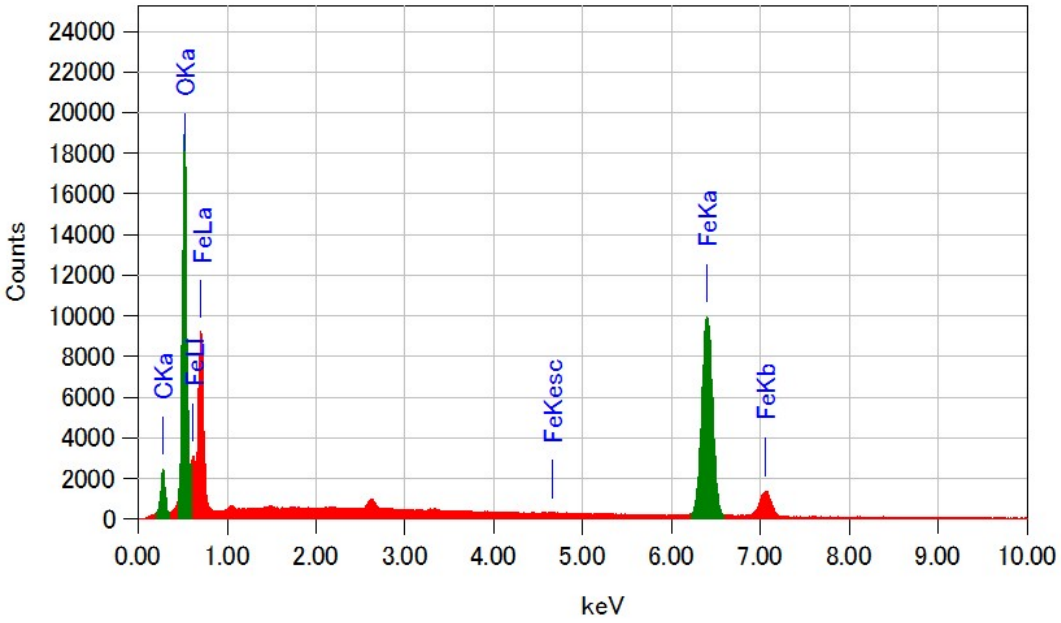

Figure 3.2.1.F EDAX spectrum of sample prepared when addition done at 70 °C (sample a). [Fe(acac)$_3$] = 30mmol/L (V = 50 mL), Reducing acid solution containing [ascorbic acid] = 25 mmol/L, [water] = 1.2 mol/L, Dropping rate: 2 mL/min, Volume of the reducing solution: 10 mL.

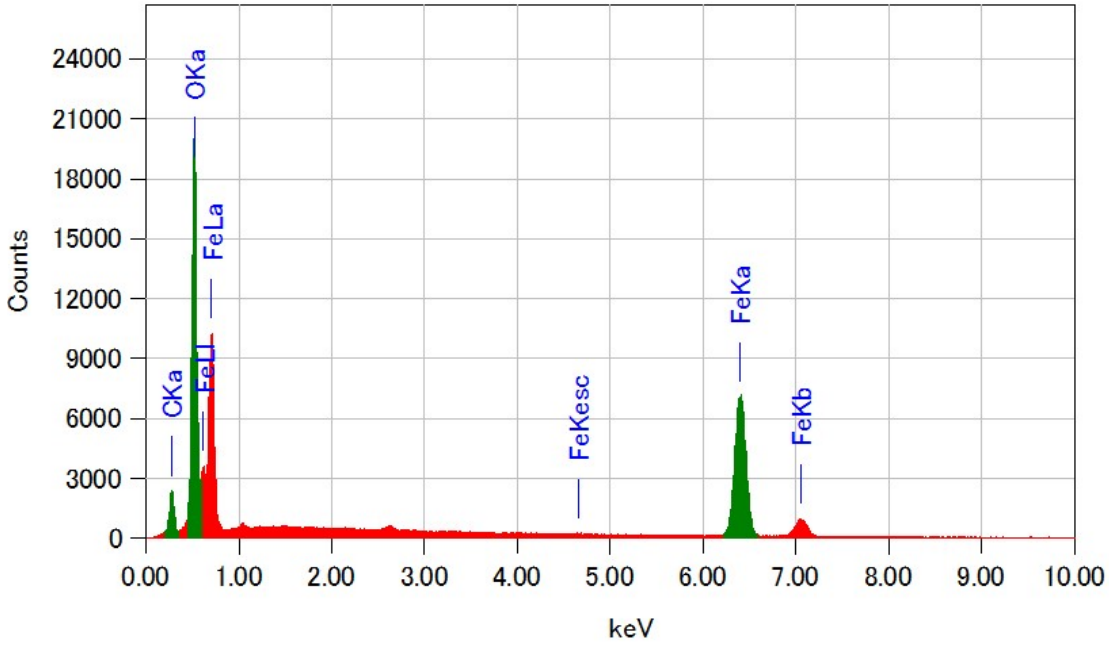

Figure 3.2.1.G EDAXspectrum of sample prepared when addition done at 80°C (sample b). [Fe(acac)$_3$] = 30mmol/L (V = 50 mL), Reducing acid solution containing [ascorbic acid] = 25 mmol/L, [water] = 1.2 mol/L, Dropping rate: 2 mL/min, Volume of the reducing solution: 10 mL.

Figure 3.2.1.F and Figure 3.2.1.G shows the EDAX spectra of samples prepared when addition was carried out at 70°C and 80°C respectively. Both EDAX spectra confirm the presence of

Iron (Fe) and Oxygen (O). Carbon (C) was detected because samples were mounted on carbon tape.

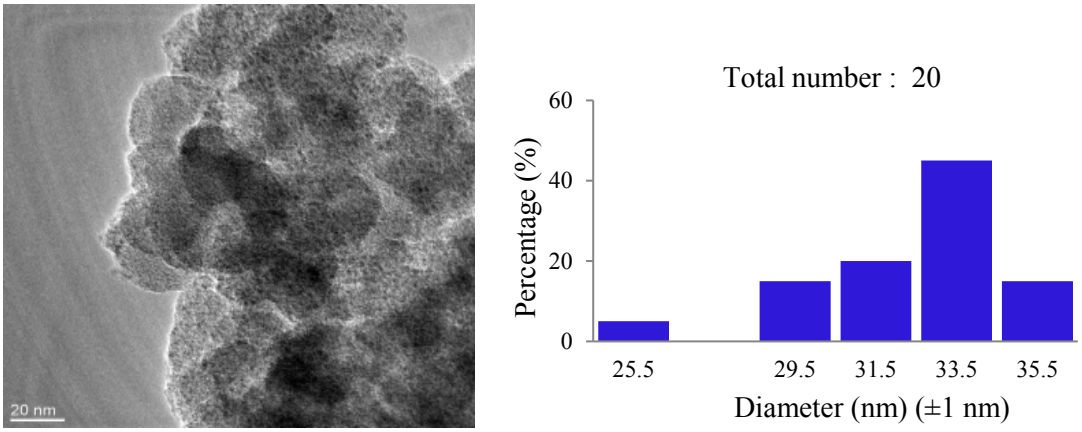

(a)

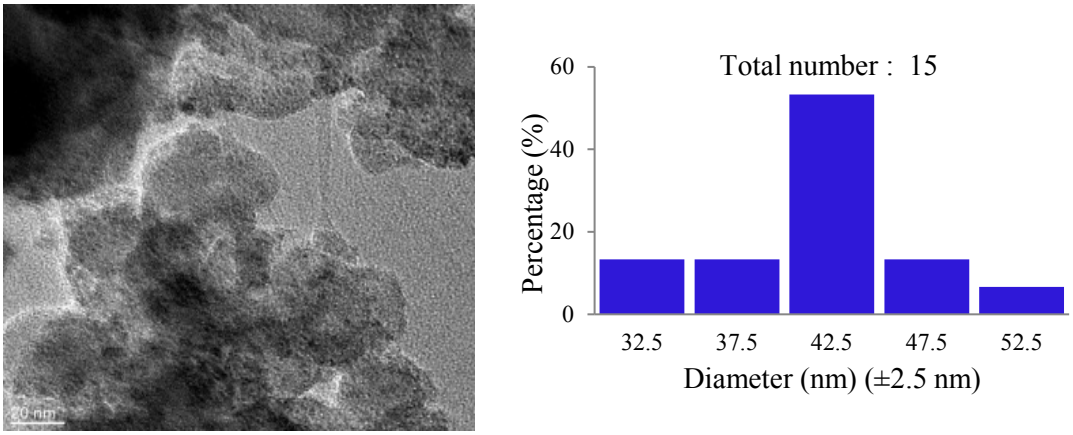

(b)

Figure 3.2.1.H HRTEM images and particle diameter distribution histogram of nanoparticles prepared at 1.2 M ultrapure water concentration: TEM (a) image of nanoparticles at addition temperature 70 °C and TEM (b) image of sample at addition temperature 80 °C. [$Fe(acac)_3$] = 30mmol/L (V = 50 mL), Reducing acid solution containing [ascorbic acid] = 25 mmol/L, [water] = 1.2 mol/L, Dropping rate: 2 mL/min, Volume of the reducing solution: 10 mL.

Figure 3.2.1.H represents HRTEM images and particle diameter distribution histogram of samples prepared when addition was carried out at 70°C and 80°C at 1.2M ultrapure water concentration. From the results in Fig. 3.2.1.H, it was observed that at 1.2M ultrapure water concentration mean particle diameter of Fe_3O_4 nanoparticles was 33±3 nm (a) and 42±5 nm (b) at addition temperature 70°C and 80°C respectively. At 1.2 M ultrapure water concentration Fe_3O_4 nanoparticle size increases with increase in addition temperature. This might be due to

when addition temperature increases at 1.2 M ultrapure water concentration due less number of nucleation sites or number of nuclei Fe_3O_4 nanoparticle size is increasing.

3.2.2 Influence of water concentration

Figure 3.2.2.A represents XRD patterns of samples prepared at addition temperature 60° C (a) and at 80° C (b) having average particle diameter 23 nm and 7 nm respectively. The average particle diameter of Fe_3O_4 nanoparticles was estimated with full-width at half maximum (FWHM) of an X-ray diffraction peak and Scherrer equation. In Figure 3.2.2A.a, eight diffraction peaks observed at 2θ= 18.02, 30.06, 35.48, 36.9, 43.12, 53.46, 56.94, 62.56. These peaks are due to (111), (220), (311), (222), (400), (422), (511) and (440) crystal planes of Fe_3O_4 phase. In Figure 3.2.2.A.b eight diffraction peaks observed at 2θ =18.3, 30.04, 35.4, 37.1, 43.0, 53.3, 56.9, 62.5. These peaks are due to (111), (220), (311), (222), (400), (422), (511) and (440) crystal planes of Fe_3O_4. The data is in accordance with reported data.

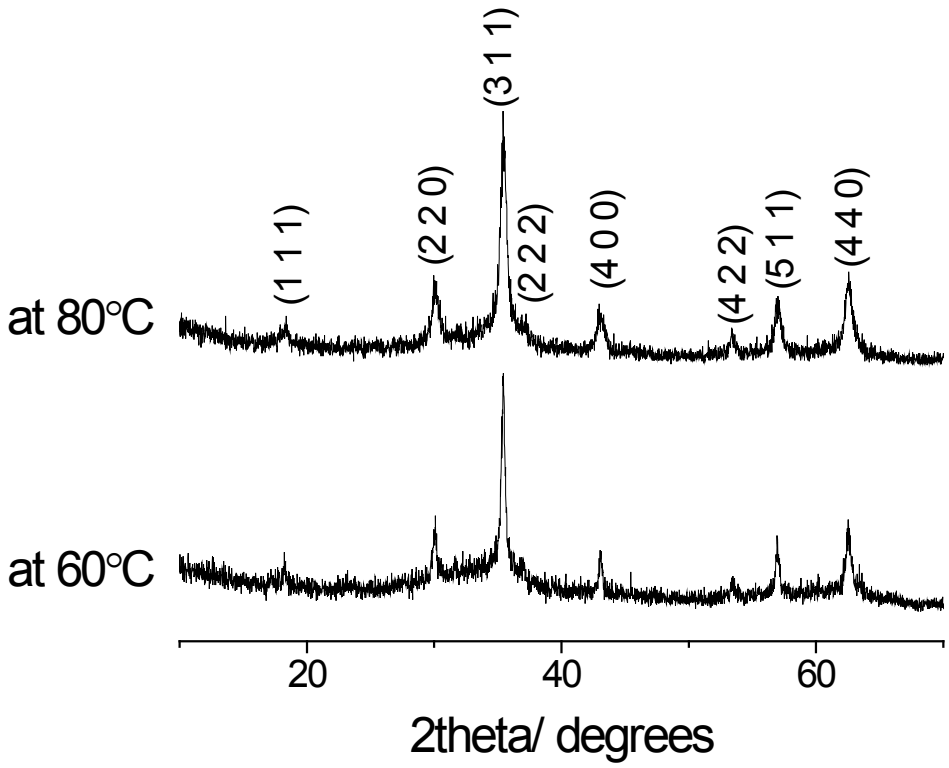

Figure 3.2.2.A XRD pattern of sample prepared when addition done at 60 °C (a), addition done at 80 °C(b). [$Fe(acac)_3$] = 30mmol/L (V = 50 mL), Reducing acid solution containing [ascorbic acid] = 25 mmol/L, [water] = 12 mol/L, Dropping rate: 2 mL/min, Volume of the reducing solution: 10 mL.

Figure 3.2.2.B and Figure 3.2.2.C represents EDAX spectra of sample prepared at addition temperature 60 °C (Figure 3.6.B) and 80 °C (Figure 3.6.C). Both EDAX spectra show the

presence of Iron (Fe) and Oxygen (O). Carbon (C) was detected because samples were mounted on carbon tape.

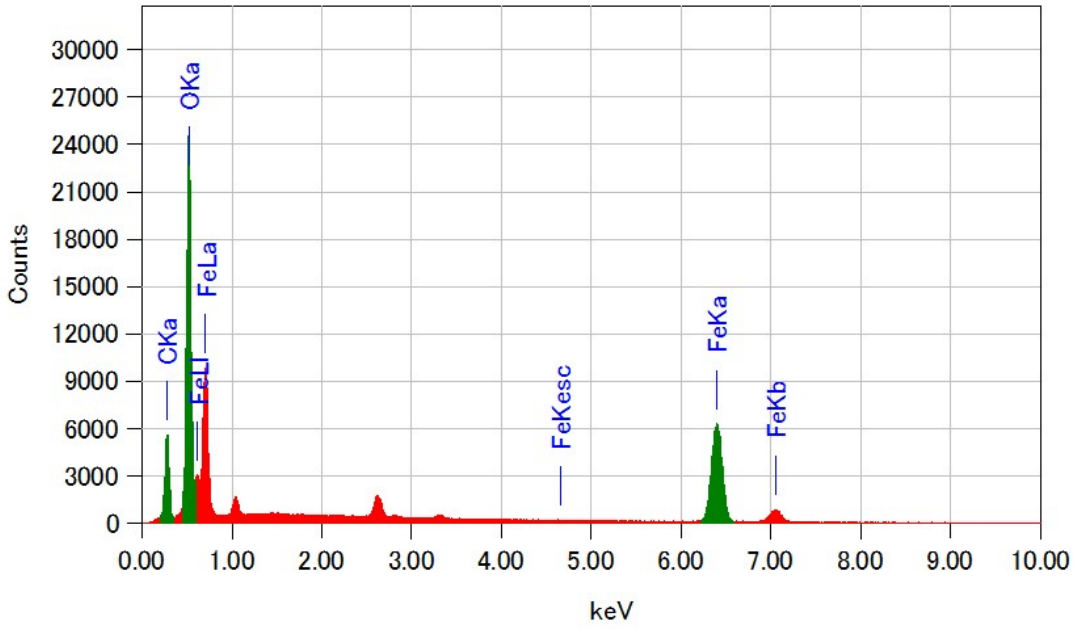

Figure 3.2.2.B EDAX spectrum of sample prepared when addition done at 60 °C. [Fe(acac)$_3$] = 30 mmol/L (V = 50 mL), Reducing acid solution containing [ascorbic acid] = 25 mmol/L, [water] = 12 mol/L, Dropping rate: 2 mL/min, Volume of the reducing solution: 10 mL.

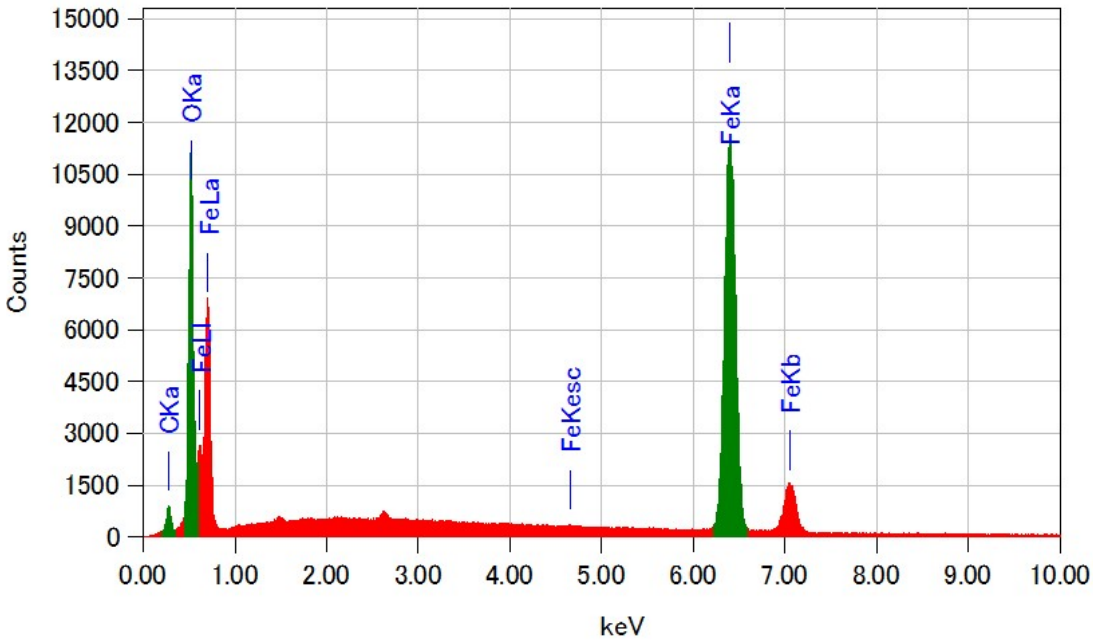

Figure 3.2.2.C EDAX spectrum of sample prepared when addition done at 80°C. [Fe(acac)$_3$] = 30mmol/L (V = 50 mL), Reducing acid solution containing [ascorbic acid] = 25 mmol/L, [water] = 12 mol/L, Dropping rate: 2 mL/min, Volume of the reducing solution: 10 mL.

Figure 3.2.2.D shows HRTEM images and particle diameter distribution histograms for nanoparticles prepared at addition temperature 60 °C (a) and 80 °C (b) and at 12M ultrapure water concentration. It was observed that when addition of reducing acid solution was carried out at 60 °C Fe_3O_4 nanoparticles with size 22±6 nm were synthesized while when addition was carried out at 80 °C size of nanoparticles was reduced to 8±2 nm.

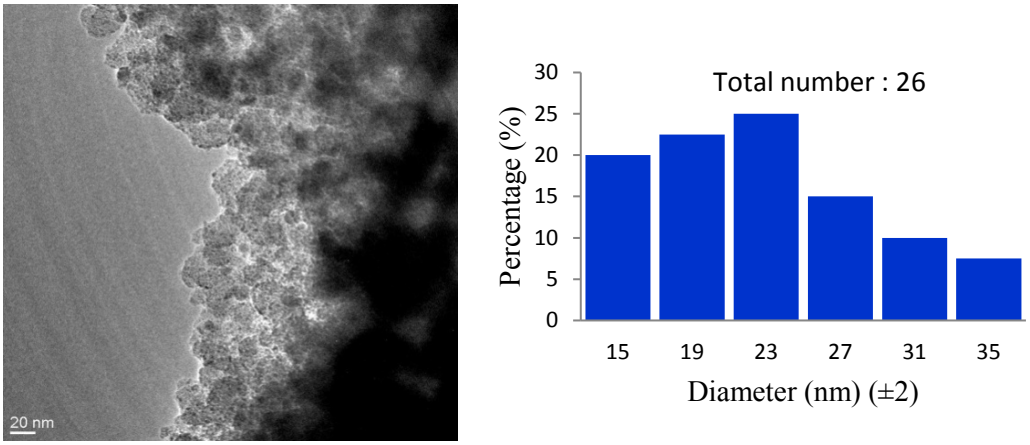

(a)

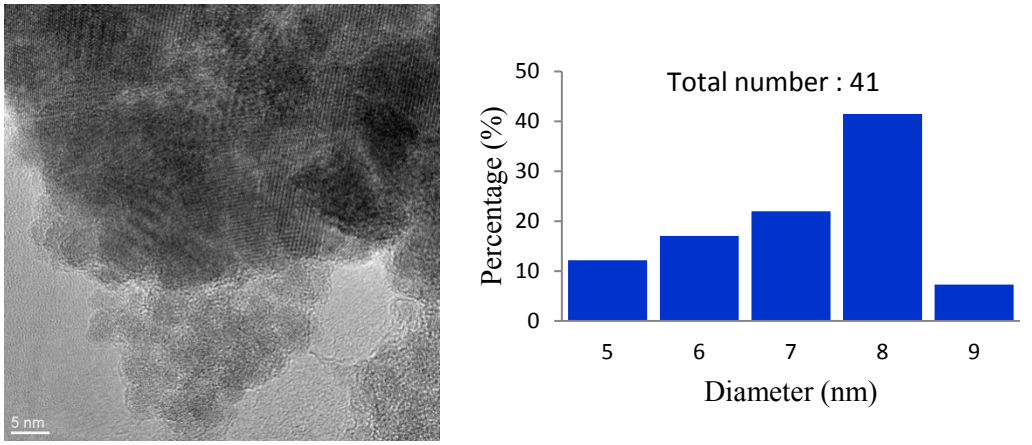

(b)

Figure 3.2.2.D HRTEM images and particle diameter distribution histogram of sample prepared when addition done at 60 °C (a), addition done at 80 °C (b). [$Fe(acac)_3$] = 30 mmol/L (V = 50 mL), Reducing acid solution containing [ascorbic acid] = 25 mmol/L, [water] = 12 mol/L, Dropping rate: 2 mL/min, Volume of the reducing solution: 10 mL.

These results agreed with XRD results (Fig.3.2.2.A). These results in comparison with Fe_3O_4 nanoparticles synthesized at 1.2 M ultrapure water concentration shows that the size of Fe_3O_4 nanoparticles decreases as ultrapure water concentration increases. This might be due to when ultrapure water concentration increases the number of nuclei or nucleation sites are increasing and Fe_3O_4 nanoparticle size decreases.

Fig. 3.2.2.E shows the XRD pattern of the powder sample formed by reduction of $Fe(acac)_3$. While preparing this sample, addition of ascorbic acid solution was carried out at 70 °C and then reaction mixture was refluxed for 1 hour. All the peaks in Figure (3.7.D) can be indexed as pure Fe_3O_4 phase with inverse spinel structure and matched well with the reported data (JCPDS: 65-3107). No impurities were detected. The crystallite size was calculated by Scherrer equation. Full-width-at-half-maximum (FWHM) of the strongest peak (3 1 1) was used for calculation. Crystallite size calculated was 15 nm.

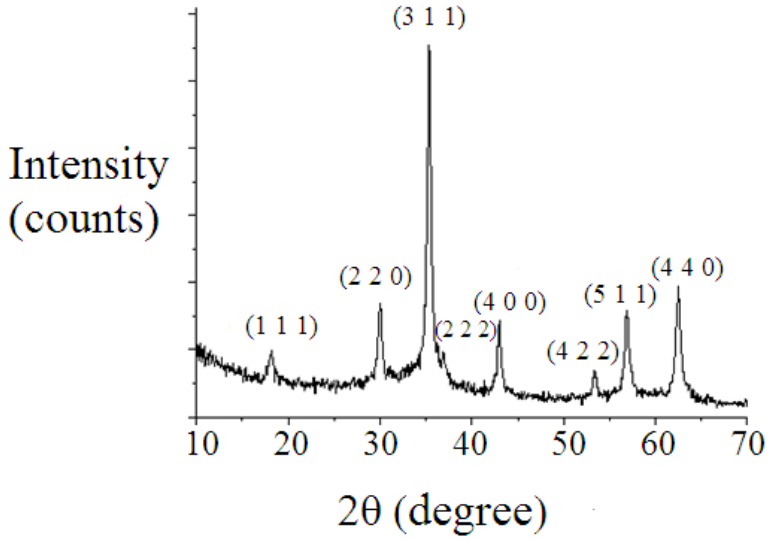

Figure 3.2.2.E X-ray diffraction pattern of sample prepared with addition of ascorbic acid at 70 °C and reflux for 1 hour. [$Fe(acac)_3$] = 30mmol/L (V = 50 mL), Reducing acid solution containing [ascorbic acid] = 25 mmol/L, [water] = 12 mol/L, Dropping rate: 2 mL/min, Volume of the reducing solution: 10 mL.

Figure 3.2.2.F presents the high resolution HRTEM images and particle diameter distribution histogram of the representative sample prepared with addition of ascorbic acid solution at 70 °C. The mean particle diameter is observed to be 15±4 nm. Fe_3O_4 nanoparticles with size less than 25 nm were successfully synthesized by fine tuning of the reaction parameters such as addition temperature, reflux temperature, dropping rate, and reflux time.

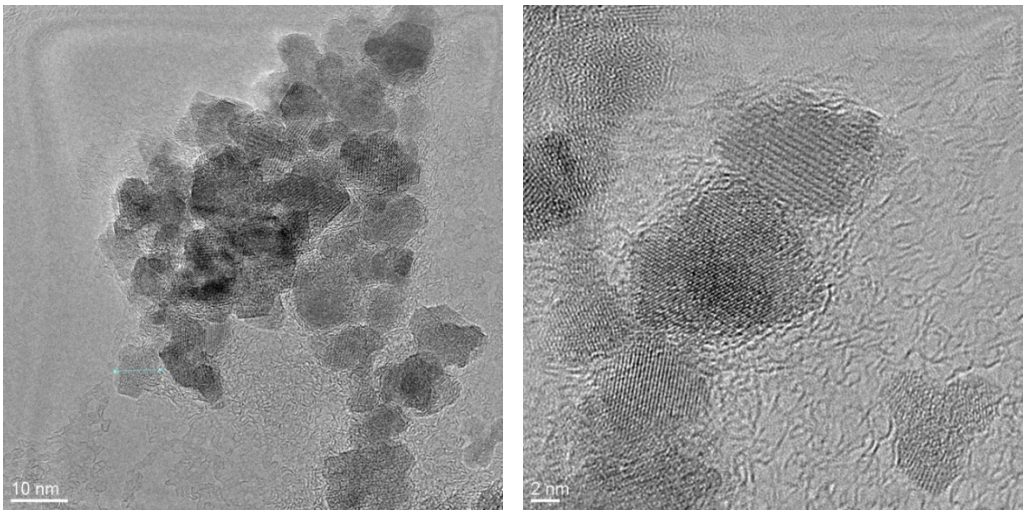

(a) (b)

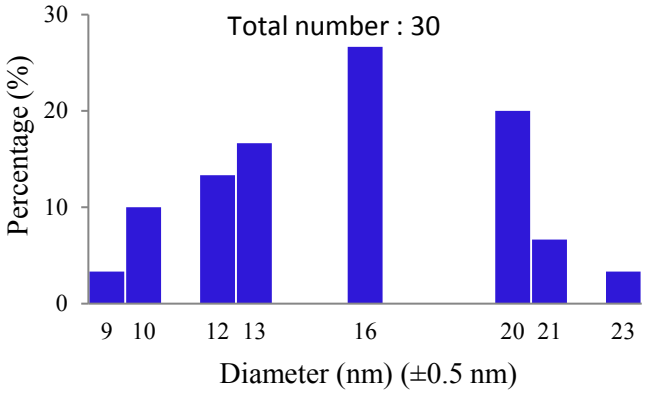

Figure 3.2.2.F HRTEM images (a, b) and particle diameter distribution histogram of Fe_3O_4 nanoparticles at addition temperature of 70 °C. [$Fe(acac)_3$] = 30 mmol/L (V = 50 mL), Reducing acid solution containing [ascorbic acid] = 25 mmol/L, [water] = 12 mol/L, Dropping rate: 2 mL/min, Volume of the reducing solution: 10 mL.

Figure 3.2.2.G shows the EDAX analysis of sample prepared when addition of ascorbic acid at 70 °C and reflux for 1 hour. The result confirms the presence of iron and oxygen. Carbon detected is due to carbon tape used for mounting the sample.

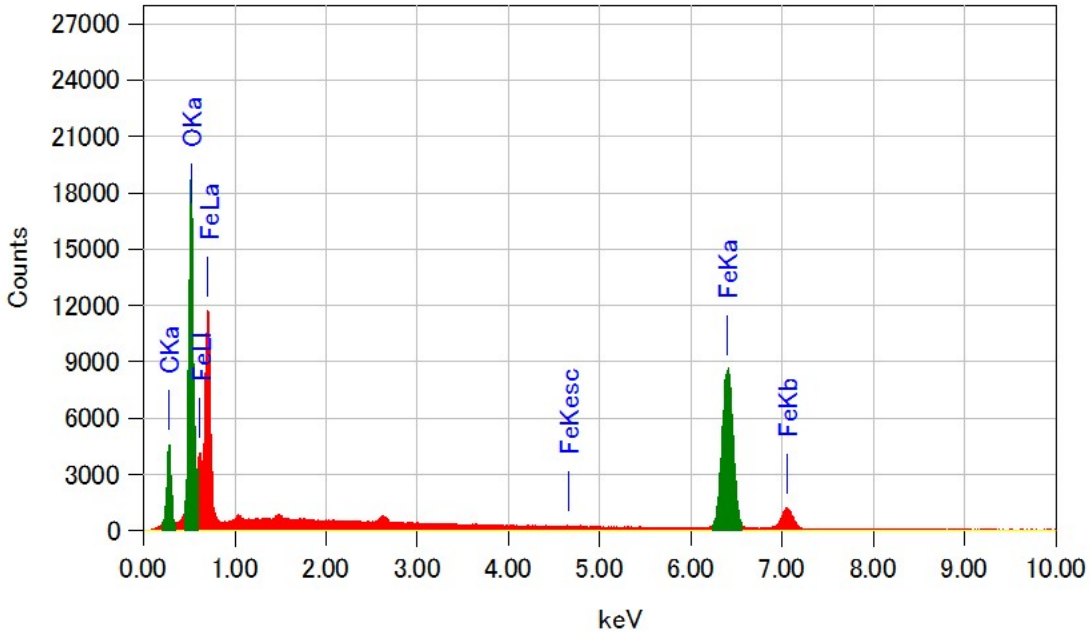

Figure 3.2.2.G EDAX analysis of Fe_3O_4 nanoparticles sample. [$Fe(acac)_3$] = 30 mmol/L (V = 50 mL), Reducing acid solution containing [ascorbic acid] = 25 mmol/L, addition temperature of 70 °C, [water] = 12 mol/L, Dropping rate: 2 mL/min, Volume of the reducing solution: 10 mL.

Figure 3.2.2.H represents survey spectrum or full scan wide spectrum of sample (a) and C1s spectrum of carbon (b) respectively. All obvious peaks in survey/full scan spectrum are labeled and can be ascribed to Fe, O, and C. The C1s peak was set to 284.8 eV to normalize any peak shifts. Figure 3.2.2.I shows the XPS spectrum of Fe 2p region. The Fe 2p spectrum can be deconvoluted into five peaks at 709.7 eV, 711.3 eV, 719.4 eV, 723.1 eV, and 724.6 eV. Photoelectron peak at binding energy of 724.6 eV corresponds to $2p_{1/2}$ of Fe^{3+} ion; the peak at binding energy of 723.1 eV can be assigned to $2p_{1/2}$ of Fe^{2+} [6]. The peaks at 709.7 eV and 711.3 eV can be assigned to $2p_{3/2}$ of Fe^{2+} and Fe^{3+} ions respectively [6]. The peak at 719.4 eV is a satellite peak for above four peaks.

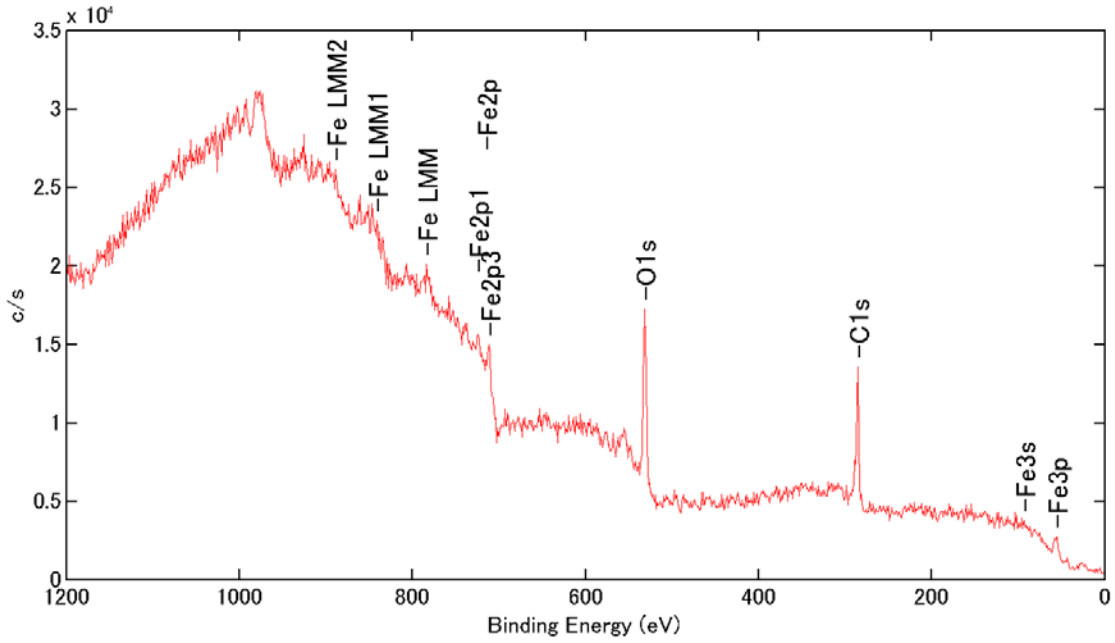

(a)

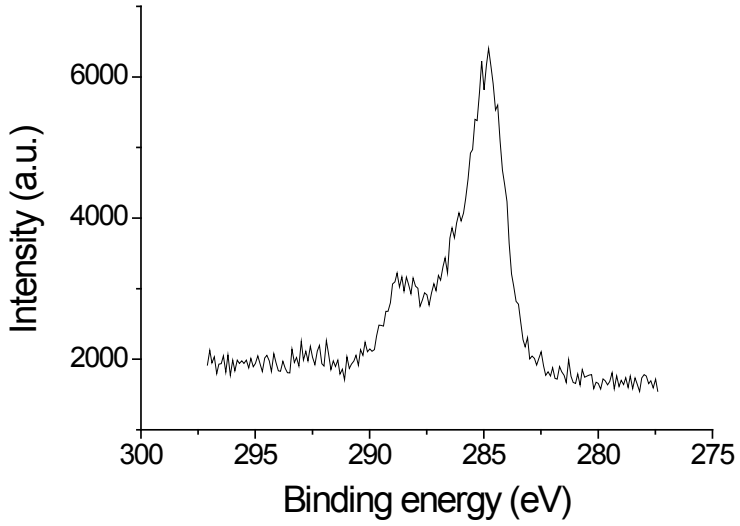

(b)

Figure 3.2.2.H Survey XPS scan (a), C1s spectrum of C (b), [Fe(acac)$_3$] = 30 mmol/L (V = 50 mL), addition temperature of 70 °C, Reducing acid solution containing [ascorbic acid] = 25 mmol/L, [water] = 12 mol/L, Dropping rate: 2 mL/min, Volume of the reducing solution: 10 mL.

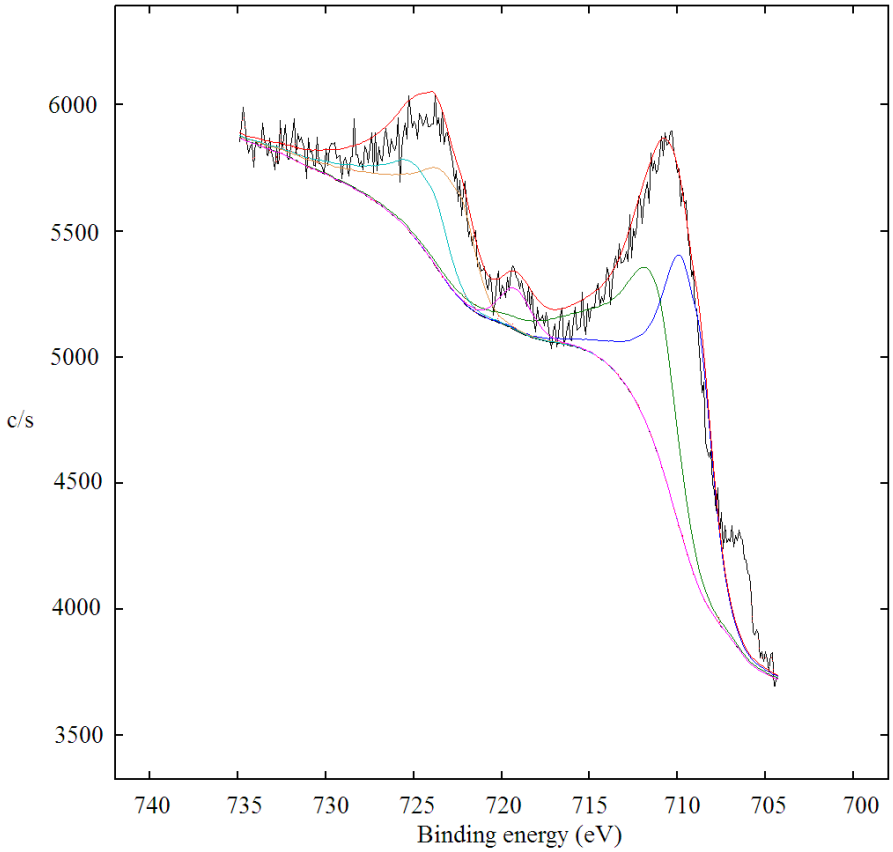

Figure 3.2.2.I XPS spectra of Fe_3O_4 nanoparticles Fe2p region. [$Fe(acac)_3$] = 30 mmol/L (V = 50 mL), Reducing acid solution containing [ascorbic acid] = 25 mmol/L, addition temperature of 70 °C, [water] = 12 mol/L, Dropping rate: 2 mL/min, Volume of the reducing solution: 10 mL.

Mechanism for formation/synthesis of Fe_3O_4 and Fe nanoparticles is proposed and reported by researchers [4] [5]. Asorbic acid mediated reduction of $Fe(acac)_3$ was performed in absence of water i.e. 0 M water. Figure 3.2.2.J (a) represents XRD patterns of samples prepared using ultrapure water and without ultrapure water. In previous results, Figure 3.2.2.E shows a typical XRD spectrum of Fe_3O_4 nanoparticles and all peaks can be indexed as pure Fe_3O_4 phase with inverse spinel structure and matched well with the reported data. No impurities were detected. The crystallite size in Figure 3.2.2.E calculated by Scherrer equation and full-width-at-half-maximum (FWHM) of the strongest peak (3 1 1) is 15 nm. Figure 3.2.2.J show XRD pattern of samples prepared without using ultrapure water. Peaks at 2θ of 30.22˚, 35.4˚, 43.12˚, 57˚ and 62.84˚ having d values as 2.9558, 2.5338, 2.0966, 1.6145, 1.4776 respectively corresponds to iron oxide. This was expected. This is due to the fact that although sample was prepared in oxygen free condition (in presence of nitrogen); however, sample was exposed to air atmosphere during filtration, drying, and XRD measurement process — leading to formation of iron oxide. Broad peaks are indicating the amorphous nature of nanoparticles.

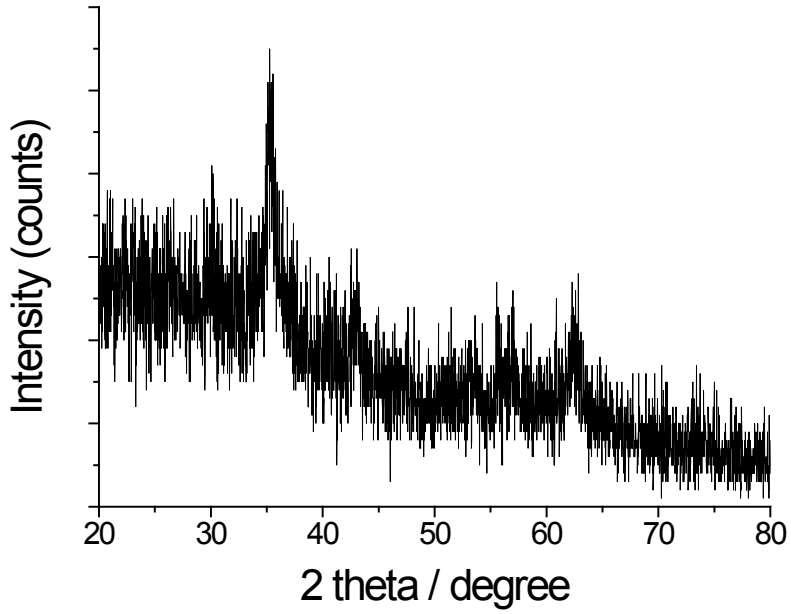

Figure 3.2.2.J XRD pattern of sample prepared without ultrapure water. [$Fe(acac)_3$] = 30mmol/L (V = 50 mL), at 70 °C, Reducing acid solution containing [ascorbic acid] = 25 mmol/L, [water] = 0 mol/L, Dropping rate: 2 mL/min, Volume of the reducing solution: 10 mL.

Figure 3.2.2.K represents the EDAX spectrum of sample prepared without using ultrapure water. EDAX spectrum of sample prepared by using water is represented in previous results in Figure 3.2.2.G. When ultrapure water was used in reaction then magnetite is formed and EDAX spectrum (Figure 3.2.2.G) shows the iron content of 62.16 at. % and oxygen content of 22.23 at. %. Large amount of oxygen is observable in this sample which corresponds to the lattice oxygen (supported by XRD). But when ultrapure water was not used (Figure 3.2.2.K) sample shows high content of iron (85.06 at. %) and very small amount of oxygen (3.89 at. %). We believe that this small amount of oxygen is actually adsorbed oxygen on the surface of iron nanoparticles when they are exposed to oxygen (which is also supported by XRD results). In both the samples, carbon was detected (which is approximately of same amount suggesting our conclusion about oxygen to be true) which arises from carbon tape used for mounting the sample. EDAX measurements were performed at three different locations of each sample and similar results were observed (oxygen of about 3 - 6 at. % for the sample prepared without using water, as against 20 - 30 at. % for the sample prepared with water).

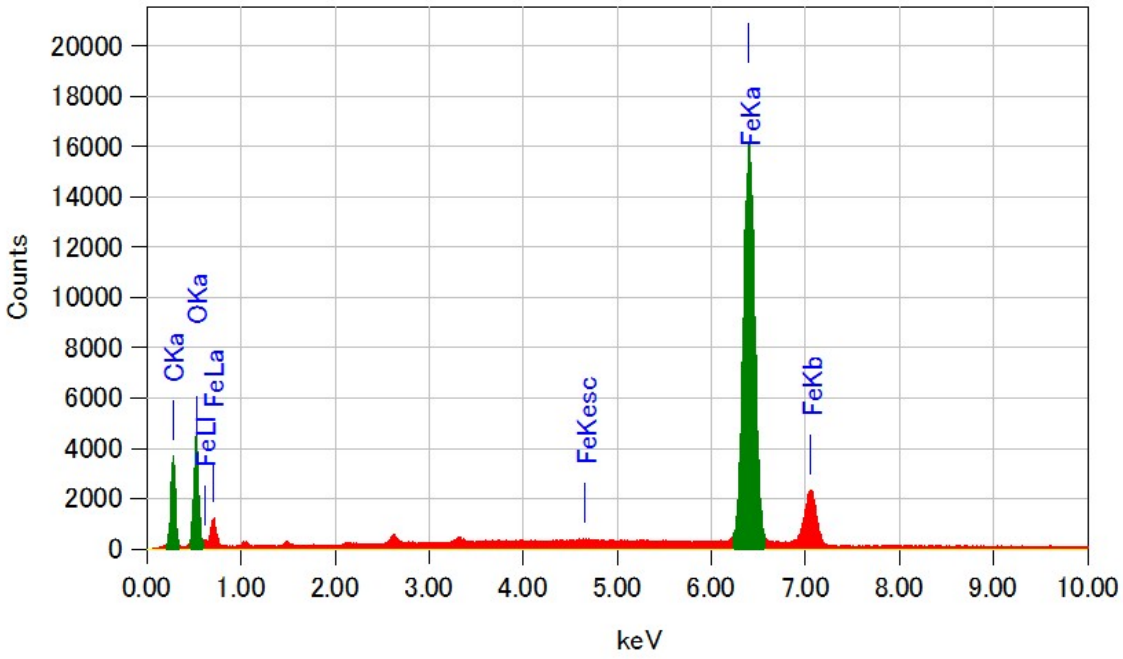

Figure 3.2.2.K EDAX spectrum of sample prepared without ultrapure water. [$Fe(acac)_3$] = 30mmol/L (V = 50 mL), at 70 °C, Reducing acid solution containing [ascorbic acid] = 25 mmol/L, [water] = 0 mol/L, Dropping rate: 2 mL/min, Volume of the reducing solution: 10 mL.

Table 3.2.2.L Elemental composition of Fe, O and C in samples obtained from EDS with and without addition of water during the synthesis process.

Sample	Fe (at. %)	O (at. %)	C (at. %)
Fe_3O_4 (Sample with water)	62.16	22.23	15.61
Fe/iron oxide (Sample without water)	85.06	3.89	11.05

Figure 3.2.2.M represents the TEM images of Fe/iron oxide nanoparticles, respectively. When ultrapure water was used (Figure 3.2.2.F) the mean particle diameter of Fe_3O_4 nanoparticles is observed to be 15±4 nm. In Figure 3.2.2.M, the size of Fe/iron oxide nanoparticles is observed to be 7±1 nm. Although synthesis parameters were same for preparation of both the samples (i.e. with and without water); because of the absence of oxygen (coming from water), smaller size Fe/iron oxide nanoparticles have been obtained.

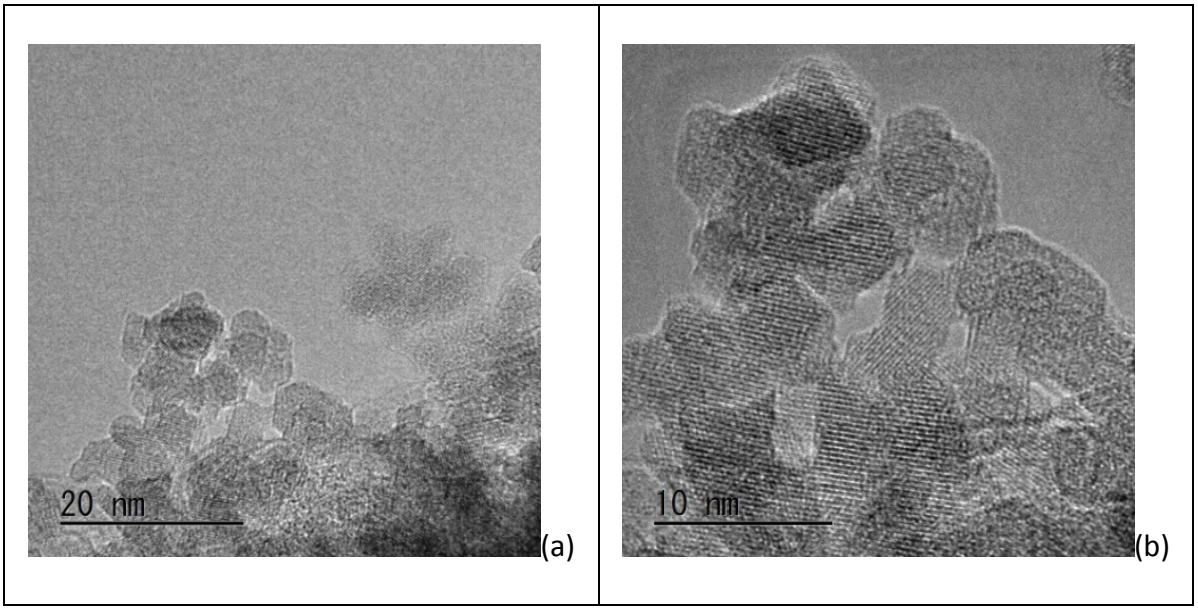

Figure 3.2.2.M HRTEM images of Fe_3O_4 nanoparticles prepared without using ultrapure water at 70 °C, Fe/iron oxide nanoparticles prepared without ultrapure water (a, b). [$Fe(acac)_3$] = 30 mmol/L (V = 50 mL), Reducing acid solution containing [ascorbic acid] = 25 mmol/L, [water] = 0 mol/L, Dropping rate: 2 mL/min, Volume of the reducing solution: 10 mL.

In figure 3.2.2.N, Survey scan of sample (a) and C1s spectrum of C (b) are represented. In survey spectrum all obvious peaks are labeled and can be ascribed to Fe, O, and C. The C1s peak was set to 284.8eV to normalize any peak shifts. Fe2p region of sample prepared without ultrapure water (Figure 3.2.2.N.c) is deconvoluted into seven peaks. Peak at 708 eV and 720.6 eV is assigned to the $2p_{3/2}$ of Fe(0) and $2p_{1/2}$ of Fe(0) [7-10]. Peak at 709.5 eV and 711.8 eV can be assigned to $2p_{3/2}$ of Fe^{2+} and Fe^{3+} species respectively. Photoelectron peak at 723 eV can be assigned to $2p_{1/2}$ of Fe^{2+} species. Peak at 724.9 eV can be assigned to $2p_{1/2}$ of Fe^{3+} species. Peak at 719.02 eV is a satellite peak for all above peaks. As Oxygen content is very low it can not form stoichiometric oxide (FeO, Fe_2O_3, Fe_3O_4) of Fe, it can form only nonstoichiometric oxide at the most hence we speculate the formation of metallic Fe since Oxygen content was very low from EDAX.

Figure (3.2.2.N. a and b) displays the photoelectron spectra of O1s for the sample without using ultrapure water and with ultrapure water, respectively. Figure 3.2.2.O (a) represents O1s photoelectron spectrum for the sample prepared with ultrapure water (12 M water).This O1s spectrum can be deconvoluted into two peaks at 531.6 eV corresponding to O-Fe in magnetite phase [11] and 529.38 eV corresponding to adsorbed oxygen [12, 13]. In Figure 3.2.2.N (b), O1s spectrum of sample prepared without ultrapure water (0 M water) is presented and it can be deconvoluted into two peaks at 531.29 eV and 529.6 eV. These peaks are due to formation of non-stoichiometric oxides on the surface of the nanoparticles [10]. This might be due to two reasons: (a) XPS is a surface sensitive technique with very small penetration depth (about 5

nm), and (b) sample prepared without using ultrapure water gets oxidized when exposed to air atmosphere while handling. This was expected due to high reactivity of iron in nanoparticulate form and its affinity and high reactivity towards oxygen. Formation of iron oxide on the surface of iron nanoparticles is also reported earlier by other researchers [5, 6, 8, 9].

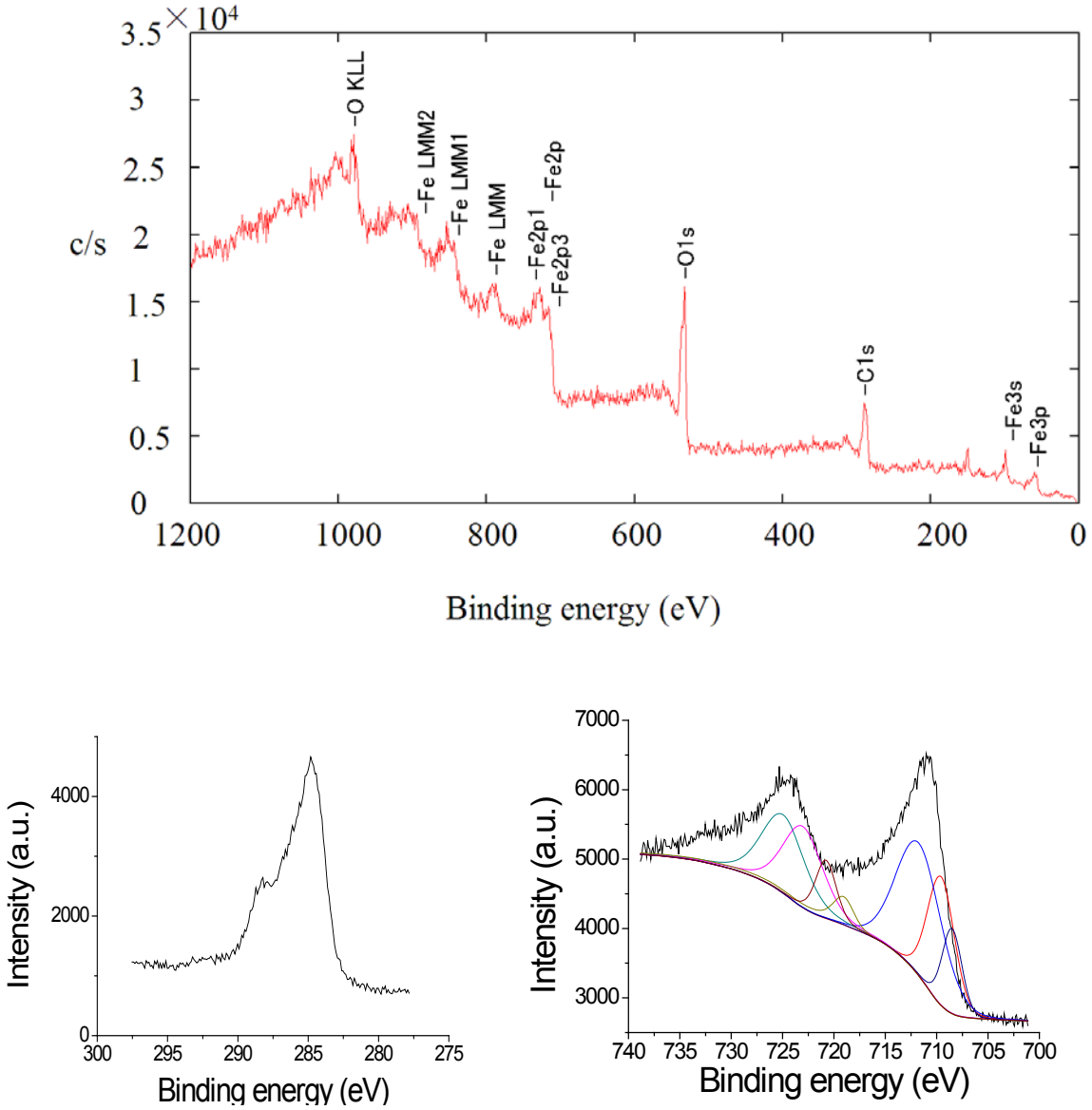

Figure 3.2.2.N Survey XPS scan (a), C1s spectrum of C (b), XPS Fe2p spectrum of sample prepared without using ultrapure water 0 mol/L (c),
$[Fe(acac)_3]$ = 30 mmol/L (V = 50 mL), reducing acid solution containing [ascorbic acid] = 25 mmol/L, Dropping rate: 2 mL/min, Volume of the reducing solution: 10 mL.

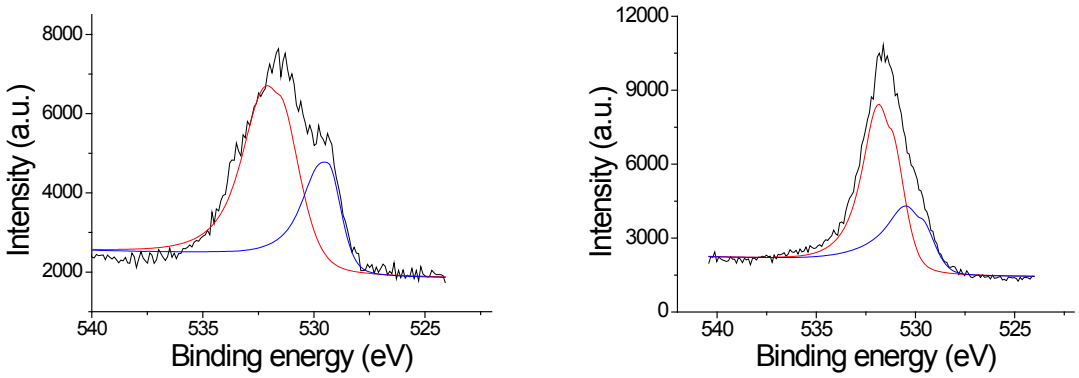

(a) (b)

Figure 3.2.2.O O1s spectrum of O in sample prepared with water 12 mol/L (a), O1s spectrum of O in sample prepared without water i.e. 0 mol/L (b),
[$Fe(acac)_3$] = 30 mmol/L (V = 50 mL), reducing acid solution containing [ascorbic acid] = 25 mmol/L, Dropping rate: 2 mL/min, Volume of the reducing solution: 10 mL.

3.2.3 Influence of $Fe(acac)_3$ concentration

Figure 3.2.3.A represents XRD pattern of samples prepared at 70 °C addition temperature and different $Fe(acac)_3$ concentrations (50 mM and 15 mM). In Fig.3.2.3.A (b) seven diffraction peaks observed at 2θ = 18.30, 30.06, 35.48, 43.03, 53.44, 56.95, 62.5. These peaks are due to due to (111), (220), (311), (400), (422), (511) and (440) crystal plane of Fe_3O_4, respectively. The average particle diameter of Fe_3O_4 particles was estimated with full-width at half maximum (FWHM) of an X-ray diffraction peak and Scherrer equation was 9 nm. In Fig. 3.2.3.A (a) five weak and broad peaks observed at 2θ= 18.30, 31.60, 34.93, 56.95, 62.77. These peaks are due to (111), (220), (311), (511), (440) crystal plane of Fe_3O_4.

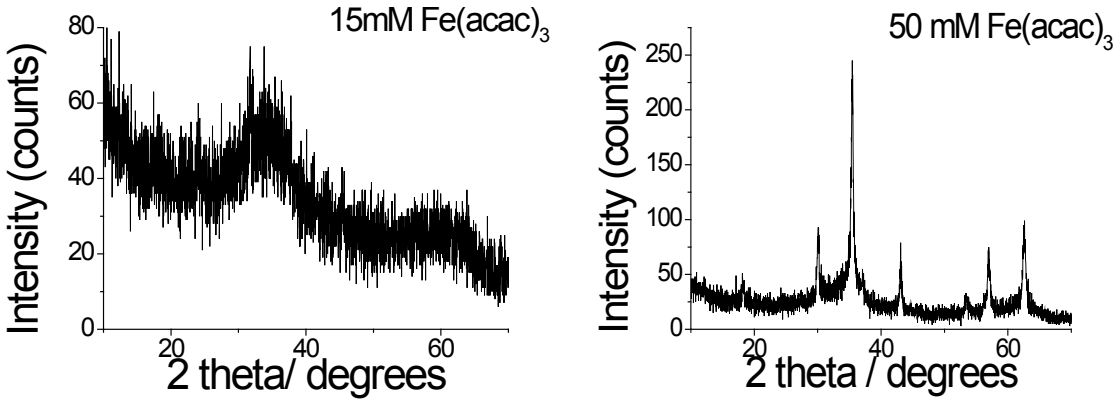

(a) (b)

Figure 3.2.3.A XRD pattern of sample prepared with addition of ascorbic acid at 70°C and at different precursor [$Fe(acac)_3$] (V= 50 mL) concentrations, (a) at 15mM $Fe(acac)_3$, (b) at 50mM $Fe(acac)_3$. Reducing acid solution containing [ascorbic acid] = 25 mmol/L, [water] = 12 mol/L, Dropping rate: 2 mL/min, Volume of the reducing solution: 10 mL.

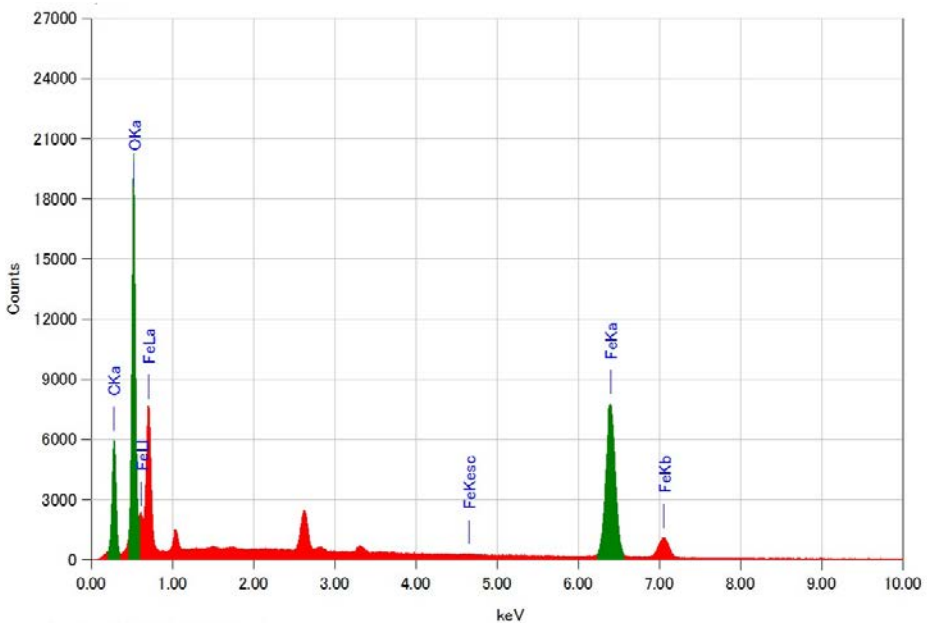

Figure 3.2.3.B EDAX spectrum of sample prepared with addition of ascorbic acid at 70 °C and at 15 mM precursor [$Fe(acac)_3$] (V = 50 mL) concentration. Reducing acid solution containing [ascorbic acid] = 25 mmol/L, [water] = 12 mol/L, Dropping rate: 2 mL/min, Volume of the reducing solution: 10 mL.

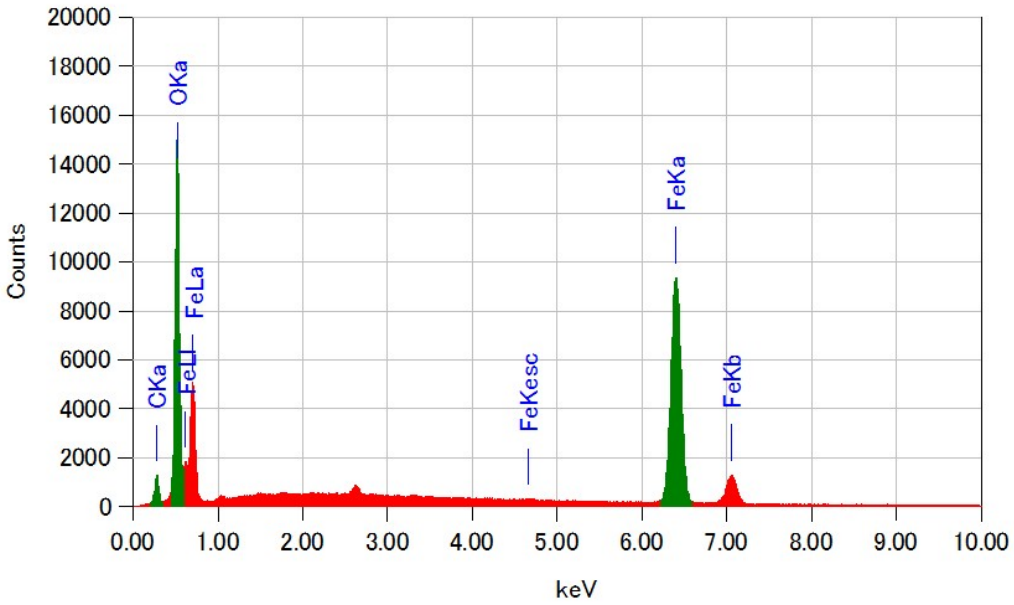

Figure 3.2.3.C EDAX spectrum of sample prepared with addition of ascorbic acid at 70 °C and at 50 mM precursor [$Fe(acac)_3$] (V = 50 mL) concentration. Reducing acid solution containing [ascorbic acid] = 25 mmol/L, [water] = 12 mol/L, Dropping rate: 2 mL/min, Volume of the reducing solution: 10 mL.

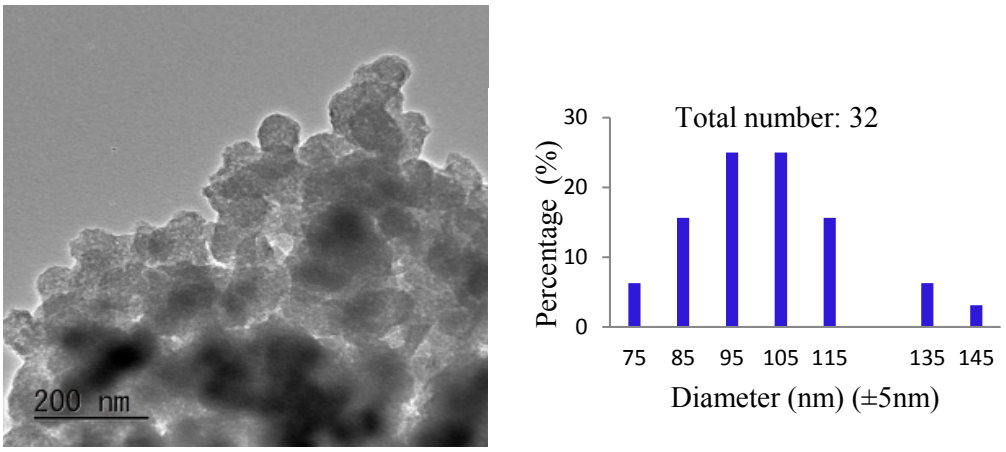

(a)

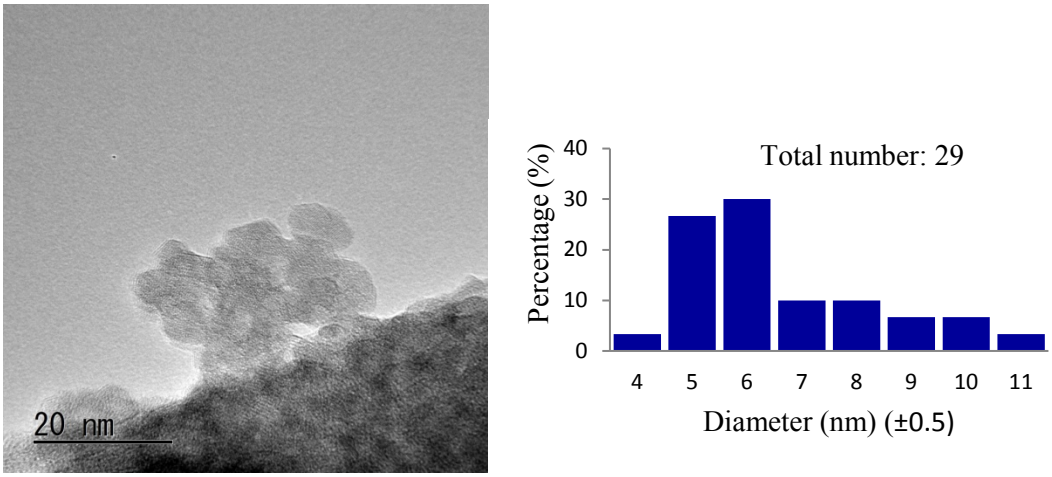

(b)

Figure 3.2.3.D TEM and HRTEM images and particle diameter distribution histogram of nanoparticles prepared at addition temperature at 70 °C and at different precursor concentration, (a) TEM images of nanoparticles at 15 mM [$Fe(acac)_3$] (V = 50 mL) concentration, (b) HRTEM images of nanoparticles at 50 mM [$Fe(acac)_3$] (V = 50 mL) concentration. Reducing acid solution containing [ascorbic acid] = 25 mmol/L, [water] = 12 mol/L, Dropping rate: 2 mL/min, Volume of the reducing solution: 10 mL.

Figure 3.2.3.B and Figure 3.2.3.C represents EDAX spectra of nanoparticles prepared at addition temperature of 70 °C and at 15 mM and 50 mM of $Fe(acac)_3$ concentration respectively. The result confirms the presence of iron and oxygen. Carbon detected is due to carbon tape used for mounting the sample.

Figure 3.2.3.D shows TEM, HRTEM images and particle diameter distribution of nanoparticles prepared at addition temperature of 70 °C and at different precursor concentration. In Fig.

3.2.3.D (b), it was observed that at 50 mM $Fe(acac)_3$ concentration, the mean particle diameter of Fe_3O_4 nanoparticles was 9±1 nm. From Fig. 3.2.3.D (a) it was observed that at 15 mM $Fe(acac)_3$ concentration, the mean particle diameter of Fe_3O_4 nanoparticles was 108±21 nm. Results show that Fe_3O_4 nanoparticle size increases with decrease in $Fe(acac)_3$ concentration and Fe_3O_4 nanoparticle size decreases with increase in $Fe(acac)_3$ concentration. This might be due to number of nuclei or nucleation sites increases with increase in $Fe(acac)_3$ concentration and nuclei or nucleation sites decreases with decrease in $Fe(acac)_3$ concentration .

3.2.4 Influence of Ascorbic acid concentration

Figure 3.2.4.A represents XRD pattern of samples prepared at addition temperature of 70°C and at different ascorbic acid concentrations (0.05 mM and 0.005 mM). In Fig. 3.2.4.A (a) two weak and broad diffraction peaks observed at 2θ= 34.67, 61.02. These peaks are due to due to (311), (440) crystal plane of Fe_3O_4, respectively. In Figure 3.2.4.A (b) two weak and broad peaks observed at 2θ= 35.33, 62.5. These peaks are due to (311), (440) crystal plane of Fe_3O_4.

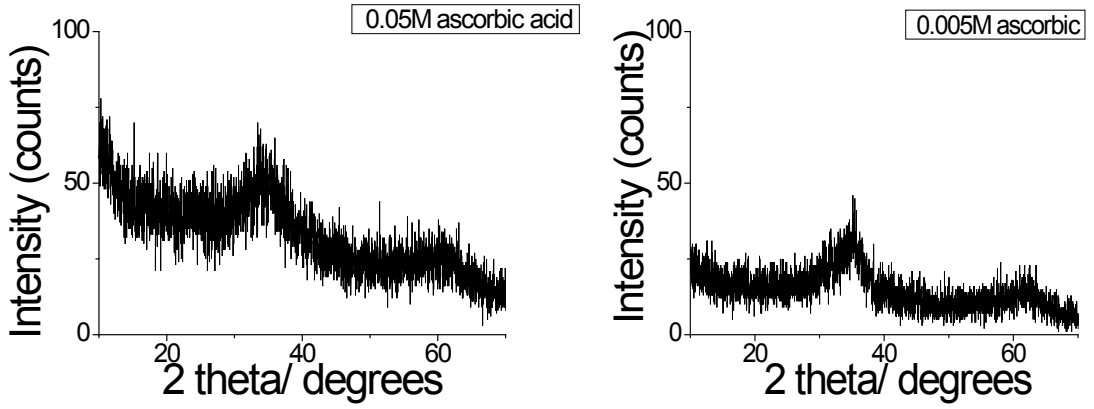

(a) (b)

Figure 3.2.4.A X-ray diffraction pattern of sample prepared with addition temperature at 70 °C and reducing acid solution containing [ascorbic acid], (a) at 0.05 M, (b) at 0.005 M. [$Fe(acac)_3$] = 30 mmol/L (V = 50 mL), [water] = 12 mol/L, Dropping rate: 2 mL/min, Volume of the reducing solution: 10 mL.

Figure 3.2.4.B and Fig. 3.2.4.C represents EDAX spectra of nanoparticles prepared at addition temperature of 70 °C and at 0.005 M and 0.05 M concentration of ascorbic acid respectively. The result confirms the presence of iron and oxygen. Carbon detected is due to carbon tape used for mounting the sample.

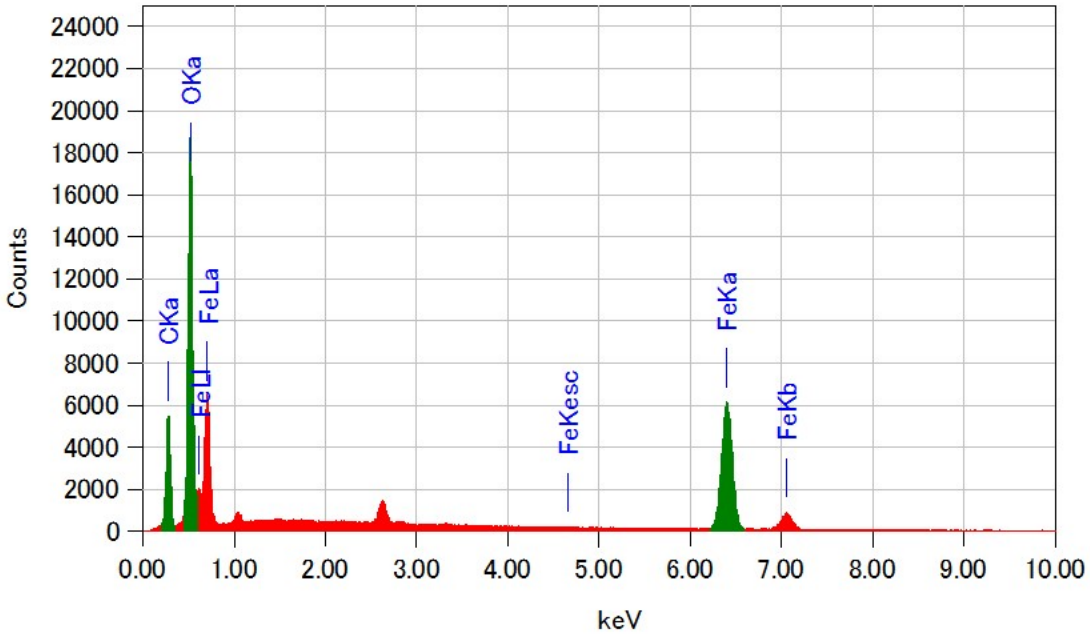

Figure 3.2.4.B EDAX spectrum of sample prepared with addition temperature of 70 °C and reducing acid solution containing [ascorbic acid] 0.005 M. [$Fe(acac)_3$] = 30mmol/L (V = 50 mL), [water] = 12 mol/L, Dropping rate: 2 mL/min, Volume of the reducing solution: 10 mL.

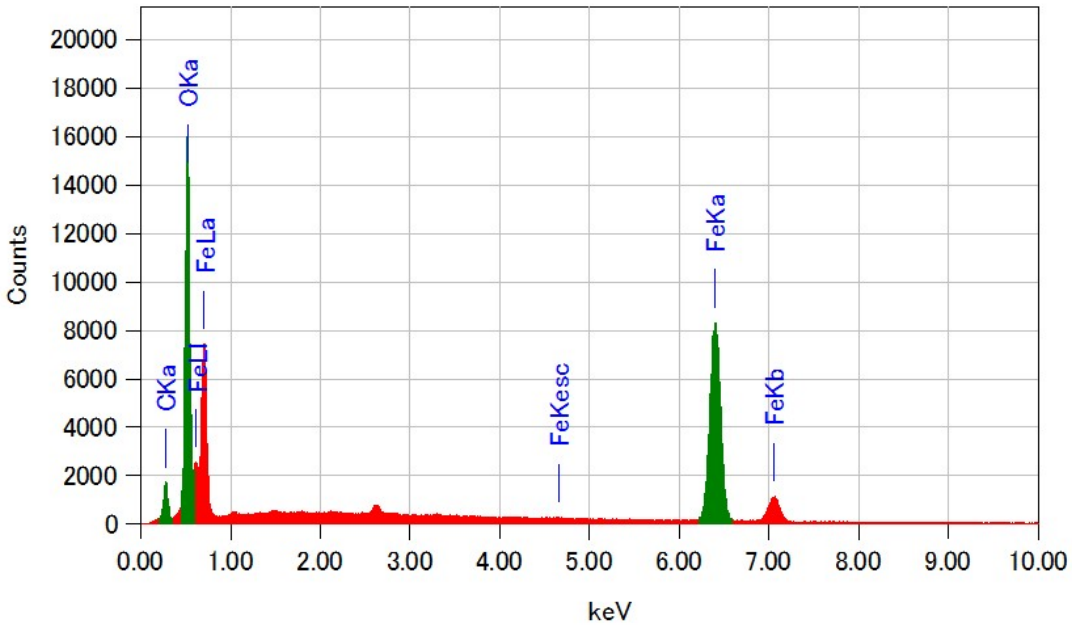

Figure 3.2.4.B EDAX spectrum of sample prepared with addition temperature of 70 °C and reducing acid solution containing [ascorbic acid] 0.05 M. [$Fe(acac)_3$] = 30 mmol/L (V = 50 mL), [water] = 12 mol/L, Dropping rate: 2 mL/min, Volume of the reducing solution: 10 mL.

Figure 3.2.4.D shows HRTEM images and particle diameter distribution of nanoparticles

prepared at addition temperature of 70 °C and at different precursor concentration. It was observed (in Fig. 3.2.4.D.b) that at 0.05 M ascorbic acid concentration, the mean particle diameter of Fe_3O_4 nanoparticles was 9±3 nm. From Fig. 3.2.4.D (a) it was observed that at 0.005 M ascorbic acid concentration, the mean particle diameter of Fe_3O_4 nanoparticles was 76±29 nm. Results show that Fe_3O_4 nanoparticle size decreases with increase in ascorbic acid concentration and Fe_3O_4 nanoparticle size increases with decrease in ascorbic acid concentration. This might be due to number of nuclei or nucleation sites in increasing with increase in ascorbic acid concentration and number of nuclei or nucleation sites decreasing with decrease in ascorbic acid concentration.

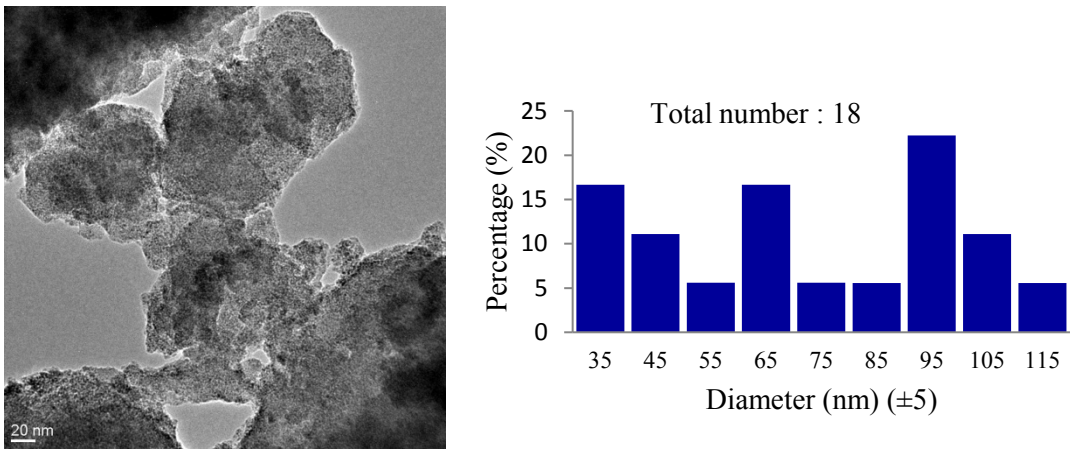

(a)

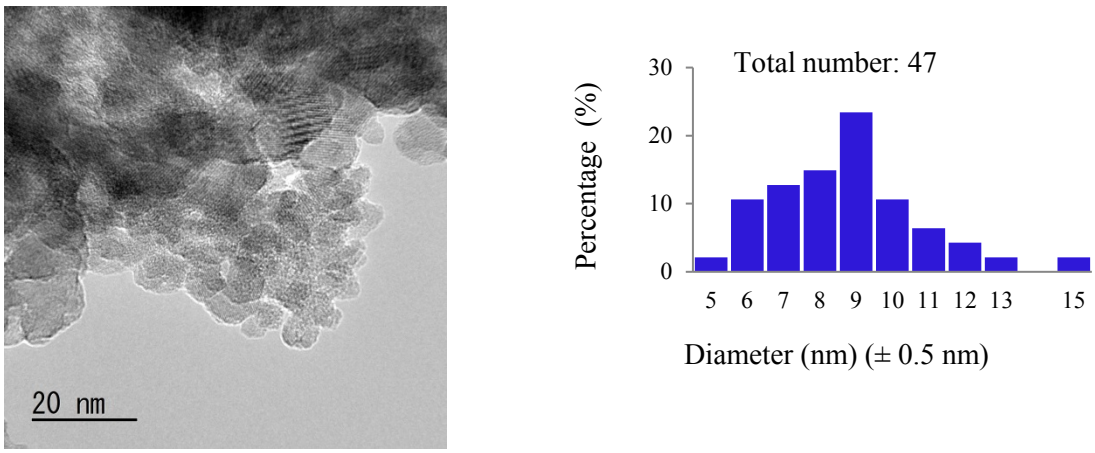

(b)

Figure 3.2.4.D HRTEM images and particle diameter distribution histogram of nanoparticles prepared at addition temperature of 70 °C and at different ascorbic acid concentrations, (a) HRTEM images of nanoparticles at 0.005 M ascorbic acid concentration, (b) HRTEM images of nanoparticles at 0.05M ascorbic acid concentration. $[Fe(acac)_3]$ = 30 mmol/L (V = 50 mL), [water] = 12 mol/L, Dropping rate: 2 mL/min, Volume of the reducing solution: 10 mL.

3.2.5 Influence of dropping rate

Figure 3.2.5.A represents XRD pattern of samples prepared at 70 °C addition temperature and at dropping rate of 1 ml/min. In Fig. 3.2.5.A five diffraction peaks observed at 2θ= 30.06, 35.33, 43.03, 56.95, 62.5.These peaks are due to due to (220), (311), (400), (511), (440) crystal plane of Fe_3O_4, respectively. Mean particle diameter was 8±2 nm. Fig. 3.2.5.B represents EDAX spectra of nanoparticles prepared at addition temperature of 70 °C and at 1ml/min of dropping rate. The result confirms the presence of iron and oxygen. Carbon detected is due to carbon tape used for mounting the sample.

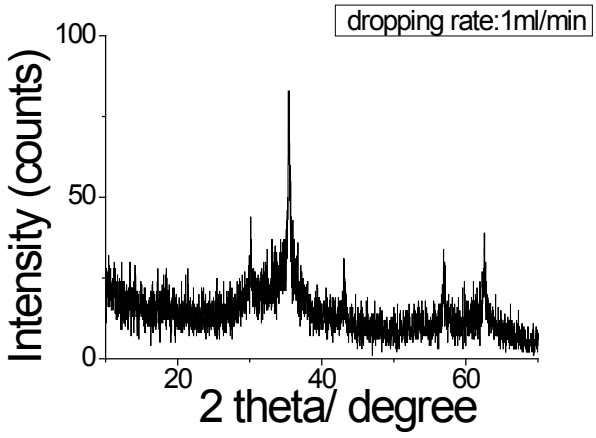

Figure 3.2.5.A X-ray diffraction pattern of sample prepared with addition temperature at 70 °C and at 1 mL/min dropping rate. [$Fe(acac)_3$] = 30 mmol/L (V = 50 mL), Reducing acid solution containing [ascorbic acid] = 25 mmol/L, [water] = 12 mol/L, Volume of the reducing solution: 10 mL.

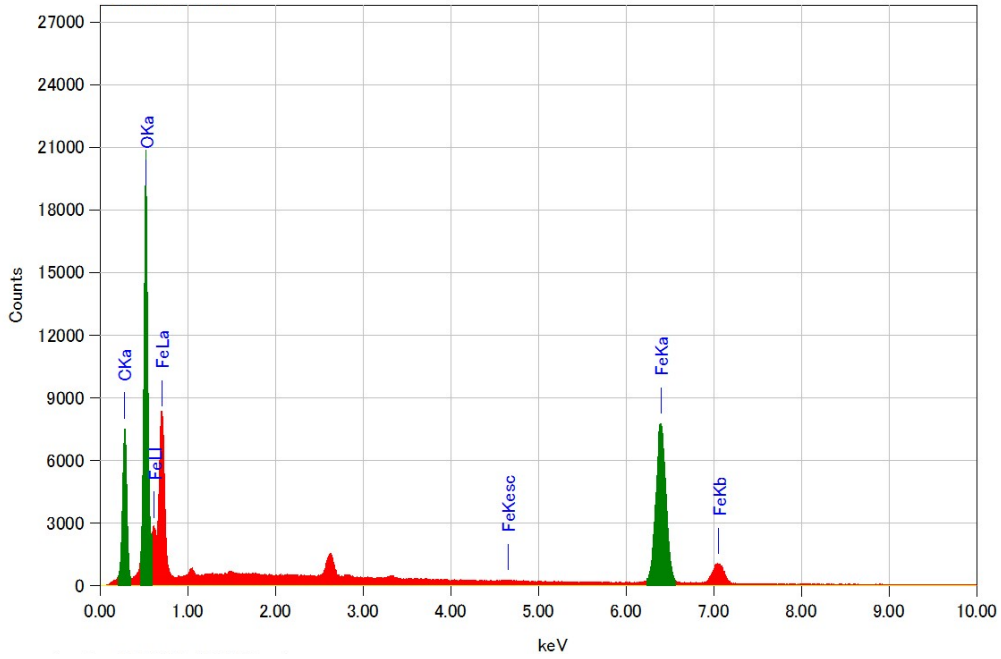

Figure 3.2.5.B EDAX spectrum of sample prepared with addition temperature of 70 °C and at dropping rate of 1 mL/min. [$Fe(acac)_3$] = 30 mmol/L (V = 50 mL), Reducing acid solution containing [ascorbic acid] = 25 mmol/L, [water] = 12 mol/L, Volume of the reducing solution: 10 mL.

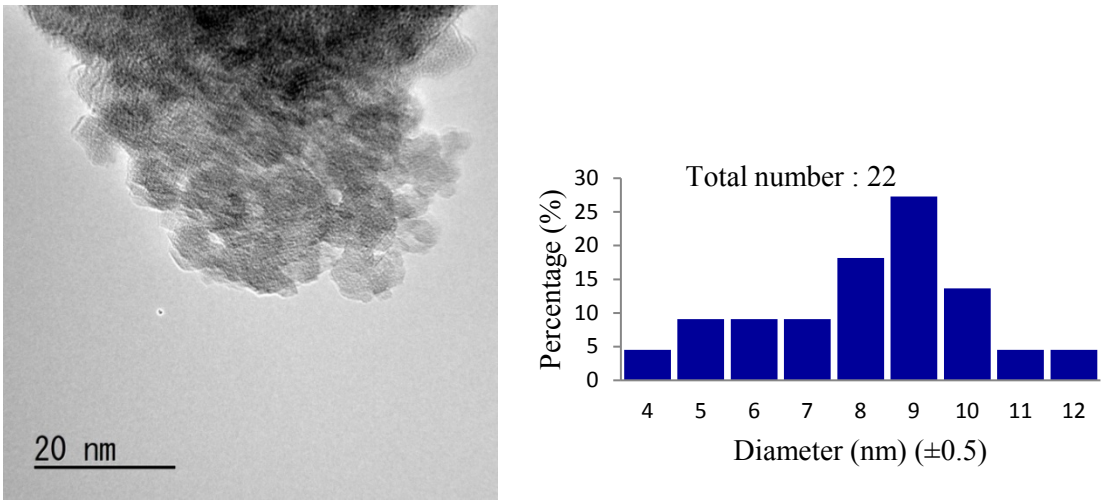

Figure 3.2.5.C HRTEM images and particle diameter distribution histogram of nanoparticles prepared at addition temperature of 70 °C and at 1 mL/min dropping rate. [$Fe(acac)_3$] = 30 mmol/L (V = 50 mL), Reducing acid solution containing [ascorbic acid] = 25 mmol/L, [water] = 12 mol/L, Volume of the reducing solution: 10 mL.

Figure 3.2.5.C shows HRTEM images and particle diameter distribution histogram of nanoparticles prepared at addition temperature of 70 °C and at 1ml/min dropping rate. It was observed in Figure 3.2.5.C at 1ml/min dropping rate, the mean particle diameter of Fe_3O_4

nanoparticles was 8± 2 nm. Results show that Fe_3O_4 nanoparticle size decreases with decrease in ascorbic acid solution dropping rate. This might be due to when dropping rate decreases number of nuclei or nucleation sites is increasing.

3.3 Discussion

In this synthesis process, ascorbic acid acts as reducing agent and ultrapure water acts as supplier of oxygen. The role of dehydrated ethanol is a solvent in ascorbic acid solution. $Fe(acac)_3$ in diphenyl-ether is reduced by ascorbic acid and hydrolyzed by ultrapure water. Fe(III) ion is reduced by the ascorbic acid and $Fe_2^{3+}Fe^{2+}(OH)_8$ (precursor) is synthesized. Then the reaction system is heated at 190 °C for several times (30, 60, 90 min). This heating process (annealing) is very important as the crystallization process of precursor particles.

$$6Fe(III)(acac)_3 + \text{ascorbic acid (act as reducer)} + 8H_2O$$

$$\text{------ > } 2Fe_3O_4 + \text{dehydroascorbic acid} + 18\text{acac}$$

Ascorbic acid reduces the $Fe(acac)_3$ as follows:

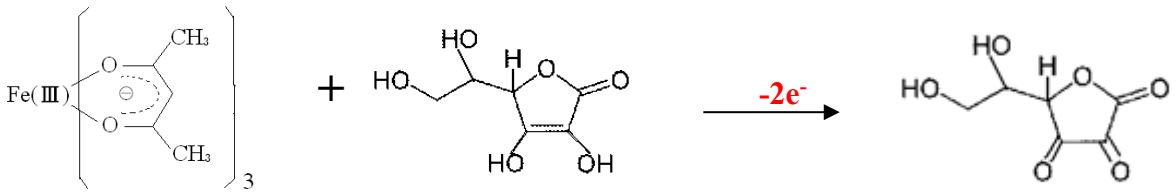

$Fe(acac)_3$ Ascorbic acid dehydroascorbic acid

Fe^{2+} is formed because of reduction of $Fe^{3+}(acac)_3$ by ascorbic acid, and because of ultrapure water Fe $(OH)_2$ is generated as follows:

$$Fe^{3+}(acac)_3 + ½\ (C_6H_8O_6) \longrightarrow Fe^{2+}$$

$$2H_2O \rightleftharpoons 2H^+ + 2(OH)^-$$

$$Fe^{2+} + 2(OH)^- \longrightarrow Fe\ (OH)_2$$

And $2Fe(OH)_3$ is formed as follows:

$$6H_2O \rightleftharpoons 6H^+ + 6(OH)^-$$

$$2Fe(acac)_3 + 6(OH)^- + 6H^+ \longrightarrow 2Fe(OH)_3$$

In general, $Fe(acac)_3$ is reduced by ascorbic acid and $Fe_3(OH)_8$ is synthesized as follows :

$$2Fe^{3+} + Fe^{2+} + 8H_2O \longrightarrow Fe_2^{3+}Fe^{2+}(OH)_8$$

When reaction mixture is heated to reflux, it results in crystallization of Fe_3O_4 nanoparticles and hydrolysis. The formation of Fe_3O_4 is as follows:

$$Fe_3(OH)_8 \xrightarrow{\text{reflux}} Fe_3O_4 + 4H_2O$$

The general reaction can be written as:

$$6Fe(acac)_3 + C_6H_8O_{6(\text{reductant})} + 8H_2O \longrightarrow 2Fe_3O_4 + C_6H_6O_{6(\text{oxidant})} + 18(acac)$$

In this method, ultrapure water is oxygen supplier thereby explaining the formation mechanism of magnetite nanoparticles. Size controlled synthesis of Fe_3O_4 nanoparticles without any capping agent is achieved by ascorbic acid mediated reduction of $Fe(acac)_3$.

A study on decomposition efficiency of $Fe(acac)_3$ was carried out at different addition temperatures and ultrapure water concentrations. Decomposition efficiency of $Fe(acac)_3$ was estimated at different addition temperatures and ultrapure water concentrations. Decomposition efficiency (%) of $Fe(acac)_3$ increases with respect to increase in addition temperature, this may be due to rate of reaction increases as addition temperature increases. It was also observed that decomposition efficiency increases with respect to time showing that precursor gets reduced by ascorbic acid. Final decomposition efficiency was estimated after the refluxing reaction mixture at 190°C for 1 hour and cooling down naturally to room temperature in all experiments. It was observed that there was no significant difference in absorbance after the completion of reaction. Final decomposition efficiency (90-100%) indicates near-complete utilization of $Fe(acac)_3$ in reaction. This might be due to the fact that almost all precursor was used when reactants were in stoichiometric ratio. There was no significant effect of ultrapure water concentration changes on decomposition efficiency. At 60 °C (12 M water), after 25 minutes decomposition efficiency was found to be 33.57 %, indicating 1/3 reduction of precursor $Fe(acac)_3$ by ascorbic acid. When reactants were added in stoichiometric ratio the decomposition efficiency of $Fe(acac)_3$ after the completion of reaction was in the range of 90-100%, shows that almost all precursor was utilized in reaction.

It was observed that magnetite (Fe_3O_4) can be synthesized when addition of reducing acid solution was carried out at room temperature but the sample was largely aggregated. Fe_3O_4 nanoparticles having size 29 ±9 nm were synthesized at addition temperature of 60 °C and at 1.2 M ultrapure water. Fe_3O_4 nanoparticles with diameter 33±3 nm and 42±5 nm were

successfully synthesized at 1.2 M ultrapure water concentration and addition temperature of 70°C and 80°C respectively. From these results it can be conclude that at 1.2 M ultrapure water concentration, Fe_3O_4 nanoparticle size increases with increase in addition temperature.

Fe_3O_4 nanoparticles having diameter 22±6 nm and 8±2 nm were successfully synthesized at addition temperature of 60 °C, 80 °C and at 12 M ultrapure water. Size controlled synthesis of Fe_3O_4 nanoparticles having diameter 15± 4 nm was successfully carried out at 12 M ultrapure water concentration and at addition temperature of 70 °C. Reaction parameters were optimized to synthesize size controlled Fe_3O_4 nanoparticles with diameter less than 30 nm. It was observed that Fe_3O_4 nanoparticle size decreases with increase in ultrapure water concentration.

Fe_3O_4 nanoparticles with diameter 9±1 nm and 108±21 nm were synthesized at 50 mM and 15 mM $Fe(acac)_3$ concentrations respectively. It was observed that at addition temperature of 70 °C Fe_3O_4 nanoparticle size decreases with increase in $Fe(acac)_3$ concentration and size increases with decrease in $Fe(acac)_3$ concentration.

Fe_3O_4 nanoparticles having diameter 9±3 nm and 76±29 nm were synthesized at 0.05 M and 0.005 M ascorbic acid concentration. At addition temperature of 70 °C nanoparticle size is inversely proportional to the concentration of ascorbic acid.

Fe_3O_4 nanoparticles having diameter 8±2 nm were synthesized at 1mL/min dropping rate and it was observed that at 70°C if dropping rate was reduced to 1 mL/min the Fe_3O_4 nanoparticle size is reduced.
If ultrapure water is not used in reaction, then $Fe(acac)_3$ is reduced by ascorbic acid; but due to lack of oxygen source Fe_3O_4 is not formed, leading to formation of Fe/iron oxide nanoparticles. It was observed that may be such Fe nanoparticles get oxidized to form Fe/iron oxide nanoparticles having size 7 ± 1 nm due to exposure to air atmosphere. This also proves that ultrapure water is oxygen supplier in our reaction. In polyol-methods, the exact mechanism leading to formation of Fe_3O_4 and origin of oxygen element in Fe_3O_4 is still unclear. Our mechanism proves the origin of oxygen and the role of water during our synthesis process.

Mechanism for the synthesis of Fe_3O_4 nanoparticles is proposed. Method presented herewith should prove to be very useful for synthesis of Fe_3O_4 nanoparticles having surface available for further use such as uploading of drug molecules for biomedical applications or other applications.

References:

1. A. Dakhela, A. Ali-Mohamed, Preparation and characterisation of crystalline tris(acetylacetonato)Fe(III) films grown on p-Si substratefor dielectric applications, Journal of Physics and Chemistry of Solids 68, 162–167, 2007.
2. M. Kraken, I. Masthoff, A. Borchers , F. Litterst, G. Garnweitner, Formation of magnetic nanoparticles studiedduring the initial synthesis stage, Hyperfine Interact 224, 57, 2014.
3. J. Zabicky, Z. Rappoport, The chemistry of metal enolates- 2 volume set, Part 1, 1250 pages, ISBN: 978-0-470-06168-8, John Willey and Sons, 2009.
4. Sheng Peng, Chao Wang, Jin Xie, Shouheng Sun, Synthesis and Stabilization of Monodisperse Fe Nanoparticles, J. Am. Chem. Soc. 128, 10676, 2006.
5. D. Prabu, R. Parthiban, Synthesis and Characterization of Nanoscale Zero Valent Iron (NZVI) Nanoparticlesfor Environmental Remediation, Asian J. Pharm. Tech. 3, 181, 2013.
6. G. Martinez, A. Malumbres, R. Mallada, J. Hueso, S. Irusta, O. Bomati-Miguel, Use of a polyol liquid collection medium to obtain ultrasmall magnetic nanoparticles by laser pyrolysis, J. Santamaria, Nanotechnology 23, 425605, 4, 2012.
7. Y. Sun, X. Li, W. Zhang, H. Paul Wang, A Method for the Preparation of Stable Dispersion of Zero-Valent Iron Nanoparticles, Colloids and Surfaces A: Physicochem. Eng. Aspects 308, 60, 2007.
8. Y. Sun, X. Li, J. Cao, W. Zhang, H. Paul Wang, Characterization of Zero-Valent Iron Nanoparticles, Adv. Colloid Interface Sci. 120, 47, 2006.
9. S. Watson, H. Mohamed, B. Horrocksa, A. Houlton, Electrically Conductive Magnetic Nanowires Usingan Electrochemical DNA-Templating Route, Nanoscale 5, 5349, 2013.
10. NIST X-ray Photoelectron Spectroscopy Database, Version 4.1 (National Institute of Standards and Technology, Gaithersburg, 2012); http://srdata.nist.gov/xps/.
11. F. Marquez, G. Herrera, T. Campo, M. Cotto, J. Duconge, J. Sanz, E. Elizalde, O. Perales, C. Morant, Preparation of hollow magnetite microspheres and their applications as drugs carriers, Nanoscale Research Letters 7:210, 1-11, 2012.
12. N. Eltounya, P. Ariya, Competing reactions of selected atmospheric gases on Fe_3O_4 nanoparticles surfaces, Phys.Chem.Chem.Phys.**,** 16, 23056**,** 2014.
13. Y. Liu, L. Liao, C. Pan, J. Li, Y. Dai, W. Chen, Modulated structure assisted growth and properties of Fe3O4 nanoneedles films using a thermal oxidation process in the air, J. Phys. Chem. C 112, 902-910, 2008.

Chapter 4: Synthesis and characterization of graphene-Fe_3O_4 nanocomposite

4.1 Introduction

4.1.1 Graphene

In October 2004, Konstantin Novoselov, Andre Geim and their collaborators showed that a single layer from graphite could be isolated and transferred to another substrate and that electrical characterization could be done on a few such layers. In graphene carbon is packed in hexagonal (honeycomb) lattice with a carbon-carbon distance 0.142 nm. It is a truly two dimensional crystalline material. Graphene is a single atomic layer of carbon. Graphene has variety of interesting properties which makes it important for fundamental studies and future applications. The electronic property of graphene leads to an unusual quantum hall effect. Graphene is a one atom thin transparent conductor. Thermal and electrical conductivity of graphene is very high and it can be used as a flexible conductor. Graphene is a single layer of carbon packed in a hexagonal (honeycomb lattice). Each atom in graphene has four bonds, three σ bonds with neighbouring carbon atoms and one π-bond oriented out of plane. Graphene is stable due to closely packed carbon atoms and sp^2 hybridization. Graphene is a zero band gap semiconductor in which charge carriers behaves as massless Dirac fermions. Graphene has high electron mobility at room temperature due to weak electron phonon interaction. Due to unique thermal, optical, electronic, mechanical properties graphene has potential applications in energy storage, FET (field effect transistors), catalysis, sensors, drug delivery, and cancer therapy and in LED (light emission diodes). Table 4.1.1.B represents some properties of graphene [1- 4].

Table 4.1.1.B. Properties of Graphene [1].

Property	Details
Density	0.77 mg / m^2
Optical transparency	Absorbs 2.3% light, almost transparent, graphene suspension does not have any color
Strength	Breaking strength is 42N/m
Electrical conductivity	Using layer thickness the bulk conductivity is $0.96x10^6$ $\Omega^{-1}cm^{-1}$
Thermal conductivity	5000 $Wm^{-1}k^{-1}$

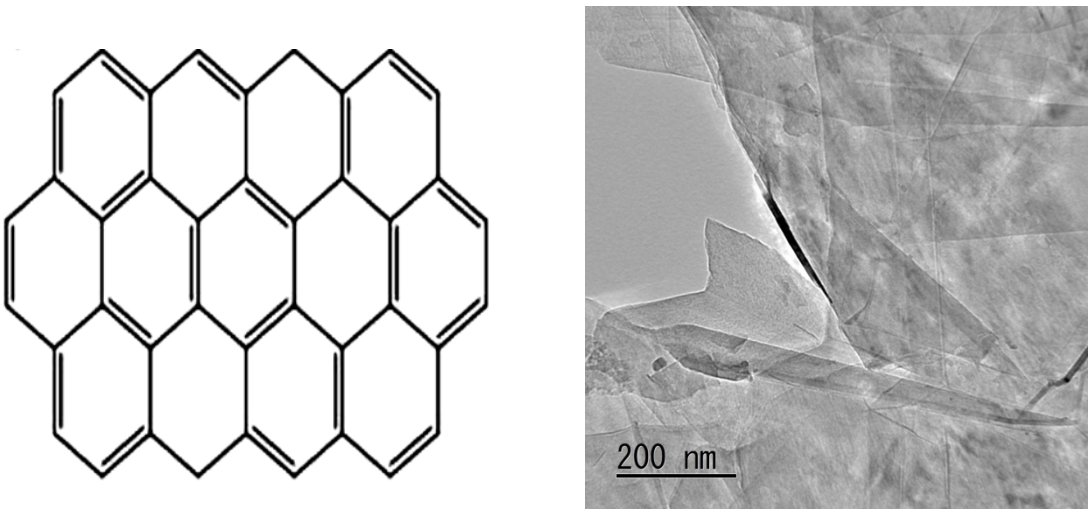

(a) (b)

Figure 4.1.1.A Chemical structure of graphene (a) [4], TEM image of graphene (b).

4.1.2 Graphene-Fe_3O_4 nanocomposite

Graphene has attracted lots of attention due to its excellent electrical and mechanicalproperties, since from its discovery in 2004 [5]. Somani et. al. have demonstrated synthesis of planer nano-graphenes from camphor by CVD method first time in the world [6]. Structure of graphene is a honeycomb lattice which is a two dimensional in which carbon atoms are bonded together with σ bonds [7 - 14]. Graphene is coupled with nanoparticles of other materials for various applications. Deposition of nanoparticles is possible on graphene surface because of its two-dimensional structure and high surface area [15]. Nanoparticles of different materials such as metal oxides [15, 16], metals [17], quantum dots [18], sulfides [19] etc. have been combined with graphene for various applications. This helps in two ways: nanoparticles remains anchored on graphene sheet and do not get agglomerated, and also prevents graphene sheets from their reassembly into graphite or aggregation in a bulky form. Deposition of nanoparticles on graphene is observed to enhance its electrical, mechanical, and thermal properties [20]. Graphene based nanocomposites have also potential applications in biosensing, solar cell, magnetic resonance imaging (MRI), drug delivery, photocatalysis, electrodes of energy storage devices such as that of supercapacitors and batteries [21 - 25] etc.

Fe_3O_4 nanoparticles are of special interest due to their magnetic properties and possible applications in cancer hyperthermia, MRI imaging etc. In earlier studies, Fe_3O_4 nanoparticles have been deposited on graphene oxide.

In these efforts, graphene is first converted into graphene oxide and then nanoparticles are deposited on graphene oxide. Ma et. al. made functionalized graphene-Fe_3O_4 nanocomposite by dispersing graphene oxide, $FeCl_3.6H_2O$ in a mixture of ethylene glycol and diethylene glycol followed by heating at 200 °C for 10 hours [26]. Major drawback of this approach is

that the reaction needs very long time. Also the size distribution of nanoparticles is very wide (from 50 nm to 300 nm). Guan et. al. assembled Fe_3O_4 nanoparticles on graphene by stirring Fe_3O_4 nanoparticles and graphene in hexane overnight and then sonicating for 2 hours [27]. However, Fe_3O_4 nanoparticles are not firmly attached to graphene sheet. Poor adhesion between Fe_3O_4 and graphene is a major concern for any realistic applications. In an effort, Li et. al. synthesized Fe_3O_4 decorated graphene oxide sheets by adding graphene oxide in solution containing $FeCl_3.6H_2O$ and $FeSO_4.7H_2O$ under N_2 at 80 °C [29]. However, the method has a crucial and difficult step of adjusting the pH of the reaction to 10, throughout the course of the reaction. In yet another attempt, Gan et. al. synthesized Fe_3O_4-(poly(diallyldimethyl ammonium chloride) (PDDA)) core-shell structured nanoparticles and graphene oxide-DNA composite first. In next step both composites were attached together by sol-gel technique. But while doing the synthesis of Fe_3O_4 nanoparticles, $FeCl_3 \cdot 6H_2O$ and sodium acetate were dissolved in ethylene glycol and obtained solution was heated at 200˚C for 8 hours. This kind of method needs long time reaction and high temperature. Also mean Fe_3O_4 particle size was 300 nm [29].

Magnetic Fe_3O_4 nanoparticles are of interest to us for their possible applications in cancer hyperthermia treatment. Synthesis of monodisperse, small size (less than 10 nm), shape and size controlled, reproducible and of single phase (without contaminations by other iron oxide phases such as FeO, Fe_2O_3, etc) was a challenge. We developed a method for synthesis of Fe_3O_4 nanoparticles and addressed listed challenges. Fe_3O_4 nanoparticles are synthesized on carboxylic group functionalized graphene in presence of $Fe(acac)_3$, ascorbic acid, dehydrated ethanol and ultrapure water. In our method, $Fe(acac)_3$ was reduced by ascorbic acid and hydrolyzed by ultrapure water in presence of surface functionalized graphene for deposition of Fe_3O_4 nanoparticles on graphene. –COOH moieties present on surface functionalized graphene provides attachment site for Fe_3O_4 nanoparticles [30, 31]. The reaction parameters are optimized to obtain monodisperse Fe_3O_4 spherical nanoparticles of 10 nm diameter deposited on surface functionalized graphene sheet. Synthesized nanocomposite is characterized by various physico-chemical characterization techniques and results are reported here.

4.2 Materials and method

Graphene, functionalized graphene and graphene-Fe_3O_4 samples were characterized by X-ray powder diffraction (XRD), Scanning Electron Microscopy and EDAX analysis, Transmission electron microscopy (TEM), X-ray photoelectron spectroscopy (XPS) and Raman Spectroscopy was also performed using Renishaw InVia Raman Microscope (Japan). The chemical characterization of functional groups on surface of the all samples was studied by a Fourier transform infrared spectrometer in the range 4000 cm^{-1} - 450 cm^{-1}.

Graphene is functionalized with carboxylic group by interaction with H_2SO_4 and HNO_3 mixture, followed by filtration, washing with ultrapure water and drying at room temperature and at 60 °C.

Surface functionalized graphene (0.1 gm) was added in 50 mL of 30 mM $Fe(acac)_3$ diphenyl-ether solution made (by dissolving $Fe(acac)_3$ in diphenyl-ether) and the solution was kept under stirring in N_2 gas atmosphere. Temperature was increased up to various temperatures 60 °C, 70 °C, 80 °C. Ascrobic acid solution of 0.025 M in 12 M ultrapure water and dehydrated ethanol was then added at a dropping rate of 2 mL/min when solution temperature reached to 70 °C. After the addition of reducing acid solution, the reaction mixture was heated to 190 °C again and refluxed for 1 hour. Finally, it was cooled down to room temperature naturally. Product was separated by filtration and washed 4 - 5 times by chloroform to remove any impurities, followed by dried in vacuum. Dry powder obtained is subsequently used for physico-chemical characterization.

4.3 Results and discussion

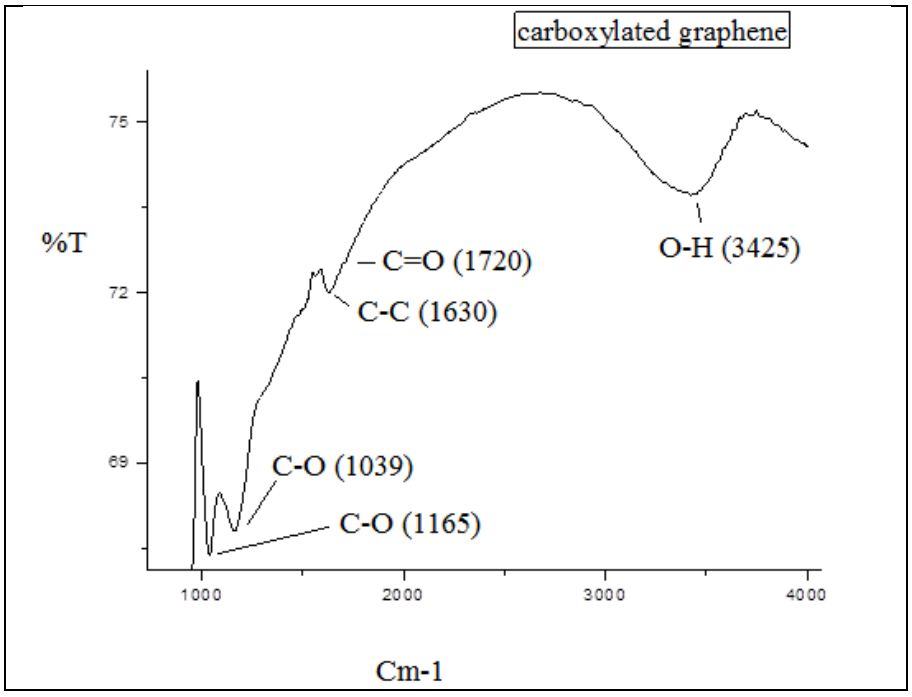

Figure 4.3.1 FTIR spectrum of carboxylated graphene. [$Fe(acac)_3$] = 30mmol/L (V = 50 mL), Reducing acid solution containing [ascorbic acid] = 25 mmol/L, [water] = 12 mol/L, Dropping rate: 2 mL/min, Volume of the reducing solution: 10 mL.

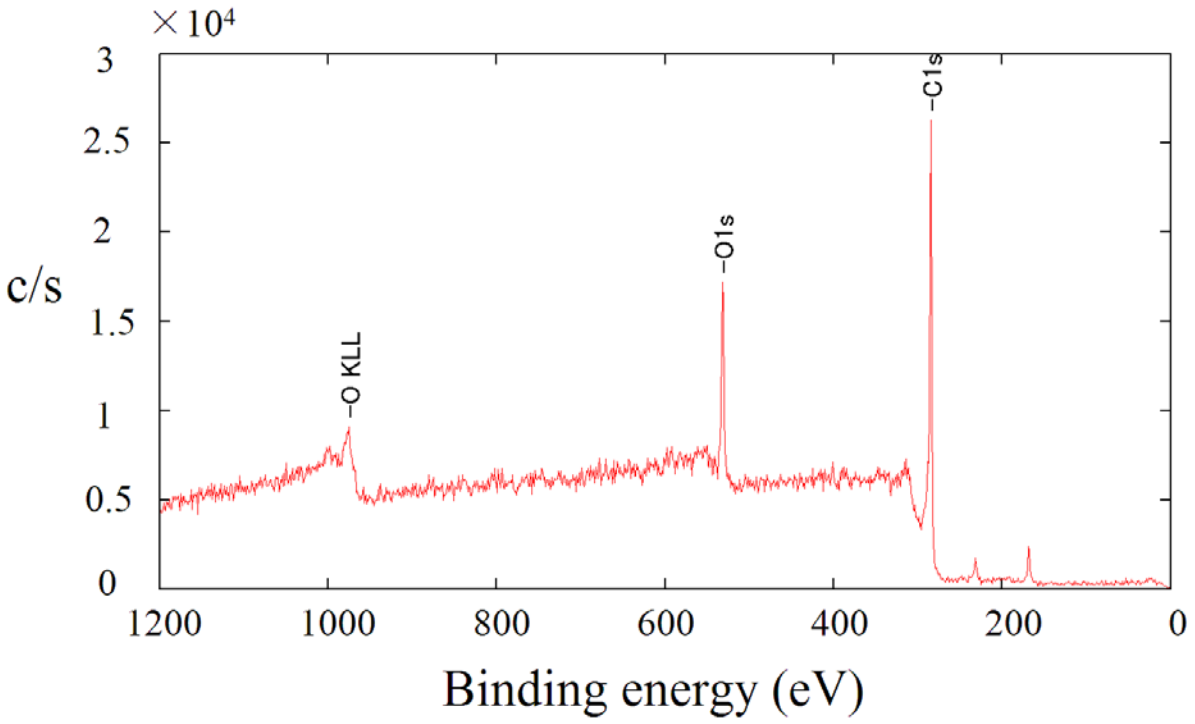

Figure 4.3.2 XPS survey or full scan spectrum of carboxylated graphene. [$Fe(acac)_3$] = 30mmol/L (V = 50 mL), Reducing acid solution containing [ascorbic acid] = 25 mmol/L, [water] = 12 mol/L, Dropping rate: 2 mL/min, Volume of the reducing solution: 10 mL.

During the synthesis process, $Fe(acac)_3$ is reduced by ascorbic acid and hydrolyzed by ultrapure water. Ascorbic acid acts as reducing agent and ultrapure water acts as oxygen supplier. When this reaction occurs in presence of carboxylated graphene, the –COOH moieties provide anchoring site for Fe_3O_4 nanoparticles and graphene-Fe_3O_4 nanocomposite is synthesized. In first step Fe ions (Fe^{2+} and Fe^{3+}) get anchored on oxygen containing groups (-COO-) present on graphene sheets. In second step, Fe_3O_4 nanoparticles are generated through heating process in which oxygen is supplied by ultrapure water and Fe-ions gets reduced. The overall reaction for Fe_3O_4 formation is as follows:

$$6\ Fe(acac)_3 + C_6H_8O_6 + 8\ H_2O \longrightarrow 2\ Fe_3O_4 + C_6H_6O_6 + 18\ (acac)$$

Figure 4.3.1 shows the Fourier transform infra-red spectroscopy (FTIR) spectrum of carboxylated graphene. It can be observed that after carboxylation process, C=O stretching vibration was observed at 1710 cm^{-1}. Peaks at 3425 cm^{-1}, 1630 cm^{-1}, 1039 cm^{-1}, 1165 cm^{-1} are due to O-H vibrations, C=C vibrations, C-O vibrations and C-O vibrations, respectively. In order to understand the chemical structure of carboxylated graphene, X-ray photoelectron spectroscopy (XPS) study was performed.

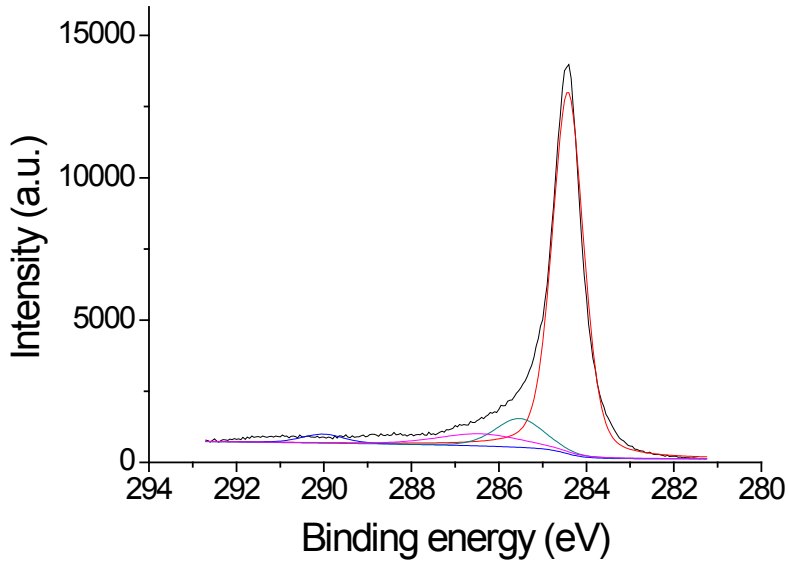

(a)

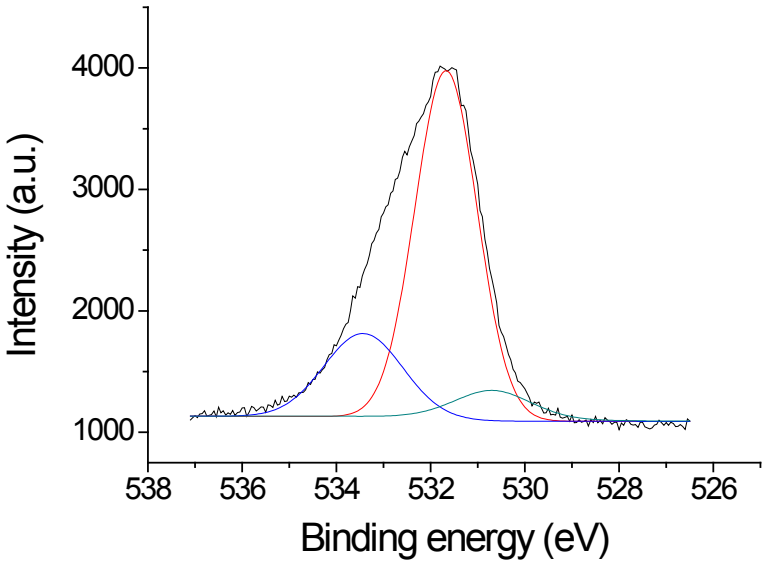

(b)

Figure 4.3.3 (a) XPS - C1s spectra of carboxylated graphene, (b) XPS-O1s spetra of carboxylated graphene. [$Fe(acac)_3$] = 30mmol/L (V = 50 mL), Reducing acid solution containing [ascorbic acid] = 25 mmol/L, [water] = 12 mol/L, Dropping rate: 2 mL/min, Volume of the reducing solution: 10 mL.

All obvious peaks are labeled and can be ascribed to O and C in Figure 4.3.2. In Figure 4.3.3.a shows C 1s region XPS spectrum of carboxylated graphene. C1s peak was set to 284.8eV to normalize any peak shifts. The C1s XPS spectrum contained four typical components which corresponds to binding energy peaks centered at 284.5 eV (C-C bond type bonding), 285.61

eV (C-O type bond), 286.75 eV (C=O type bond), and 290.43 eV (–COO bond). Figure (4.3.3.b) is carboxylated graphene XPS spectrum of O 1s. It can be observed that O 1s spectrum can be deconvoluted into two peaks centered at binding energy of 530.69 eV and 531.67 eV and 533.43 eV; which can be C-O type bonding and C=O bonding and carboxylated carbon (COOH). This indicated that carboxylation of graphene was successfully prepared. The data was consistent with reported data [32- 34].

Figure 4.3.4 shows the elemental composition of carboxylated graphene studied by Energy Dispersive X-ray Analysis (EDAX). Main elements found were carbon and oxygen. Gold (Au) was also detected which arises due to gold coated samples used for SEM observations.

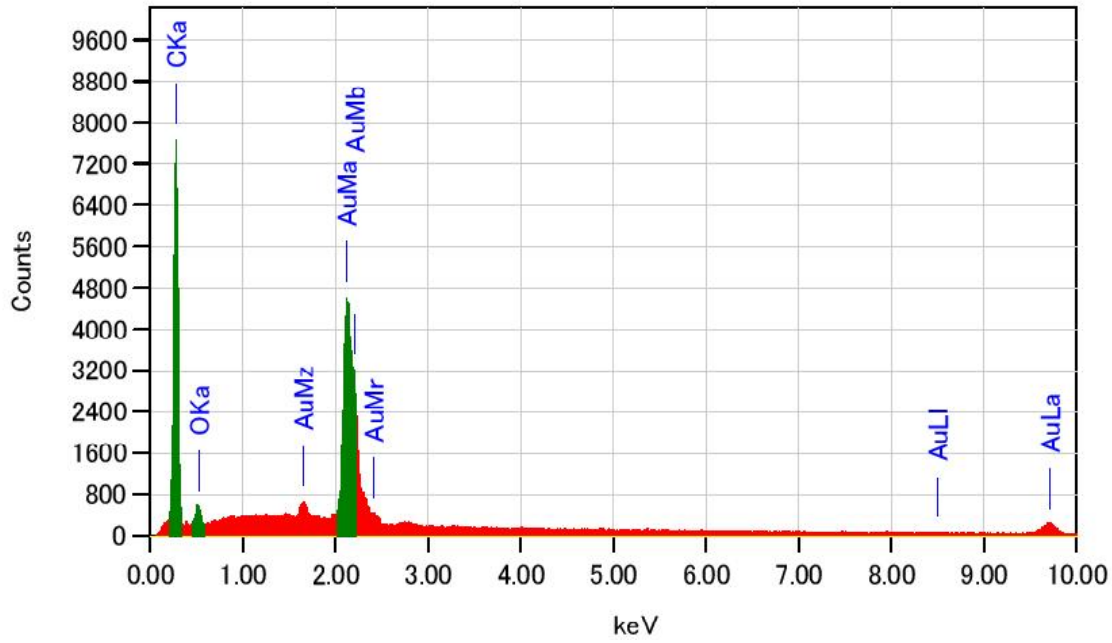

Figure 4.3.4.A EDAX spectum of carboxylated graphene. [$Fe(acac)_3$] = 30mmol/L (V = 50 mL), Reducing acid solution containing [ascorbic acid] = 25 mmol/L, [water] = 12 mol/L, Dropping rate: 2 mL/min, Volume of the reducing solution: 10 mL.

Table 4.3.4.B The atomic weight (%) of each element in carboxylated graphene

Element	atomic weight %
C (carbon)	92.40
O (Oxygen)	4.27
Au (Gold)	3.33

Figure (4.3.5.a) represents SEM image of carboxylated graphene. Figure (4.3.5.b) shows the transmission electron microscopy (TEM) image of carboxylated graphene in which carboxylated graphene sheets consisting of layers stacked eah other with less wrinkles and

foldings. Figure (4.3.5.c) is the high resolution transmission electron microscopy (HRTEM) image of carboxylated graphene sheet showing the lattice fringes.

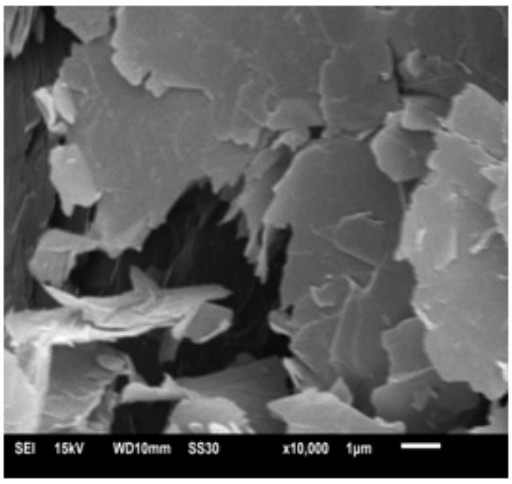

(a)

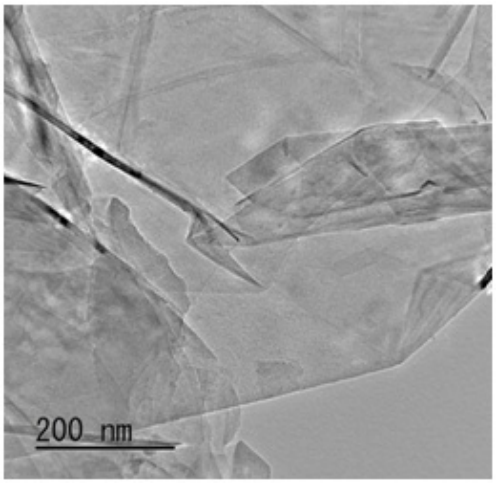

(b)

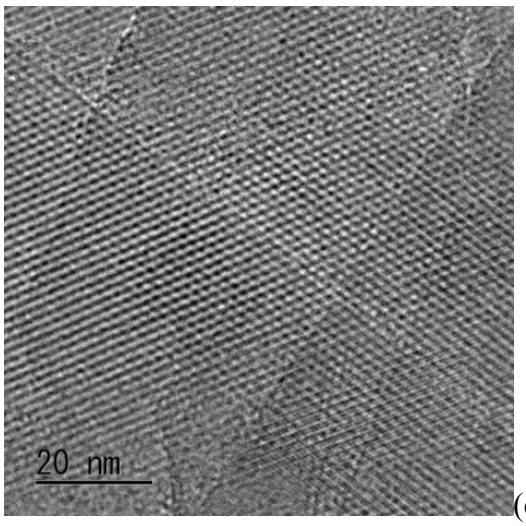

(c)

Figure 4.3.5 (a) SEM image of carboxylated graphene, (b) TEM image of carboxylated graphene and (c) HRTEM image of carboxylated graphene. [$Fe(acac)_3$] = 30mmol/L (V = 50 mL), Reducing acid solution containing [ascorbic acid] = 25 mmol/L, [water] = 12 mol/L, Dropping rate: 2 mL/min, Volume of the reducing solution: 10 mL.

All obvious peaks in Figure 4.3.6 are labeled and can be ascribed to Fe, O, and C. Figure 4.3.7 shows the XPS spectrum of Fe 2p region for Fe_3O_4 nanoparticles in graphene-Fe_3O_4 nanocomposite. The Fe 2p spectrum can be deconvoluted into five peaks at 710.29 eV, 711 eV, 719.06 eV, 722.90 eV, and 724.70 eV. Photoelectron peak at binding energy of 724.70 eV corresponds to $2p_{1/2}$ of Fe^{3+} ion; the peak at binding energy of 722.90 eV can be assigned to$2p_{1/2}$ of Fe^{2+} ions. The peaks at 710.29 eV and 711 eV can be assigned to $2p_{3/2}$ of Fe^{2+} and Fe^{3+} ions. The peak at 719.06 eV is a satellite peak for above four peaks [34].

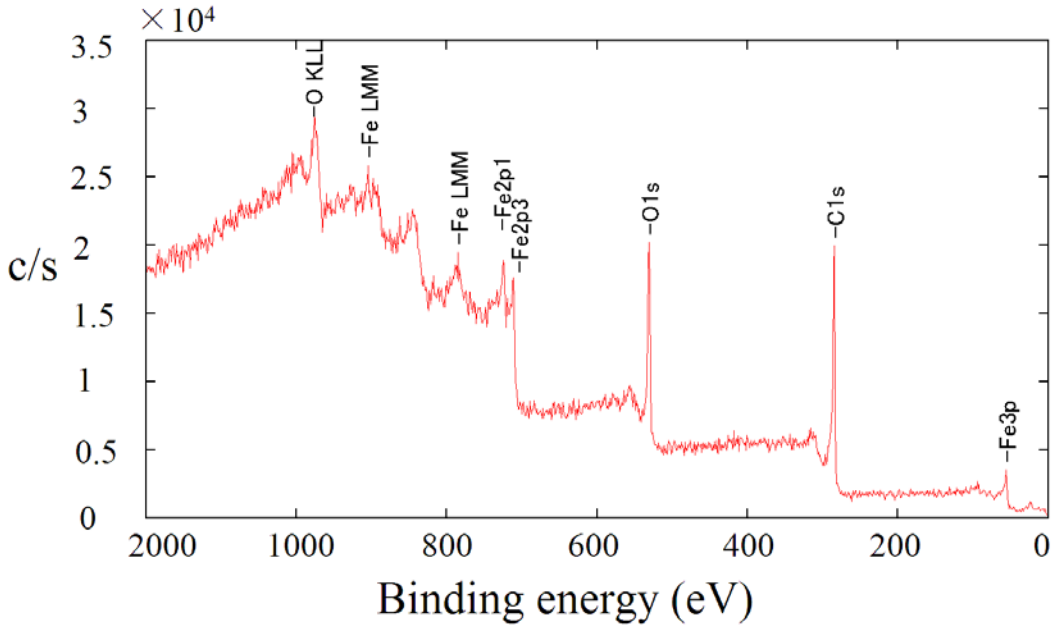

Figure 4.3.6 XPS survey or full scan spectrum of graphene-Fe_3O_4 nanocomposite. [$Fe(acac)_3$] = 30mmol/L (V = 50 mL), Reducing acid solution containing [ascorbic acid] = 25 mmol/L, [water] = 12 mol/L, Dropping rate: 2 mL/min, Volume of the reducing solution: 10 mL.

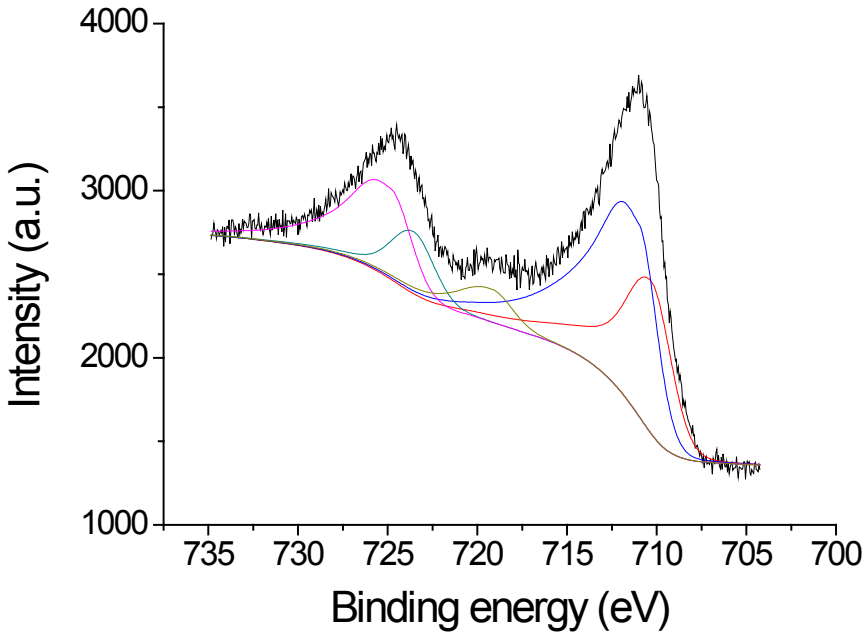

Figure 4.3.7 XPS of Fe2p region for Fe_3O_4 nanoparticles in graphene-Fe_3O_4 nanocomposite. [$Fe(acac)_3$] = 30mmol/L (V = 50 mL), Reducing acid solution containing [ascorbic acid] = 25 mmol/L, [water] = 12 mol/L, Dropping rate: 2 mL/min, Volume of the reducing solution: 10 mL.

Figure 4.3.8 represents XPS spectra of as synthesized graphene-Fe_3O_4 nanocomposite. C1s peak was set to 284.8eV to normalize any peak shifts. The C 1s spectrum (Figure 4.3.8.a) can be deconvoluted into three main peaks at 284.42 eV, 288.43 eV and 285.33 eV attributable to C-C type bond, C-O type bond and C=O type bonding, respectively. O 1s spectrum (Figure 4.3.8.b) can be deconvoluted into three peaks centered at 531.10 eV, 532.43 eV and 530.04 eV attributable to Fe-O-C bond, C-O bond and Fe-O bond, respectively. The Fe-O-C linkage suggests interfacial interaction between Fe_3O_4 and graphene and ensured the strong interaction, structural stability of graphene-Fe_3O_4 nanocomposite. The results were consistent with reported data [35].

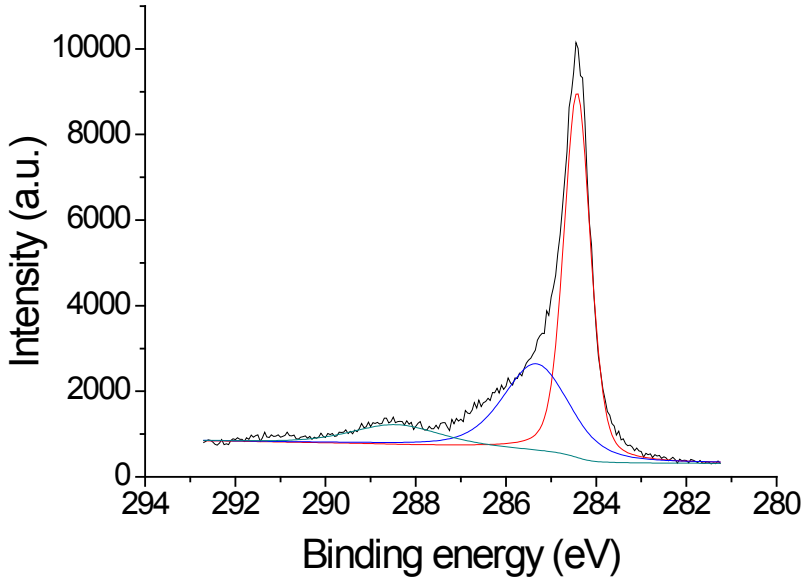

(a)

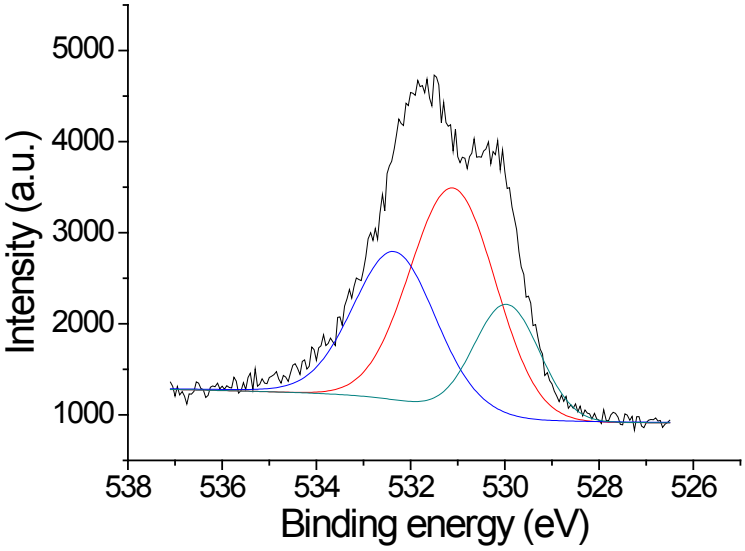

(b)

Figure 4.3.8 XPS spectrum of Graphene-Fe_3O_4 nanocomposite.
(a) C 1s spectrum and (b) O 1s spectrum.
[$Fe(acac)_3$] = 30mmol/L (V = 50 mL), Reducing acid solution containing [ascorbic acid] = 25 mmol/L, [water] = 12 mol/L, Dropping rate: 2 mL/min, Volume of the reducing solution: 10 mL.

Size, shape and morphology of graphene-Fe_3O_4 nanocomposite and bare Fe_3O_4 nanoparticles were characterized by SEM and TEM. Figure (4.3.9a and 4.3.9b) represents TEM images of graphene-Fe_3O_4 nanocomposite. It is evident that the two-dimensional graphene sheets are decorated by Fe_3O_4 nanoparticles. Average size of Fe_3O_4 nanoparticles was found to be 10 nm. Aggregation of Fe_3O_4 nanoparticles was not observed on graphene sheet. While making the samples for TEM analysis, even after vigorous ultrasonication, Fe_3O_4 nanoparticles were firmly attached on graphene sheets indicating strong interaction between the two. Figure (4.3.9c and 4.3.9d) shows SEM image of graphene-Fe_3O_4 nanocomposite. It is observable that Fe_3O_4 nanoparticles are distributed over graphene sheet. For comparison, SEM and TEM images of Fe_3O_4 nanoparticles synthesized separately (without using graphene) are displayed in Figure (4.3.9e and 4.3.9f). Fe_3O_4 nanoparticles of the same size of about 10 nm were obtained. However, aggregation of Fe_3O_4 nanoparticles is observable.

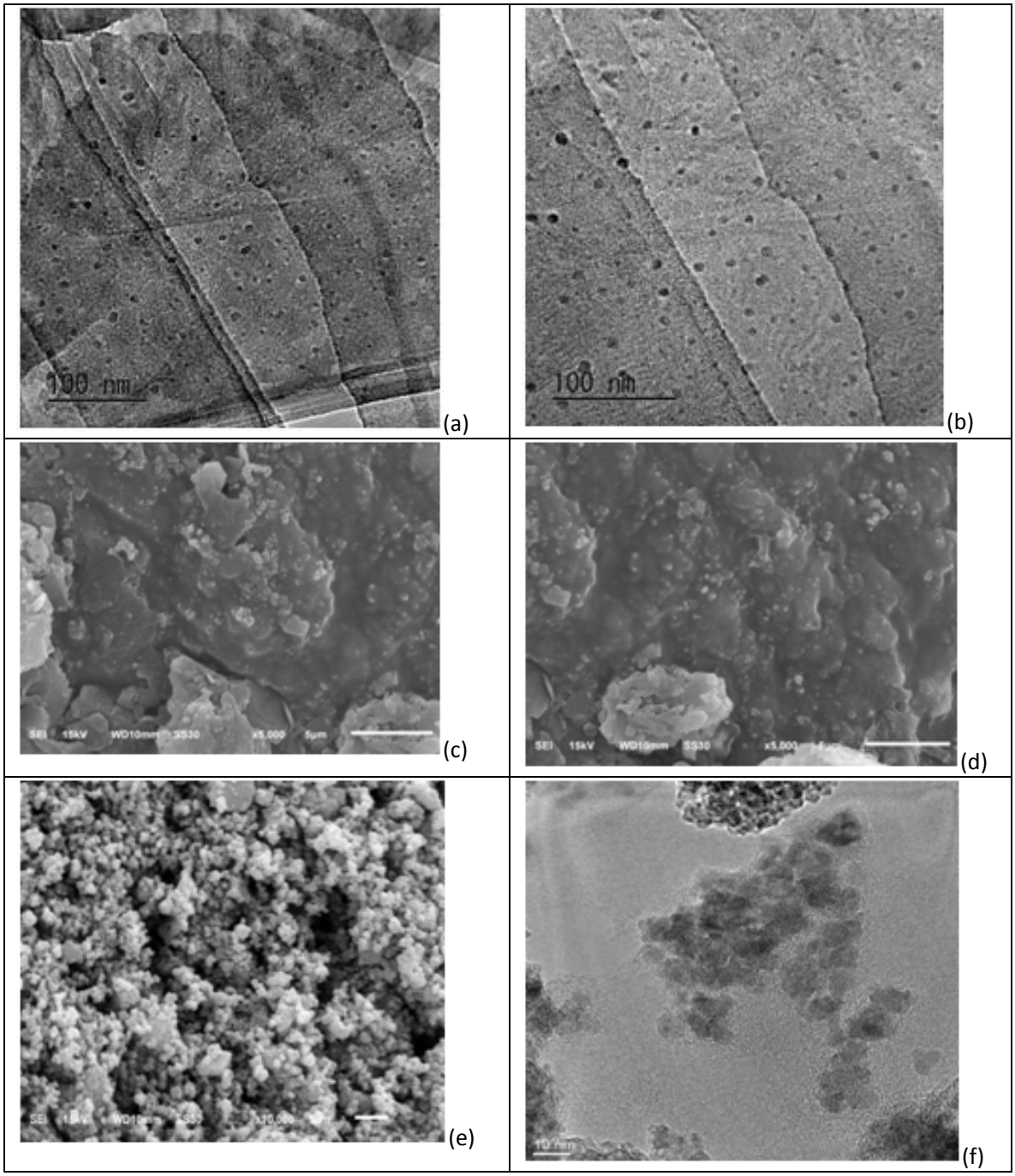

Figure 4.3.9 (a, b) TEM images of graphene-Fe_3O_4 nanocomposite, (c, d) SEM images of graphene-Fe_3O_4 nanocomposite, (e and f) SEM and TEM image of bare Fe_3O_4 nanoparticles. [$Fe(acac)_3$] = 30mmol/L (V = 50 mL), Reducing acid solution containing [ascorbic acid] = 25 mmol/L, [water] = 12 mol/L, Dropping rate: 2 mL/min, Volume of the reducing solution: 10 mL.

Figure 4.3.10.A represents the EDAX spectrum of graphene-Fe_3O_4 nanocomposite. Major elements found are: carbon, oxygen, iron, and gold (which arises due to the fact that the samples

were coated with gold for SEM observations).

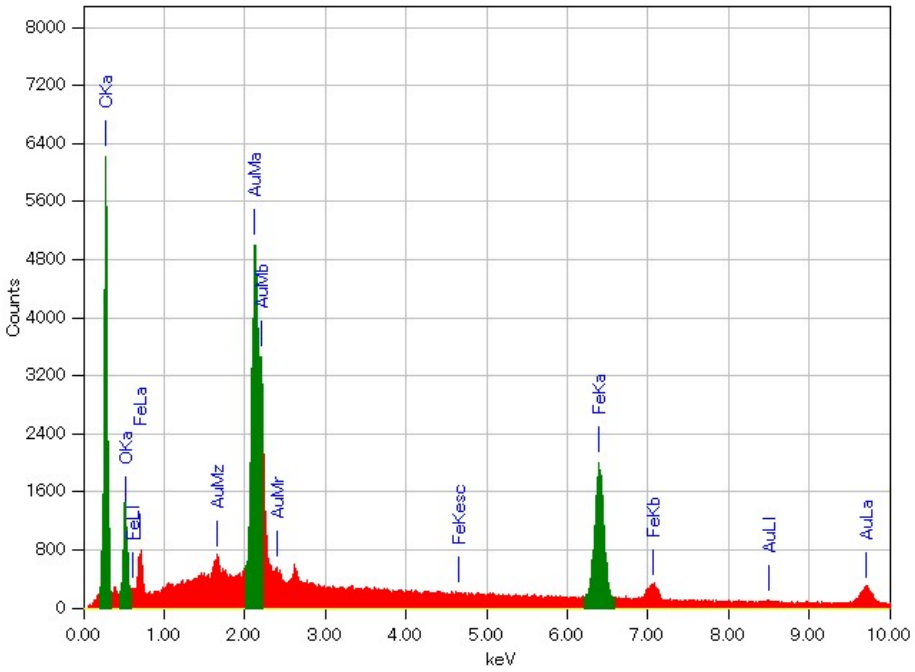

Figure 4.3.10.A EDAX spectrum of graphene-Fe_3O_4 nanocomposite. [$Fe(acac)_3$] = 30mmol/L (V = 50 mL), Reducing acid solution containing [ascorbic acid] = 25 mmol/L, [water] = 12 mol/L, Dropping rate: 2 mL/min, Volume of the reducing solution: 10 mL.

Table 4.3.10.B The atomic weight % of each element in graphene-Fe_3O_4 nanocomposite.

Element	Atomic weight (%)
C (carbon)	76.94
O (Oxygen)	9.39
Fe (Iron)	10.32
Au (Gold)	3.35

Figure 4.3.11 represents Raman spectra of graphene (Figure 4.3.11a) and graphene-Fe_3O_4 nanocomposite (Figure 4.3.11b). Raman spectrum of graphene exhibits G-band at 1580 cm^{-1}, D-band at 1350 cm^{-1} and 2D band at 2717 cm^{-1}. Raman spectrum of graphene-Fe_3O_4 nanocomposite shows G-band at 1581 cm^{-1}, D-band at 1352 cm^{-1} and 2D band at 2717 cm^{-1} which is similar to Raman spectra of graphene. D and G bands are corresponding to sp^3-hybridized carbon and sp^2-hybridized carbon [34]. It is observed that I_D/I_G ratio of graphene-Fe_3O_4 (0.97) nanocomposite was greater than I_D/I_G ratio of graphene (0.51) which indicates the presence of some unrepaired defects and interaction between Fe_3O_4 and graphene. This is consistent with earlier observations by other researchers [37, 38].

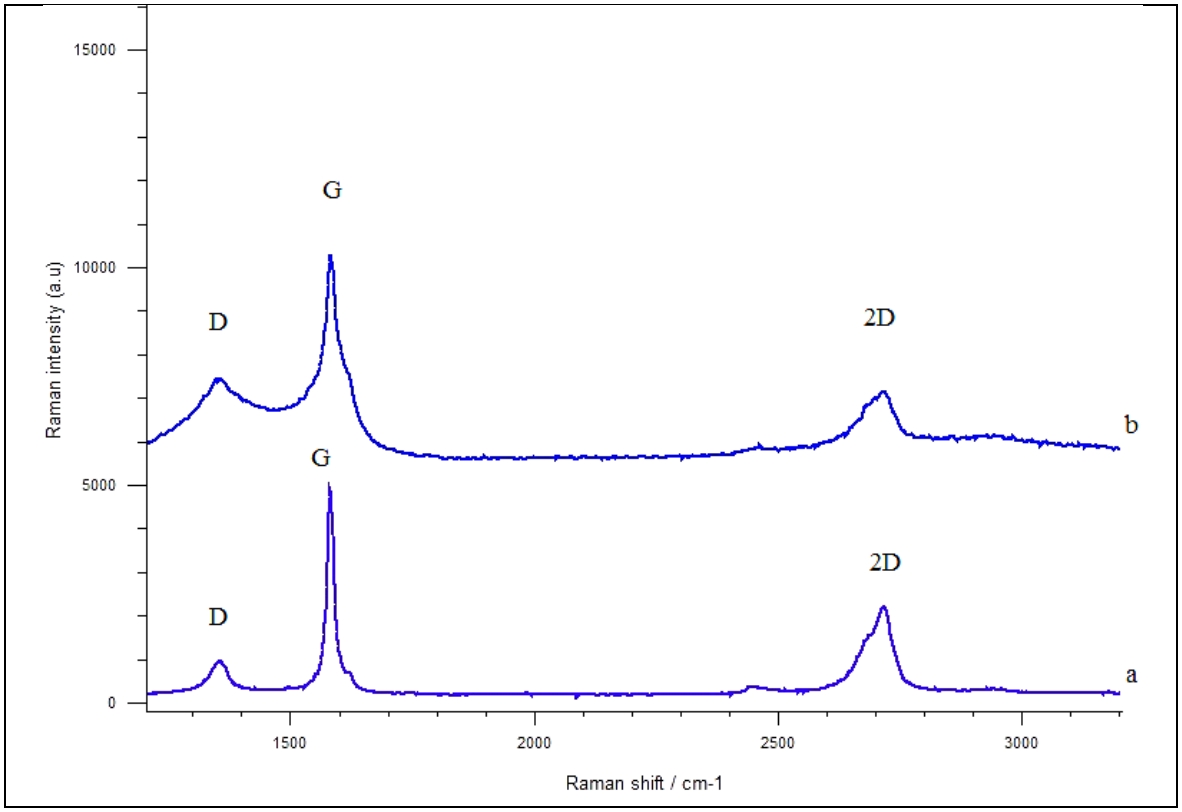

Figure 4.3.11 Raman spectra (a) graphene and (b) graphene-Fe_3O_4 nanocomposite. [$Fe(acac)_3$] = 30mmol/L (V = 50 mL), Reducing acid solution containing [ascorbic acid] = 25 mmol/L, [water] = 12 mol/L, Dropping rate: 2 mL/min, Volume of the reducing solution: 10 mL.

4.4 Concluding remarks

A new method to synthesize graphene-Fe_3O_4 nanocomposite is developed. Graphene functionalized with carboxylic group was added during the chemical synthesis of Fe_3O_4 nanoparticles by reduction of $Fe(acac)_3$ using ascorbic acid to get Graphene-Fe_3O_4 nanocomposite, wherein the monodisperse spherical nanoparticles of Fe_3O_4 of 10 nm diameter remains attached to graphene surface. Physico-chemical characterization of the synthesized nanocomposite is done using scanning electron microscopy, transmission electron microscopy, X-ray diffraction, X-ray photoelectron spectroscopy, Raman and Fourier Transform Infra-red spectroscopy in order to understand different physico-chemical parameters and properties of the synthesized material. TEM shows that Fe_3O_4 nanoparticles of about 10 nm diameter were decorated on graphene. FTIR and XPS confirm the carboxylation or surface functionalization of graphene. XPS also confirms formation of Fe_3O_4 nanoparticles and chemical bond between graphene and Fe_3O_4 nanoparticles. Method presented herewith should prove to be useful for synthesis of graphene-Fe_3O_4 nanocomposite for application in cancer hyperthermia. Further uploading of drug molecules on the graphene-Fe_3O_4 nanocomposite should be possible for

applications in biomedical science.

References:

1. "The 2010 Nobel Prize in Physics - Press Release". Nobelprize.org. Nobel Media AB 2014. Web. 11 Nov 2016. http://www.nobelprize.org/nobel_prizes/physics/laureates/2010/press.html
2. Spyrou, K. and Rudolf, P. (2014) An Introduction to Graphene, in Functionalization Of Graphene (ed V. Georgakilas), Wiley-VCH Verlag GmbH & Co. KGaA, Weinheim, Germany. Doi: 10.1002/9783527672790.ch1.
3. S. Rahi, P. Rastogi, R. Kumar, Graphene: Introduction and applications in next-generation ULSI technology an overview, International Journal of Advances in Engineering & Technology. 6(4), 1535-1540, 2013.
4. T. Das, S. Prusty, Recent advances in applications of graphene, International Journal of Chemical Sciences and Applications. 4(1), 39-55, 2013.
5. K. S. Novoselov, A. K. Geim, S. V. Morozov, D. Jiang, Y. Zhang, S. V. Dubonos, I. V. Grigorieva, A. A. Firsov, Electric field effect in atomically thin carbon films, Science.306, 666-669, 2004.
6. P. Somani, S. Somani, M. Umeno, Planer nano-graphenes from camphor by CVD, Chemical Physics letters.430,56-59, 2006.
7. Y. Zhu, S. Murali, W. Cai, X. Li, J. W. Suk, J.R. Potts, R. S. Ruoff, Graphene and Graphene oxide: Synthesis, Properties and Applications, Adv. Mater. 22, 3906-3924, 2010.
8. L.X. Dong, Q. Chen, Properties, Synthesis and Characterization of Graphene, Front. Mater. Sci. China. 4(1), 45-51, 2010.
9. X. Wang, L. Zhi, K. Mullen, Transperent, Conductive Graphene Electrodes for Dye-Sensitized Solar Cells, Nano Lett.8, 323-327, 2008.
10. H. Shen, L. Zhang, M. Liu, Z. Zhang, Biomedical Applications of Graphene, Theranostics. 2(3), 283-294, 2012.
11. Y. Huang, J. Liang, Y. Chen, An overview of the Applications of Graphene-Based Materials in Supercapacitors, Small.8, 1805-1834, 2012.
12. Y. He, Q. Sheng, J. Zheng, M. Wang, B. Liu, Magnetite–graphene for the direct electrochemistry of hemoglobin and its biosensing application, Electrochimica Acta. 56, 2471–2476, 2011.
13. D. Wei, Y. Liu, Controllable Synthesis of Graphene and Its Applications, Adv. Mater. 22, 3225–3241, 2010.
14. X. Sun, Z. Liu, K. Welsher, J. T. Robinson, A. Goodwin, S. Zaric, H. Dai, Nano-Graphene Oxide for Cellular Imaging and Drug Delivery, Nano Res.1, 203 212, 2008.
15. Q. Cheng, J. Tang, J. Ma, H. Zhang, N. Shinya, L. C. Qin, Nano-Flower MnO_2 Coated

Graphene Composite Electrodes for Energy Storage Devices, Mater. Res. Soc. Symp. Proc. 1303, 129-134, 2011.

16. X. Y. Zhang, H. P. Li, X. L. Cui, Y. Lin, Graphene/TiO_2 nanocomposites: synthesis, characterization and application in hydrogen evolution from water photocatalytic splitting, J. Mater. Chem. 20, 2801–2806, 2010.
17. J. Yang, C. Tian, L. Wang , H. Fu, An effective strategy for small-sized and highly-dispersed palladium nanoparticles supported on graphene with excellent performance for formicacid oxidation, J. Mater. Chem. 21, 3384–3390, 2011.
18. X. Sun, C. Zhou, M. Xie, H. Sun, T. Hu, F. Lu, S. M. Scott, S. M. George , J. Lian, Synthesis of ZnO quantum dot/graphene nanocomposites by atomic layer deposition with high lithium storage capacity, J. Mater. Chem. A. 2, 7319–7326, 2014.
19. Y. Li, H. Wang, L. Xie, Y. Liang, G. Hong, H. Dai, MoS_2 Nanoparticles Grown on Graphene: An Advanced Catalyst for the Hydrogen Evolution Reaction, J. Am. Chem. Soc.133, 7296–7299, 2011.
20. Y. W. Liu, M. X. Guan, L. Feng, S. L. Deng, J. F. Bao, S.Y. Xie, Z. Chen, R. B. Huang, L.S. Zheng, Facile and straightforward synthesis of superparamagnetic reduced grapheneoxide–Fe_3O_4 hybrid composite by a solvothermal reaction, Nanotechnology. 24,1-10, 2013.
21. Z. Wang, J. Tang, F. Zhang, J. Xia, N. Sun, G. Shi, Y. Xia, L. Xia, L. Qin, Elimination of ascorbic acid and sensitive detection of uric acid at the MnO_2 nanorods / Graphene- based modified electrode, Int. J. Electrochem. Sci. 8, 9967 – 9976, 2013.
22. C. B. Song, Y. H. Qiang, Y. L. Zhao, X. Q. Gu, L. Zhu，J. Song, X. Liu, Dye-sensitized Solar Cells Based on Graphene-TiO_2 Nanoparticles/ TiO_2 Nanotubes Composite Films, Int. J. Electrochem. Sci. 9, 8090 - 8096, 2014.
23. P. T. Yin, S. Shah, M. Chhowalla, K. B. Lee, Design, Synthesis, and Characterization of Graphene − Nanoparticle Hybrid Materials for Bioapplications, Chem. Rev. 115, 2483−2531, 2015.
24. X. Pan, Y. Zhao, S. Wang, Z. Fan, TiO_2/graphene nanocomposite for photocatalytic application, International Journal of Hydrogen Energy.37, 2224-2230, 2012.
25. B. Li, H. Cao, J. Shao, M. Qub, J. H. Warner, Superparamagnetic Fe_3O_4 nanocrystals@ graphene composites for energy storage devices, J. Mater. Chem. 21, 5069–5075, 2011.
26. X. Ma, H. Tao, K. Yang, L. Feng, L. Cheng, X. Shi, Y. Li, L. Guo, Z. Liu, A Functionalized Graphene Oxide–Iron Oxide Nanocomposite for Magnetically Targeted Drug Delivery, Photothermal Therapy, and Magnetic Resonance Imaging, Nano Res. 5(3), 199–212, 2012.
27. P. F. Guan, X. F. Zhang, J. J. Guo, Assembled Fe_3O_4 nanoparticles on graphene for enhanced electromagnetic wave losses, Applied Physics Letters 101, 153108, 2012.
28. J. Li, S. Zhang, C. Chen, G. Zhao, X. Yang, J. Li, X. Wang, Removal of Cu(II) and fulvic acid by Graphene oxide nanosheets decorated with Fe_3O_4 nanoparticles, ACS Appl. Mater.

Interfaces. 4, 4991−5000, 2012.

29. N. Gan, J. Zhang, S. Lin, N. Long, T. Li , Y. Cao, A novel magnetic Graphene oxide composite absorbent for removing trace residues of polybrominated diphenyl ethers in water, Materials.7, 6028-6044, 2014.
30. T. T. Tung, J. F. Feller, T. Y. Kim, H. Kim, W. S. Yang, K. S. Suh, Electromagnetic Properties of Fe_3O_4 - Functionalized Graphene and its composites with a conducting polymer, Journal of Polymer Science Part A: Poymer Chemistry. 50, 927–935, 2012.
31. X. Yang, X. Zhang, Y. Ma, Y. Huang, Y. Wanga, Y. Chen, Superparamagnetic graphene oxide–Fe_3O_4 nanoparticles hybrid for controlled targeted drug carriers, J. Mater. Chem. 19, 2710–2714, 2009.
32. D. Wang, A. Du, E. Taran, G. Lu, I. Gentle, J. Mater. Chem. 22, 21085–21091, 2012.
33. L. Zhang, Y. Li, L. Zhang, D. Li, D. Karpuzov, Y. Long, Electrocatalytic oxidation of NADH on Graphene oxide and reduced Graphene oxide modified screen - printed electrode, Int. J. Electrochem. Sci, 6, 819 – 829, 2011.
34. G. Martinez, A. Malumbres, R. Mallada, J. L. Hueso, S. Irusta, O. B. Miguel, J. Santamaria,Use of a polyol liquid collection medium to obtain ultrasmall magnetic nanoparticles by laser pyrolysis, Nanotechnology. 23, 425605 (9pp), 2012.
35. C. Fu, G. Zhao, H. Zhang, S. Li,A Facile route to controllable synthesis of Fe_3O_4/Graphene composites and their application in Lithium-Ion batteries,

    Int. J. Electrochem.Sci. 9, 46 - 60, 2014.
36. S. Adhikari, M. S. Kayastha, D. C. Ghimire, H. R. Aryal, S. Adhikary, T. Takeuchi, K. Murakami, Y. Kawashimo, H. Uchida, K. Wakita, M. Umeno, Improved photovoltaic properties of heterojunction carbon based solar cell, Journal of Surface Engineered Materials and Advanced Technology.3, 178-183, 2013.
37. S. Zhu, J. Guo, J. Dong, Z. Cui, T. Lu, C. Zhu, D. Zhang, J. Ma, Sonochemical fabrication of Fe_3O_4 nanoparticles on reduced graphene oxidefor biosensors ultrasonics sonochemistry.20, 872–880, 2013.
38. P. Li, Y. Zheng, Y. Wu, P. Qu, R. Yang, N. Wang, M. Li, A nanoscale liquid-like graphene@Fe_3O_4 hybrid with excellent amphiphilicity and electronic conductivity, New J. Chem. 38, 5043-5051, 2014.

Chapter 5: Summary, Conclusion and Future Scope

This work is intended to the development of synthetic route for synthesis of Fe_3O_4 nanoparticles by ascorbic acid mediated reduction of $Fe(acac)_3$ in which size control of Fe_3O_4 nanoparticles is possible. Synthesis and size control of Fe_3O_4 nanoparticles was achieved by controlling the reaction parameters. Synthesized nanoparticles were characterized by standard scientific techniques. Relationship between the reaction parameters and particle size, composition, crystallinity was studied.

This dissertation describes motivation of this work and a brief introduction about nanotechnology, nanobiotechnology, nanomaterials, nanoparticles, Types of nanoparticles, applications of nanoparticles, different synthesis methods for nanoparticles their merits and demerits, properties of magnetite (Fe_3O_4), applications of nanoparticles. It also represents a brief study on synthesis of Fe_3O_4 nanoparticles by different methods and different Fe_3O_4 nanoparticle synthesis mechanisms.

The synthesis of Fe_3O_4 nanoparticles at different reaction parameters was carried out and characterization techniques used for characterizing Fe_3O_4 nanoparticles are represented. Synthesis procedures at different reaction parameters for estimating decomposition efficiency and synthesis of Fe_3O_4 nanoparticles are explained. Synthesis and mechanism of Fe_3O_4 formation by ascorbic acid mediated reduction of $Fe(acac)_3$ is described. Decomposition efficiency of $Fe(acac)_3$, Synthesis of Fe_3O_4 nanoparticles by ascorbic acid mediated reduction of $Fe(acac)_3$ and effect of various reaction parameters on nanoparticle diameter and crystallinity have been studied. Decomposition efficiency of $Fe(acac)_3$ was estimated at different addition temperatures and ultrapure water concentrations. Decomposition efficiency (%) of $Fe(acac)_3$ increases with respect to increase in addition temperature, this may be due to rate of reaction increases as addition temperature increases. It was also observed that decomposition efficiency increases with respect to time showing that precursor gets reduced by ascorbic acid. There was no significant effect of ultrapure water concentration changes on decomposition efficiency. At 60 °C, after 25 minutes decomposition efficiency was found to be 33.57%, indicating 1/3 reduction of precursor $Fe(acac)_3$ by ascorbic acid. When reactants were added in stoichiometric ratio the decomposition efficiency of $Fe(acac)_3$ after the completion of reaction was in the range of 90-100%, shows that almost all precursor was utilized in reaction.

Effect of addition temperature on Fe_3O_4 nanoparticle diameter: It was observed that magnetite (Fe_3O_4) can be synthesized when addition of reducing acid solution was carried out at room temperature but the sample was largely aggregated. Fe_3O_4 nanoparticles having size 29±9 nm were synthesized at addition temperature of 60 °C. Fe_3O_4 nanoparticles with diameter 33±3 nm and 42±5 nm were successfully synthesized at 1.2 M ultrapure water concentration and addition temperature of 70 °C and 80 °C respectively. At 1.2 M ultrapure water concentration

Fe_3O_4 nanoparticle size increases with increase in addition temperature.

Effect of ultrapure water concentration on Fe_3O_4 nanoparticle diameter: Fe_3O_4 nanoparticles having diameter 22±6 nm and 8±2 nm were successfully synthesized at addition temperature of 60 °C, 80 °C and at 12 M ultrapure water. Fe_3O_4 nanoparticle size decreases with increase in ultrapure water concentration.

Size controlled synthesis of Fe_3O_4 nanoparticles having diameter 15±4 nm was successfully carried out at 12 M ultrapure water concentration and at addition temperature of 70 °C. Reaction parameters were optimized to synthesize size controlled Fe_3O_4 nanoparticles with diameter 15 ± 4 nm. At addition temperature of 70 °C Fe_3O_4 nanoparticle size decreases with increase in ultrapure water concentration.

Ascorbic acid mediated reduction of $Fe(acac)_3$ was also carried out in absence of ultrapure water (0 M water). Fe_3O_4 nanoparticles are observed to form with addition of water; whereas Fe/iron oxide nanoparticles are formed in absence of water. It was observed that such Fe nanoparticles get oxidized to form Fe/iron oxide nanoparticles due to exposure to air atmosphere. Reproducible synthesis of Fe/iron oxide nanoparticles having size 7 ± 1 nm was achieved.

Effect of $Fe(acac)_3$ concentration on Fe_3O_4 nanoparticle diameter: Fe_3O_4 nanoparticles with diameter 9±1 nm and 108±21 nm were synthesized at 50 mM and 15 mM $Fe(acac)_3$ concentrations respectively. Results show that Fe_3O_4 nanoparticle size decreases with increase in $Fe(acac)_3$ concentration and size increases with decrease in $Fe(acac)_3$ concentration.

Effect of ascorbic acid concentration on Fe_3O_4 nanoparticle diameter: Fe_3O_4 nanoparticles having diameter 9±3 nm and 76±29 nm were synthesized at 0.05 M and 0.005 M ascorbic acid concentration. At addition temperature of 70 °C nanoparticle size is inversely proportional to the concentration of ascorbic acid.

Effect of dropping rate on Fe_3O_4 nanoparticle diameter: Fe_3O_4 nanoparticles having diameter 8±2 nm and 23±5 nm were synthesized at 1 mL/min and 3 mL/min dropping rate. At 70 °C Fe_3O_4 nanoparticle size is directly proportional to dropping rate of ascorbic acid solution.

A new method developed to synthesize graphene-Fe_3O_4 nanocomposite is developed. Graphene functionalized with carboxylic group was added during the chemical synthesis of Fe_3O_4 nanoparticles by reduction of $Fe(acac)_3$ using ascorbic acid to get Graphene-Fe_3O_4 nanocomposite, wherein the monodisperse spherical nanoparticles of Fe_3O_4 of 10 nm diameter

remains attached to graphene surface. TEM shows that Fe_3O_4 nanoparticles of about 10 nm diameter were decorated on graphene. FTIR and XPS confirm the carboxylation or surface functionalization of graphene. XPS also confirms formation of Fe_3O_4 nanoparticles and chemical bond between graphene and Fe_3O_4 nanoparticles. Method presented herewith should prove to be useful for synthesis of graphene-Fe_3O_4 nanocomposite for application in cancer hyperthermia.

This work may provide solution for the problems related to synthesis of Fe_3O_4 nanoparticles such as size control and reproducibility with much clearer Fe_3O_4 formation mechanism. The efforts presented in this work may be one of the pronounced references in the future researches in the field of magnetite nanoparticle synthesis. Method presented herewith should prove to be very useful for synthesis of Fe_3O_4 nanoparticles, having surface available for further use such as uploading of drug molecules for bio-medical applications. This research in future can be oriented in different directions such as: (a) scaling up this synthesis method, (b) study of magnetic properties of Fe_3O_4 nanoparticles synthesized by ascorbic acid mediated reduction of $Fe(acac)_3$ and (c) applications in cancer hyperthermia.

Table index

Figure index

Volume of the reducing solution: 10 mL.

22. **Figure 3.1.3.C** UV-visible spectra of samples taken at different time interval and when addition carried out at 80 °C. [$Fe(acac)_3$] = 30mmol/L (V = 50 mL), Reducing acid solution containing [ascorbic acid] = 25 mmol/L, [water] = 2.4 mol/L, Dropping rate: 2 mL/min, Volume of the reducing solution: 10 mL.
23. **Figure 3.1.3.G** Final decomposition efficiency of $Fe(acac)_3$ after reaction completion at different addition temperature at 60 °C (a), at 70 °C (b), at 80 °C (c). [$Fe(acac)_3$] = 30mmol/L (V = 50 mL), Reducing acid solution containing [ascorbic acid] = 25 mmol/L, [water] = 2.4 mol/L, Dropping rate: 2 mL/min, Volume of the reducing solution: 10 mL.
24. **Figure 3.1.3.H** UV-visible spectra of samples taken at different time interval and when addition carried out at 60 °C. [$Fe(acac)_3$] = 30mmol/L (V = 50 mL), Reducing acid solution containing [ascorbic acid] = 25 mmol/L, [water] = 12 mol/L, Dropping rate: 2 mL/min, Volume of the reducing solution: 10 mL.
25. **Figure 3.1.3.I** UV-visible spectra of samples taken at different time interval and when addition carried out at 70 °C. [$Fe(acac)_3$] = 30mmol/L (V = 50 mL), Reducing acid solution containing [ascorbic acid] = 25 mmol/L, [water] = 12 mol/L, Dropping rate: 2 mL/min, Volume of the reducing solution: 10 mL.
26. **Figure 3.1.3.J** UV-visible spectra of samples taken at different time interval and when addition carried out at 80 °C. [$Fe(acac)_3$] = 30mmol/L (V = 50 mL), Reducing acid solution containing [ascorbic acid] = 25 mmol/L, [water] = 12 mol/L, Dropping rate: 2 mL/min, Volume of the reducing solution: 10 mL.
27. **Figure 3.1.3.M** Comparison between decomposition efficiency of $Fe(acac)_3$ (%) at different addition temperature and at different ultrapure water concentration.
28. **Figure 3.1.3.N** Final decomposition efficiency of $Fe(acac)_3$ after reaction completion at different addition temperature at 60 °C (a), at 70 °C (b), at 80 °C (c). [$Fe(aca)_3$] = 30mmol/L (V = 50 mL), Reducing acid solution containing [ascorbic acid] = 25 mmol/L, [water] = 12 mol/L, Dropping rate: 2 mL/min, Volume of the reducing solution: 10 mL.
29. **Figure 3.2.1.A** XRD pattern of sample prepared when addition done at room temperature (Sample A), addition done at 60°C (Sample B). [$Fe(acac)_3$] = 30mmol/L (V = 50 mL), Reducing acid solution containing [ascorbic acid] = 25 mmol/L, [water] = 1.2 mol/L, Dropping rate: 2 mL/min, Volume of the reducing solution: 10 mL.
30. **Figure 3.2.1.B** EDAX pattern of sample prepared when addition done at room temperature (23°C), (Sample A). [$Fe(acac)_3$] = 30mmol/L (V = 50 mL), Reducing acid solution containing [ascorbic acid] = 25 mmol/L, [water] = 1.2 mol/L, Dropping rate: 2 mL/min, Volume of the reducing solution: 10 mL.
31. **Figure 3.2.1.C** EDAX pattern of sample prepared when addition done at 60°C (sample B). [$Fe(acac)_3$] = 30mmol/L (V = 50 mL), Reducing acid solution containing [ascorbic acid] = 25 mmol/L, [water] = 1.2 mol/L, Dropping rate: 2 mL/min, Volume of the reducing

solution: 10 mL.

32. **Figure 3.2.1.D** HRTEM images of samples synthesized at 1.2M ultrapure water, addition at room temperature (a, b), ataddition temperature of 60 °C with particle diameter distribution histogram (c). [$Fe(acac)_3$] = 30mmol/L (V = 50 mL), Reducing acid solution containing [ascorbic acid] = 25 mmol/L, [water] = 1.2 mol/L, Dropping rate: 2 mL/min, Volume of the reducing solution: 10 mL.
33. **Figure 3.2.1.E** XRD pattern of sample prepared when addition done at 70 °C (Sample a), addition done at 80 °C (Sample b). [$Fe(acac)_3$] = 30mmol/L (V = 50 mL), Reducing acid solution containing [ascorbic acid] = 25 mmol/L, [water] = 1.2 mol/L, Dropping rate: 2 mL/min, Volume of the reducing solution: 10 mL.
34. **Figure 3.2.1.F** EDAX spectrum of sample prepared when addition done at 70 °C (sample a). [$Fe(acac)_3$] = 30mmol/L (V = 50 mL), Reducing acid solution containing [ascorbic acid] = 25 mmol/L, [water] = 1.2 mol/L, Dropping rate: 2 mL/min, Volume of the reducing solution: 10 mL.
35. **Figure 3.2.1.G** EDAXspectrum of sample prepared when addition done at 80°C (sample b). [$Fe(acac)_3$] = 30mmol/L (V = 50 mL), Reducing acid solution containing [ascorbic acid] = 25 mmol/L, [water] = 1.2 mol/L, Dropping rate: 2 mL/min, Volume of the reducing solution: 10 mL.
36. **Figure 3.2.1.H** HRTEM images and particle diameter distribution histogram of nanoparticles prepared at 1.2M ultrapure water concentration: TEM (a) image of nanoparticles at addition temperature 70 °C and TEM (b) image of sample at addition temperature 80 °C. [$Fe(acac)_3$] = 30mmol/L (V = 50 mL), Reducing acid solution containing [ascorbic acid] = 25 mmol/L, [water] = 1.2 mol/L, Dropping rate: 2 mL/min, Volume of the reducing solution: 10 mL.
37. **Figure 3.2.2.A** XRD pattern of sample prepared when addition done at 60 °C (a), addition done at 80 °C(b). [$Fe(acac)_3$] = 30mmol/L (V = 50 mL), Reducing acid solution containing [ascorbic acid] = 25 mmol/L, [water] = 12 mol/L, Dropping rate: 2 mL/min, Volume of the reducing solution: 10 mL.
38. **Figure 3.2.2.B** EDAX spectrum of sample prepared when addition done at 60 °C. [$Fe(acac)_3$] = 30 mmol/L (V = 50 mL), Reducing acid solution containing [ascorbic acid] = 25 mmol/L, [water] = 12 mol/L, Dropping rate: 2 mL/min, Volume of the reducing solution: 10 mL.
39. **Figure 3.2.2.C** EDAX spectrum of sample prepared when addition done at 80°C. [$Fe(acac)_3$] = 30mmol/L (V = 50 mL), Reducing acid solution containing [ascorbic acid] = 25 mmol/L, [water] = 12 mol/L, Dropping rate: 2 mL/min, Volume of the reducing solution: 10 mL.
40. **Figure 3.2.2.D** HRTEM images and particle diameter distribution histogram of sample prepared when addition done at 60 °C (a), addition done at 80 °C (b). [$Fe(acac)_3$] = 30

mmol/L (V = 50 mL), Reducing acid solution containing [ascorbic acid] = 25 mmol/L, [water] = 12 mol/L, Dropping rate: 2 mL/min, Volume of the reducing solution: 10 mL.

41. **Figure 3.2.2.E** X-ray diffraction pattern of sample prepared with addition of ascorbic acid at 70 °C and reflux for 1 hour. [$Fe(acac)_3$] = 30mmol/L (V = 50 mL), Reducing acid solution containing [ascorbic acid] = 25 mmol/L, [water] = 12 mol/L, Dropping rate: 2 mL/min, Volume of the reducing solution: 10 mL.
42. **Figure 3.2.2.F** HRTEM images (a, b) and particle diameter distribution histogram of Fe_3O_4 nanoparticles at addition temperature of 70 °C. [$Fe(acac)_3$] = 30mmol/L (V = 50 mL), Reducing acid solution containing [ascorbic acid] = 25 mmol/L, [water] = 12 mol/L, Dropping rate: 2 mL/min, Volume of the reducing solution: 10 mL.
43. **Figure 3.2.2.G** EDAX analysis of Fe_3O_4 nanoparticles sample. [$Fe(acac)_3$] = 30mmol/L (V = 50 mL), Reducing acid solution containing [ascorbic acid] = 25 mmol/L, [water] = 12 mol/L, Dropping rate: 2 mL/min, Volume of the reducing solution: 10 mL.
44. **Figure 3.2.2.H** Survey XPS scan (a), C1s spectrum of C (b), [$Fe(acac)_3$] = 30 mmol/L (V = 50 mL), addition temperature of 70 °C, Reducing acid solution containing [ascorbic acid] = 25 mmol/L, [water] = 12 mol/L, Dropping rate: 2 mL/min, Volume of the reducing solution: 10 mL.
45. **Figure 3.2.2.I** XPS spectra of Fe_3O_4 nanoparticles Fe2p region. [$Fe(acac)_3$] = 30 mmol/L (V = 50 mL), Reducing acid solution containing [ascorbic acid] = 25 mmol/L, addition temperature of 70 °C, [water] = 12 mol/L, Dropping rate: 2 mL/min, Volume of the reducing solution: 10 m.
46. **Figure 3.2.2.J** XRD pattern of sample prepared without ultrapure water. [$Fe(acac)_3$] = 30mmol/L (V = 50 mL), at 70 °C, Reducing acid solution containing [ascorbic acid] = 25 mmol/L, [water] = 0 mol/L, Dropping rate: 2 mL/min, Volume of the reducing solution: 10 mL.
47. **Figure 3.2.2.K** EDAX spectrum of sample prepared without ultrapure water. [$Fe(acac)_3$] = 30mmol/L (V = 50 mL), at 70 °C, Reducing acid solution containing [ascorbic acid] = 25 mmol/L, [water] = 0 mol/L, Dropping rate: 2 mL/min, Volume of the reducing solution: 10 mL.
48. **Figure 3.2.2.M** HRTEM images of Fe_3O_4 nanoparticles prepared without using ultrapure water at 70 °C, Fe/iron oxide nanoparticles prepared without ultrapure water (a, b). [$Fe(acac)_3$] = 30 mmol/L (V = 50 mL), Reducing acid solution containing [ascorbic acid] = 25 mmol/L, [water] = 0 mol/L, Dropping rate: 2 mL/min, Volume of the reducing solution: 10 mL.
49. **Figure 3.2.2.N** Survey XPS scan (a), C1s spectrum of C (b), XPS Fe2p spectrum of sample prepared without using ultrapure water 0 mol/L (c) [$Fe(acac)_3$] = 30 mmol/L (V = 50 mL), reducing acid solution containing [ascorbic acid] = 25 mmol/L, Dropping rate: 2 mL/min, Volume of the reducing solution: 10 mL.

50. **Figure 3.2.2.O** O1s spectrum of O in sample prepared with water 12 mol/L (a), O1s spectrum of O in sample prepared without water i.e. 0 mol/L (b), [$Fe(acac)_3$] = 30 mmol/L (V = 50 mL), reducing acid solution containing [ascorbic acid] = 25 mmol/L, Dropping rate: 2 mL/min, Volume of the reducing solution: 10 mL.
51. **Figure 3.2.3.A** XRD pattern of sample prepared with addition of ascorbic acid at 70°C and at different precursor [$Fe(acac)_3$] (V= 50 mL) concentrations, (a) at 15mM $Fe(acac)_3$, (b) at 50mM $Fe(acac)_3$. Reducing acid solution containing [ascorbic acid] = 25 mmol/L, [water] = 12 mol/L, Dropping rate: 2 mL/min, Volume of the reducing solution: 10 mL..
52. **Figure 3.2.3.B** EDAX spectrum of sample prepared with addition of ascorbic acid at 70 °C and at 15 mM precursor [$Fe(acac)_3$] (V = 50 mL) concentration. Reducing acid solution containing [ascorbic acid] = 25 mmol/L, [water] = 12 mol/L, Dropping rate: 2 mL/min, Volume of the reducing solution: 10 mL.
53. **Figure 3.2.3.C** EDAX spectrum of sample prepared with addition of ascorbic acid at 70 °C and at 50 mM precursor [$Fe(acac)_3$] (V = 50 mL) concentration. Reducing acid solution containing [ascorbic acid] = 25 mmol/L, [water] = 12 mol/L, Dropping rate: 2 mL/min, Volume of the reducing solution: 10 mL.
54. **Figure 3.2.3.D** TEM and HRTEM images and particle diameter distribution histogram of nanoparticles prepared at addition temperature at 70 °C and at different precursor concentration, (a) TEM images of nanoparticles at 15 mM [$Fe(acac)_3$] (V = 50 mL) concentration, (b) HRTEM images of nanoparticles at 50 mM [$Fe(acac)_3$] (V = 50 mL) concentration. Reducing acid solution containing [ascorbic acid] = 25 mmol/L, [water] = 12 mol/L, Dropping rate: 2 mL/min, Volume of the reducing solution: 10 mL.
55. **Figure 3.2.4.A** X-ray diffraction pattern of sample prepared with addition temperature at 70 °C and reducing acid solution containing [ascorbic acid], (a) at 0.05 M, (b) at 0.005 M. [$Fe(acac)_3$] = 30 mmol/L (V = 50 mL), [water] = 12 mol/L, Dropping rate: 2 mL/min, Volume of the reducing solution: 10 mL.
56. **Figure 3.2.4.B** EDAX spectrum of sample prepared with addition temperature of 70 °C and reducing acid solution containing [ascorbic acid] 0.005 M. [$Fe(acac)_3$] = 30mmol/L (V = 50 mL), [water] = 12 mol/L, Dropping rate: 2 mL/min, Volume of the reducing solution: 10 mL.
57. **Figure 3.2.4.B** EDAX spectrum of sample prepared with addition temperature of 70 °C and reducing acid solution containing [ascorbic acid] 0.05 M. [$Fe(acac)_3$] = 30 mmol/L (V = 50 mL), [water] = 12 mol/L, Dropping rate: 2 mL/min, Volume of the reducing solution: 10 mL.
58. **Figure 3.2.4.D** HRTEM images and particle diameter distribution histogram of nanoparticles prepared at addition temperature of 70 °C and at different ascorbic acid concentrations, (a) HRTEM images of nanoparticles at 0.005 M ascorbic acid concentration, (b) HRTEM images of nanoparticles at 0.05M ascorbic acid concentration.

[$Fe(acac)_3$] = 30 mmol/L (V = 50 mL), [water] = 12 mol/L, Dropping rate: 2 mL/min, Volume of the reducing solution: 10 mL.

59. **Figure 3.2.5.A** X-ray diffraction pattern of sample prepared with addition temperature at 70 °C and at 1 mL/min dropping rate. [$Fe(acac)_3$] = 30 mmol/L (V = 50 mL), Reducing acid solution containing [ascorbic acid] = 25 mmol/L, [water] = 12 mol/L, Volume of the reducing solution: 10 mL.
60. **Figure 3.2.5.B** EDAX spectrum of sample prepared with addition temperature of 70 °C and at dropping rate of 1 mL/min. [$Fe(acac)_3$] = 30 mmol/L (V = 50 mL), Reducing acid solution containing [ascorbic acid] = 25 mmol/L, [water] = 12 mol/L, Volume of the reducing solution: 10 mL.
61. **Figure 3.2.5.C** HRTEM images and particle diameter distribution histogram of nanoparticles prepared at addition temperature of 70 °C and at 1 mL/min dropping rate. [$Fe(acac)_3$] = 30 mmol/L (V = 50 mL), Reducing acid solution containing [ascorbic acid] = 25 mmol/L, [water] = 12 mol/L, Volume of the reducing solution: 10 mL.
62. **Figure 4.1.1.A** Chemical structure of graphene (a) [4], TEM image of graphene (b).
63. **Figure 4.3.1** FTIR spectrum of carboxylated graphene. [$Fe(acac)_3$] = 30mmol/L (V = 50 mL), Reducing acid solution containing [ascorbic acid] = 25 mmol/L, [water] = 12 mol/L, Dropping rate: 2 mL/min, Volume of the reducing solution: 10 mL.
64. **Figure 4.3.2** XPS survey or full scan spectrum of carboxylated graphene. [$Fe(acac)_3$] = 30mmol/L (V = 50 mL), Reducing acid solution containing [ascorbic acid] = 25 mmol/L, [water] = 12 mol/L, Dropping rate: 2 mL/min, Volume of the reducing solution: 10 mL.
65. **Figure 4.3.3** (a) XPS - C1s spectra of carboxylated graphene, (b) XPS-O1s spetra of carboxylated graphene. [$Fe(acac)_3$] = 30mmol/L (V = 50 mL), Reducing acid solution containing [ascorbic acid] = 25 mmol/L, [water] = 12 mol/L, Dropping rate: 2 mL/min, Volume of the reducing solution: 10 mL.
66. **Figure 4.3.4.A** EDAX spectum of carboxylated graphene. [$Fe(acac)_3$] = 30mmol/L (V = 50 mL), Reducing acid solution containing [ascorbic acid] = 25 mmol/L, [water] = 12 mol/L, Dropping rate: 2 mL/min, Volume of the reducing solution: 10 mL.
67. **Figure 4.3.5** (a) SEM image of carboxylated graphene, (b) TEM image of carboxylated graphene and (c) HRTEM image of carboxylated graphene. [$Fe(acac)_3$] = 30mmol/L (V = 50 mL), Reducing acid solution containing [ascorbic acid] = 25 mmol/L, [water] = 12 mol/L, Dropping rate: 2 mL/min, Volume of the reducing solution: 10 mL.
68. **Figure 4.3.6** XPS survey or full scan spectrum of graphene-Fe_3O_4 nanocomposite. [$Fe(acac)_3$] = 30mmol/L (V = 50 mL), Reducing acid solution containing [ascorbic acid] = 25 mmol/L, [water] = 12 mol/L, Dropping rate: 2 mL/min, Volume of the reducing solution: 10 mL.
69. **Figure 4.3.7** XPS of Fe2p region for Fe_3O_4 nanoparticles in graphene-Fe_3O_4 nanocomposite. [$Fe(acac)_3$] = 30mmol/L (V = 50 mL), Reducing acid solution containing

[ascorbic acid] = 25 mmol/L, [water] = 12 mol/L, Dropping rate: 2 mL/min, Volume of the reducing solution: 10 mL.

70. **Figure 4.3.8** XPS spectrum of Graphene-Fe_3O_4 nanocomposite.
C 1s spectrum and (b) O 1s spectrum. [$Fe(acac)_3$] = 30mmol/L (V = 50 mL), Reducing acid solution containing [ascorbic acid] = 25 mmol/L, [water] = 12 mol/L, Dropping rate: 2 mL/min, Volume of the reducing solution: 10 mL.
71. **Figure 4.3.9** (a, b) TEM images of graphene-Fe_3O_4 nanocomposite, (c, d) SEM images of graphene-Fe_3O_4 nanocomposite, (e and f) SEM and TEM image of bare Fe_3O_4 nanoparticles. [$Fe(acac)_3$] = 30mmol/L (V = 50 mL), Reducing acid solution containing [ascorbic acid] = 25 mmol/L, [water] = 12 mol/L, Dropping rate: 2 mL/min, Volume of the reducing solution: 10 mL.
72. **Figure 4.3.10.A** EDAX spectrum of graphene-Fe_3O_4 nanocomposite. [$Fe(acac)_3$] = 30mmol/L (V = 50 mL), Reducing acid solution containing [ascorbic acid] = 25 mmol/L, [water] = 12 mol/L, Dropping rate: 2 mL/min, Volume of the reducing solution: 10 mL.
73. **Figure 4.3.11** Raman spectra (a) graphene and (b) graphene-Fe_3O_4 nanocomposite. [$Fe(acac)_3$] = 30mmol/L (V = 50 mL), Reducing acid solution containing [ascorbic acid] = 25 mmol/L, [water] = 12 mol/L, Dropping rate: 2 mL/min, Volume of the reducing solution: 10 mL.

LIST OF RESEARCH ACHIEVEMENTS

I. PUBLICATIONS

1. Size controlled synthesis of Fe_3O_4 nanoparticles by ascorbic acid mediated reduction of $Fe(acac)_3$ without using capping agent.

Ajinkya Nene, M. Takahashi, K. Wakita, M. Umeno, Journal of Nano Research. 40(2016) 8-19.

2. Synthesis and characterization of graphene-Fe_3O_4 nanocomposite.
   Ajinkya G. Nene, M. Takahashi, P. R. Somani, H. Aryal, K. Wakita, M. Umeno, Carbon - Science and Technology. 8 (2016) 13 - 24.

3. Fe_3O_4 and Fe nanoparticles by chemical reduction of $Fe(acac)_3$ by ascorbic acid: Role of Water.
   Ajinkya G. Nene, M. Takahashi, P. R. Somani, World Journal of Nano Science and Engineering. 6(2016) 20 - 28.

II. PUBLICATIONS IN PROCEEDINGS

1. "Synthesis and size control of Fe_3O_4 nanoparticles by reduction of $Fe(acac)_3$ using ascorbic acid", **Ajinkya G. Nene**, M. Takahashi, K. Wakita, P. Somani, M. Umeno, Global Conference in Engineering and Applied Science, Hokkaido, Japan (2016), 806-808, ISBN 978-986-5654-24-5.

III. INTERNATIONAL CONFERENCE PRESENTATIONS

1. "Synthesis and size control of Fe_3O_4 nanoparticles by reduction of $Fe(acac)_3$ using ascorbic acid", Ajinkya G. Nene, M. Takahashi, K. Wakita, P. Somani, M. Umeno, Global Conference in Engineering and Applied Science, Hokkaido, Japan (19 – 21 July, 2016).

Acknowledgement

I wish to express my sincere gratitude to my Ph. D. supervisor and Sensei Prof. Makoto Takahashi, Department of Applied Chemistry, Chubu University for giving me an opportunity to do this work under his supervision with a constant, guidance, valuable suggestions, and keeping me motivated.

I am really grateful to Prof. Ishikawa, Prof. Sakurai and Prof. Goto from Chubu University for their valuable comments and suggestions to improve the content of this thesis.

My sincere gratitude to Prof. Masayoshi Umeno, Institute of General Research of Science, Chubu University, Japan for constant support and encouragements. I am very grateful to Prof. Koichi Wakita, Department of Electronic and Information Engineering, Chubu University for his constant support and valuable comments and suggestions for this work.

My sincere gratitude to Dr. Prakash Somani for valuable suggestions, comments and scientific discussions throughout the progress of this work. I am greatful to Mr. Kawamura, Analysis Center (common facility lab.), Chubu University for his help, scientific discussions during the progress of this work.

I am really thankful to Dr. Hare Ram Aryal and Dr. Sudip Adhikary for their help, cooperation, while conducting some experiments and scientific discussions. I would like to thank all Master and Bachlor level students from Prof. Takahashi laboratory for their co-operative help during this work.

My sincere gratitude to Ministry of Education, Culture, Sports, Science and Technology (MEXT) (MONBUKAGAKUSHO) of Japan government for providing me fellowship during my Ph. D. research.

I would like to dedicate this work to my parents. I am really thankful to my friends and family for their motivation and support.